

ISBN 978-82-326-1532-2 (printed ver.)
ISBN 978-82-326-1533-9 (electronic ver.)
ISSN 1503-8181



Doctoral theses at NTNU, 2016:97

Federico Mazzola

Photoemission spectroscopies
and their application in solid
state and material physics

 **NTNU**
Norwegian University of
Science and Technology

Doctoral theses at NTNU, 2016:97

 NTNU

NTNU
Norwegian University of
Science and Technology
Thesis for the degree of
Philosophiae Doctor
Faculty of Natural Science and Technology
Department of Physics

 **NTNU**
Norwegian University of
Science and Technology

Federico Mazzola

Photoemission spectroscopies and their application in solid state and material physics

Thesis for the degree of Philosophiae Doctor

Trondheim, April 2016

Norwegian University of Science and Technology
Faculty of Natural Science and Technology
Department of Physics



Norwegian University of
Science and Technology

NTNU

Norwegian University of Science and Technology

Thesis for the degree of Philosophiae Doctor

Faculty of Natural Science and Technology
Department of Physics

© Federico Mazzola

ISBN 978-82-326-1532-2 (printed ver.)
ISBN 978-82-326-1533-9 (electronic ver.)
ISSN 1503-8181

Doctoral theses at NTNU, 2016:97

Printed by NTNU Grafisk senter

“When asked what he meant by a miracle:
Oh, anything with a probability of less than 20 %”

Enrico Fermi

Acknowledgments

In my life, the interaction and exchange of ideas with many different people has been an important ingredient which allowed me to develop myself as the person I am now. In science, it happens the same. The interaction with several scientists has been a fruitful possibility to develop my skills and to learn new ones. This is why I am first of all extremely grateful to all my collaborators and people I have met during this scientific path.

In particular, I would like to thank my Supervisor Justin Wells for his encouragement, help, guidance and friendship during my PhD. Without his support my thesis and my PhD itself would have not been possible. I thank him for the helpful suggestions and freedom he gave me to fulfill my thesis.

I thank Dr. Simon Cooil, Postdoc in our group for the help received, guidance and fun experimental time. Thanks to all the students we had in our lab, from which I learn many things and hopefully I have been a good mentor too, in particular Elise R., Cecilie G., Marit K. and Helene K. I am grateful to my collaborators who contributed to make all this possible. First of all Dr. Phil King for his encouragement, fruitful discussions and extremely useful advice and his students Lewis B. and Jon R.; I am grateful to the help received by Prof. Philip Hofmann, Prof. Jill Miwa and Dr. Marco Bianchi who had an important role for my personal and scientific development. I acknowledge Matteo M., Macjek D., Antonija C., Fabian A., Alex P. T. and all the people I collaborated with. I thank the beamline scientists who made our experiments possible and who contributed to the understanding of our scientific results, in particular ‘Balu’, Mats L., Alexei P., Johan A. Thanks to my girlfriend Gaia for the support and my friends Eva, Louise, Luca, Sylwie, Jesper, Eirik for the nice time spent together and great suggestions.

Abstract

Understanding the electronic properties of materials is of fundamental importance to all matter. Investigating the role of spin and charges in solid state systems has been conjectured to play a key role to broaden our fundamental knowledge in diverse areas, whilst establishing new approaches to design materials with tailored properties.

Photoemission spectroscopy is a powerful and versatile tool, able to elucidate the electronic properties of solid state systems, giving fundamental insight into the microscopic origin of several physics and chemistry phenomena ranging from spin-orbit coupling, electric- and size-driven quantum-confinement, crystal field splitting, many-body interactions, charge and spin ordering to surface-catalysis and surface-reactions.

Photoemission spectroscopy is here used to investigate the electronic properties of carbon-based materials such as graphene and diamond, layered materials such as WSe_2 and NbSe_2 , hybrid systems such as phosphorus δ -layers in silicon and boron δ -layers in diamond, intermediate band materials such as Cr-doped ZnS and the catalytic activity of metal surfaces in contact with organic molecules.

Specifically, this thesis is aimed to expand the photoemission toolbox for studying how the interplay of physical dimensionality, many-body effects and spin-orbit coupling influences the quantum many-body ground states of a system and how relevant the choice of a certain material can be for manipulating and re-ordering the hierarchy of the energy scales by which such effects manifest.

By using photoemission-based techniques combined with computational

approaches I aim to understand such effects for a wide range of systems, providing a platform to move beyond the existing state-of-the-art in conventional materials to open new potential for ultimate exploitation in multifunctional devices.

Short Overview

In this thesis I show how by using photoemission spectroscopies it is possible to understand the electronic properties of 2D electron gases (2DEGs) buried into the bulk of semiconductors. The particular systems studied are δ -layers. Such systems have been demonstrated to offer great potential as components of quantum computers, but the understanding of their electronic properties remains often elusive and, crucially, even controversial. Furthermore, even though atomically precise patterning of δ -layers has been achieved, there is real dearth of methodologies able to control and tune the electronic properties of these materials. Here, I show how by controlling the shape of the doping potential which gives rise to such 2DEGs, it is possible to change the nature of the quantum dynamics of these systems, directly affecting carrier mobilities, the lifetime of carriers and, more generically, transport properties. Moreover, I show how many-body effects contribute to affect such properties, which are of fundamental interest for the exploitation of δ -layers in electronic devices. I show this for two systems: P δ -layers in Si and B δ -layers at the surface of diamond (001).

I show how quantum-confined structures for quantum computer architectures can be realized by using self-assembly molecules: certain organic compounds have the intriguing property of self organizing in a periodic fashion onto the top of metallic surfaces, creating an ordered array of quantum dots which is also suitable for further manipulation. We realized this by using porphyrin derivatives onto the top of Ag(111) and we show how spectroscopic feedback can be achieved by using ARPES: insight into carriers' velocities and effective masses can be achieved shedding light on properties of fundamental interest for a quantum device.

I investigate the unusual electronic structure of 2H-phase centrosymmetric transition metal dichalcogenides (TMDCs). TMDCs are a class of lay-

ered materials with inversion symmetric unit cell. The high atomic number of the elemental constituents of TMDCs is responsible for a big spin-orbit coupling which lifts the energy degeneracy of the electronic bands of these systems which, nonetheless, remain spin-degenerate because of the powerful combination of time-reversal and inversion symmetries. However, by using spin-ARPES, we demonstrate that the electronic bands, at certain positions of the Brillouin zone, exhibit 100% spin-polarized character. In agreement with recent theoretical studies, we demonstrate how this can be possible in TMDCs: in these systems the electron wavefunctions are extremely localized within each layer and in each layer inversion symmetry is broken. Such a punctual absence of inversion symmetry has been conjectured as a powerful way to create spin-polarized electronic states even in centrosymmetric materials.

In this thesis, I also give attention to C-based materials of low dimensionality. In particular, a systematic study of the many-body effects in graphene is presented. However, whilst the attention on graphene has been always restricted to its π -band (which is responsible for the transport properties of graphene), here I shed light on new fundamental physics happening at the top of the σ -band of graphene (≈ 3.5 eV from the Fermi level): in this band, electron-phonon coupling is exceptionally strong and the bands are renormalized by such an effect. Whilst this is unusual because collective excitations have never been thought to be possible away from the Fermi level, it also paves important conceptual pathways suggesting methodologies for turning graphene into a superconductor. To this end, I here show both experimental and theoretical aspects of this unusual phenomenon and I present, by using first principle calculations, the reasons by which electron-phonon coupling can manifest also at energies away from the Fermi level.

Photoemission spectroscopies are here used also to investigate the electronic properties of 3D materials. In particular, I show the use of resonant photoemission spectroscopy to characterize the intermediate band system Cr-doped ZnS. This system consists of a ZnS bulk where Cr impurities have been added during the growth process. Cr creates electronic states within the bandgap and such states allow for additional absorption/emission processes to take place. For example, without intermediate states, an electron in the valence band can be photo-excited into the conduction band only for one particular wavelength of the excitation source. If an intermediate state

is present, not only the same mechanism takes place, but even bigger wavelengths can excite an electron: such an electron can be first promoted into the intermediate state and from such a state it can be promoted into the conduction band. This means that the presence of intermediate bands in this system allows for multiple transitions to take place. This is of big interest for photovoltaics and solar cells, whose efficiency would result greatly enhanced by the realization of the processes described.

Low dimensional materials such as graphene attracted attention also for their low reactivity. These systems are therefore suitable for coating purposes. I present a recent work about the use of photoemission for characterizing chemotherapy drugs and their reaction with materials which are generally used for delivering such drugs during the treatment of cancer. In particular I show that the reaction between 5-Fu (which is one of the most used drugs in chemotherapy) and silver (which is one of the most common materials used for coating the catheters by which the chemotherapy drugs are delivered) creates HF as a reaction product, probably complicating even more the quality of the treatment and suggesting that alternative coating materials are strongly desired. To this end we suggest graphene as a coating material and we show, by using photoemission, that 5-Fu does not react with it at all. This suggests graphene as an interesting alternative material for coating purposes in medical applications.

Preface

This thesis is submitted to the Norwegian University of Science and Technology (NTNU, Trondheim) for partial fulfillments of the requirements for the degree Philosophiae Doctor (Ph.D). It is based on 7 published and 10 works in-progress papers about the importance of photoemission-based techniques for the study of spin and electronic properties of solid state systems.

This work has been carried out at NTNU and at several synchrotron facilities such as Max-II and Max-III (Lund, Sweden), ASTRID-2 (Århus, Denmark), BESSY (Berlin, Germany), PSI (Zürich, Switzerland) and at The Australian Synchrotron (Melbourne, Australia) under supervision of Prof. Justin W. Wells and co-supervision of Prof. John Walmsley.

Papers included in the Thesis

1.

“Disentangling phonon and impurity interactions in δ -doped Si(001)”

F. Mazzola, C. M. Polley, J. A. Miwa, M. Y. Simmons and J. W. Wells.
Appl. Phys. Lett. 104, 173108 (2014)

Contribution: Measurements – Data analysis – Paper drafting

2.

“Determining the Electronic Confinement of a Subsurface Metallic State”

F. Mazzola, M. T. Edmonds, K. Høydalsvik, D. J. Carter, N. A. Marks,
B. C. C. Cowie, L. Thomsen, J. Miwa, M. Y. Simmons and J. W. Wells.
ACS Nano 8, 10 pp 10223-10228 (2014)

Contribution: Measurements – Data analysis – Paper drafting

3.

“Controlling and tuning simultaneous conduction and valence band quantization in artificial, nearly atomic-scale doping profiles in semiconductors”

F. Mazzola, J. W. Wells, A. P. Tabrizi, R. Jackman, B. Thiagarajan,
M. Y. Simmons, P. Hofmann and J. A. Miwa. *In progress*

Contribution: Measurements – Analysis – Numerical model – Paper drafting

4.

“Sub-band structure in asymmetric doping-profiles”

F. Mazzola, Jill A. Miwa, Rajib Rahman, Xie-Gang Zhu, Michelle Y. Simmons, Philip Hofmann and Justin W. Wells. *In progress*

Contribution: Measurements – Analysis – Paper drafting

5.

“Adsorbate induced modification of the confining barriers in a quantum box array”

S. Nowakowska, F. Mazzola, M. Wiss, C. Polley, M. Leandersson, S. Fattayer, T. Ivas, S. F. Mousavi, A. Ahsan, T. Nijs, O. Popova, J. Zhang, M. Muntwiler, C. Thilgen, M. Sthör, F. Diederich, J. Wells, T. Jung. *In progress*

Contribution: ARPES Measurements – ARPES analysis – Helping paper drafting

6.

“Boron-doped diamond preserving bulk-like properties at the near atomic scale”

F. Mazzola, A. Pakpour Tabrizi, J. A. Miwa, F. Arnold, M. Bianchi, P. Hofmann, R. Jackman, J. W. Wells. *In progress*

Contribution: Measurements – Analysis – Paper drafting

7.

“Direct observation of spin-polarized bulk bands in an inversion-symmetric semiconductor”

J. M. Riley, F. Mazzola, M. Dendzik, M. Michiardi, T. Takayama, L. Bawden, C. Granerød, M. Leandersson, T. Balasubramanian, M. Hoesch, T. K. Kim, H. Takagi, W. Meevasana, Ph. Hofmann, M. S. Bahramy, J. W. Wells and P. D. C. King. *Nature Physics* 10, 835–839 (2014)

Contribution: Participated in the spin-ARPES measurements and data analysis.

8.

“Kinks in the σ Band of Graphene Induced by Electron-Phonon Coupling”

F. Mazzola, J. W. Wells, R. Yakimova, S. Ulstrup, J. A. Miwa, R. Balog, M. Bianchi, M. Leandersson, J. Adell, P. Hofmann and T. Balasubramanian. *Phys. Rev. Lett.* 111, 216806 (2013)

Contribution: Data analysis – Paper drafting – Developing the 2D fit procedure

9.

“Strong electron-phonon coupling in the σ -band of graphene”

T. Frederiksen, F. Mazzola, J.W. Wells, T. Balasubramanian and B. Hellsing. *In progress*

Contribution: Measurements – Analysis of the data acquisitions

10.

“Evidence of inter-band scattering between π and σ - band of graphene”

F. Mazzola, T. Frederiksen, A. Sohanfo Ngankeu, J. A. Miwa, A. Grubisic Cabo, M. Michiardi, M. Bianchi, C. M. Polley, P. Hofmann, B. Hellsing, B. Thiagarajan and J. W. Wells. *In progress*

Contribution: Measurements – Data analysis – Paper drafting

11.

“Resonant photoemission spectroscopy for intermediate band materials”

F. Mazzola, M. Nematollahi, Z. S. Li, S. Cooil, X. Yang, T. W. Reenaas and J. W. Wells. *Appl. Phys. Lett.* 107, 192104 (2015)

Contribution: Measurements – Data analysis – Paper drafting

12.

“Graphene coatings for chemotherapy: avoiding silver-mediated degradation”

F. Mazzola, T. Trinh, S. Cooil, E. R. østli, K. Høydalsvik, E. T. Bakken Skjønsgjell, S. Kjelstrup, A. Preobrajenski, A. A. Cafolla, D. A. Evans, D. W. Breiby and J. W. Wells. *2D Mater.* 2, 025004 (2015)

Contribution: Measurements – Data analysis – Paper drafting

Additional papers

This category includes papers where I had a less significant role. For these papers, I contributed with acquiring the measurements at synchrotron facilities or helped with the data analysis or contributed to preparing the manuscript.

13.

“Valley Splitting in a Silicon Quantum Device Platform”

J. A. Miwa, O. Warschkow, D. J. Carter, N. A. Marks, F. Mazzola, M. Y. Simmons and Justin W. Wells. *Nano Lett.*, 14 (3), pp 1515–1519, (2014)

14.

“Spin-valley locking in the normal state of a transition-metal dichalcogenide superconductor”

L. Bawden, S. P. Cooil, F. Mazzola, J. M. Riley, L. J. Collins-McIntyre, V. Sunko, K. Hunvik, M. Leandersson, C. M. Polley, T. Balasubramanian, T. K. Kim, M. Hoesch, J. W. Wells, G. Balakrishnan, M. S. Bahramy, and P. D. C. King. *Submitted*, <http://arxiv.org/pdf/1603.05207.pdf>

15.

“Surface Dimensionality Transition on a Curved Bi(111) Sample: Surface States Evolution from Topologically Trivial to Topologically protected”

J. Lobo-Checa, F. Mazzola, L. Barreto, F. M. Schiller, J. W. Wells, M. Corso, L. A. Miccio, I. Piquero-Zulaica, N. C. Plumb, P. Hofmann, and

J. E. Ortega. *In progress*

16.

“In-situ growth and characterization of patterned δ -layer structures in Silicon”

S. P. Cooil, F. Mazzola, H. W. Klemm, G. Peschel, Y. R. Niu, A.x Zhakarov, A. Evans, M. Y. Simmons, J. A. Miwa and J. W. Wells *In progress*

17.

“Degradation of the chemotherapy drug 5-Fluorouracil on medical silver surfaces”

H. Kjær, S. Cooil, F. Mazzola, T. Trinh, E. Torbjørn Bakken Skjønshjell, D.Hu, E. Ramleth Østli, N. Patil, A. Preobrajenski, A. Evans, D.g W. Breiby and J. W. Wells *In progress*

Contents

1	Introduction	1
1.1	The importance of bound electrons	1
1.2	Main scientific questions	3
1.2.1	2DEGs in semiconductors and quantum materials . . .	3
1.2.2	Graphene	4
1.2.3	3D materials with unconventional properties and/or for unconventional applications	5
2	Methods and experimental requirements	7
2.1	Ultrahigh Vacuum, UHV	7
2.2	Pumping system	8
2.3	Sample Cleaning	11
2.3.1	Annealing	11
2.3.2	Ion Sputtering Cleaning	12
2.3.3	Cleaving	14
2.4	Sample Growth	15
2.4.1	Thermal evaporation	15
2.4.2	Gas dosing	16
3	Photoemission	18
3.1	The basic theory	18
3.1.1	Electronic states	19
3.1.2	From bulk to surface states	21
3.1.3	Quantum well states	23
3.2	Introduction to photoemission	25
3.3	Many-Body interactions	27
3.4	Photoemission experiments	28
3.5	Mapping the electronic structure of solids	29

3.6	2D and 3D mapping	32
4	Main photoemission techniques used in this work	35
4.1	Angle-resolved photoemission spectroscopy, ARPES	35
4.2	Spin-ARPES	40
4.3	X-ray photoemission spectroscopy	43
4.4	Resonant Photoemission Spectroscopy	45
5	Main Materials	48
5.1	2D-systems	48
5.1.1	Graphene	48
5.1.2	δ -layers	49
5.2	Layered compounds: transition metal dichalcogenides (TMDs)	52
5.3	Cr-doped ZnS	53
5.4	5-Fluorouracil, 5-Fu	54
5.5	A self-assembled organic monolayer, porphyrin	54
5.6	Curved samples, the Bi case	55
6	Analysis and Modeling	57
6.1	Data Fitting	57
6.1.1	2D-fit and many body interactions	59
6.2	Tight-binding	61
6.2.1	π -band of graphene, a simple tight-binding approach .	62
7	Papers included in the Thesis	66
8	Conclusions	67
8.1	Summary of the main results	74
8.2	Final considerations	76

Chapter 1

Introduction

Einstein's formulation of the photoelectric effect [1] is certainly one of the major discoveries of the last century and gave Einstein the Nobel prize for physics in 1921. The photoelectric effect describes the mechanism by which a metal emits electrons (thus called photoelectrons) when light shines upon it. Following its formulation, this effect found widespread use in technological applications giving birth to the arsenal of techniques and devices which contributed to advance familiar technologies such as mobile telephones, solar cells, image sensors, night vision devices and computers.

These devices are testament to the rich and broad impact of this effect but there is more than this: whilst contributing to the establishment of technology as we know it today, the photoelectric effect has been a milestone for developing techniques such as photoemission spectroscopies, making possible the understanding of the fundamental physics laws which dominate the behavior of bound electrons in solid state systems and the chemistry of various materials.

1.1 The importance of bound electrons

In any material, bound electrons are an indispensable building block which ensures the existence of the material itself providing the explanation to the origin of local bondings between atoms and molecules. For this reason, they are an essential ingredient for explaining chemical, physical, thermal, mag-

netic and vibrational properties of materials. Measuring, understanding and tailoring the properties of bound electrons is an important goal with interest to all matter.

For example, if we could hypothetically get full control over the charges and electrons' spins in a certain system, we might be able to produce currents without significant energy losses. The heat loads generated by a device could be dramatically reduced and an even more intelligent use of the energetic resources could be realized.

Photoemission spectroscopy is probably one of the most powerful techniques for probing the collective behavior of electrons in a solid. The importance of this method in diverse scientific areas represents a perfect opportunity in the context of a PhD itinerary, especially when combined to materials which host unconventional electronic properties not easily reconcilable with the current textbook explanations.

Hybrid quantum-materials such as P δ -layers in silicon are an example of this: their properties rely on an unusually narrow artificial quantum confinement and only by modifying such a confinement, it would be possible to use this material for real applications. Specifically, the lifetimes of carriers in this system depend on the quantum confinement, whose nature has been demonstrated to be often elusive and controversial. Photoemission can be an incredibly powerful tool for studying, understanding and ultimately tailoring the properties of these systems, shedding light on new aspects never investigated before with other techniques.

In the course of my PhD, non-standard photoemission spectroscopies, such as resonant and spin- and angle-resolved photoemission spectroscopy have been used, as well as we made use of photoemission to study non-surface localized two-dimensional electronic states and organic molecules. This all constitutes a non-standard use of photoemission with the aim of going beyond conventional approaches whilst expanding the fundamental knowledge about the physics and chemistry of materials.

For example, spin- and angle-resolved photoemission spectroscopy has been demonstrated to be essential for describing the spin texture of spin-orbit coupled solid state systems. As I will describe later in this thesis, this

technique can be the turning point for describing the unusual existence of fully spin-polarized electronic bands in materials which preserve their inversion symmetry within the unit cell. This demonstrates an important breakthrough in solid state physics and constitutes a big departure from a generally accepted concept.

For these reasons, my Thesis is developed around the context of a vast array of photoemission-based techniques for studying materials with unconventional electronic properties. Because of such a wide variety of techniques based on photoemission and such a broad spectrum of unusual solid state materials I see this PhD study as a unique opportunity for a multifaceted, powerful and versatile approach for studying materials targeted for various applications.

1.2 Main scientific questions

In this Thesis several systems are introduced, each one hosting unique properties whose understanding will contribute to expand the fundamental knowledge in solid state physics, whilst contributing to open potential routes for developing novel concepts and technologies. Here, I briefly introduce the main systems investigated in this Thesis, as well as the main scientific questions I would like to answer. A full description of the materials, techniques and physics will be presented later in the following chapters; thus, this is only an introduction to the scientific problems which will be discussed.

1.2.1 2DEGs in semiconductors and quantum materials

I examine a class of quantum materials, such as P δ -layers in Si and B δ -layers in diamond, to understand the role of many-body effects and how such effects might be potentially modified to tune material properties. Thus, I would like to answer the questions: *(i) which are the most important contributions coming from many-body interactions for these systems and which is their involvement in superconductivity? (ii) Is there any way to modify the shape of the doping potential in order to control the lifetime of carriers? (iii)*

How can we shape, pattern and build architectures out of these systems for technology and how do these new systems behave compared to their mother compounds?

Even though understanding these questions would offer real potential for quantum technology, another parallel and interesting way would be to investigate a class of self-organizing quantum materials: for example, certain molecules arrange to form a periodic net of quantum dots onto the top of metallic substrates. The advantage offered by these molecules is that there would not be any need of patterning them, since they would naturally form a desired pattern on a chosen substrate. Thus, we want to answer the question: *(iv) can we use photoemission to probe the electronic properties of self-assembly molecules and can we get information regarding their effective masses and transport?*

In the framework of quantum systems, in the framework of quantum systems, we also choose to study strongly spin-orbit coupled, such as WSe₂ and NbSe₂. These systems have been conjectured as important materials for spintronics and spin-based electronics. Due to their intrinsic spin-orbit coupling, WSe₂ and NbSe₂ can exhibit spin-polarized bands, i.e. the electronic bands of these systems can carry electrons with the same spin. Whilst this is generally true for single layer materials, the bulk phase of these systems should exhibit spin-degenerate bands because of the combination of time reversal and inversion symmetries. However, according to recent theories, centrosymmetric materials can also host fully spin-polarized bands in the case that inversion symmetry is locally broken. We therefore want to answer the question: *(v) Is it possible to experimentally prove this expectation? (vi) How does the spin-texture in these systems look like and how does it affect their electronic properties in perspective of real applications?*

1.2.2 Graphene

Graphene is another material studied in this Thesis. Importantly, we observe that at the top of the σ -band, which is at 3.5 eV below the Fermi level, strong ‘kinks’ appear. This is reminiscent of electron-phonon coupling which is seen close to the Fermi level. However, collective excitations such as electron-phonon coupling have never been observed away from the Fermi

level and thought to be even impossible to manifest at different energies. Therefore, we want to answer the questions: *(vii)* Are the observed ‘kinks’ a manifestation of electron-phonon coupling? *(viii)* How can such an effect manifest away from the Fermi level and which are the implications for novel technologies?

1.2.3 3D materials with unconventional properties and/or for unconventional applications

Another class of materials examined in this Thesis includes 3D systems with unusual properties. In particular, two systems are studied: intermediate-band semiconductors and organic compounds used in medical applications, specifically in the treatment of cancer.

Intermediate-band semiconductors are important systems for photovoltaics, as they would give higher efficiency than that one offered by the existing photovoltaics technology. They are comprised of a semiconducting bulk where impurities are added in order to create additional electronic states within the band gap of the host material. However, the orbital and elemental nature of these states have remained elusive. We want to answer the question: *(ix)* Is it possible to use photoemission spectroscopy to get information about the orbitals, electrons filling and spin character of such states? Answering this question is of fundamental importance for understanding how solar-cells materials can be improved in order to maximize their efficiency.

An interest aspect of graphene is associated to its low reactivity: the in plane bonding of this material are very strong, whilst the out of plane bondings are generally weak. This confers graphene the property of being inert, thus it could be used for coating materials which are generally prone to degradation when in contact with different agents. For example, we can use graphene for coating catheters which are used for delivering the drugs used in the treatment of cancer. One of the most accepted treatments against it is chemotherapy: chemotherapy drugs are injected into the body of a patient. Such drugs will inhibit the DNA to reproduce and the cancer cells will die. The drugs are injected through catheters made of materials such as silicone, but in order to avoid injuries and complications due to broken catheters, they

are often coated by silver alloys which are supposed to prevent the reactions between catheters and drugs. To the best of our knowledge no study has been carried out about the reaction occurring between the drugs which are delivered and the coating materials. Thus, a question we want to answer is: *(x) Is there any reaction happening when chemotherapy drugs get in contact with materials used for coating medical catheters? If so, can unreactive 2D materials, such as graphene, offer a superior coating?*

In the following chapters, I aim to answer these questions, giving important details about materials, techniques and the physics involved for each system.

Chapter 2

Methods and experimental requirements

2.1 Ultrahigh Vacuum, UHV

In surface science and photoemission experiments, an important goal is to perform the measurements in a clean environment. If we want a surface to stay clean as long as possible, at least as long as a measurement can be completed, no impurities and particles are allowed to stick onto such a surface. To ensure this cleanness requirement, the sample must be kept at pressures lower than 10^{-9} mbar. This condition is called ultrahigh vacuum (UHV).

In order to understand which is the vacuum requirement for a photoemission experiment, we can estimate the number of gas molecules which hit a surface per unit time. From the kinetic theory of gases:

$$R = \frac{dN}{dt} = \frac{P}{\sqrt{2\pi M k_B T}} \quad (2.1)$$

where P is the pressure, M is the molecular mass, T is the temperature and k_B is the Boltzmann constant. For water molecules at $P = 10^{-6}$ mbar and at room temperature (≈ 300 K) we obtain $R \approx 10^{14}$, a number comparable to the average number of atoms in a surface of area 1 cm^2 (10^{15}). At this condition, it only takes 1 s to contaminate the whole surface of a sample. This justifies the need of much lower pressure values, i.e. $\approx 10^{-9}$ mbar.

2.2 Pumping system

An intuitive requirement to create UHV in a vessel is a system of pumps aimed to remove most of the gas molecules from such a vessel. In typical vacuum systems, UHV is created by operating in series different types of pumps: *roughing pump*, *turbo pump*, *ion pump* and *getter pumps* (commonly, titanium sublimation pumps, TPS, are used). A simple and schematic pump diagram is illustrated in Fig. 2.1.

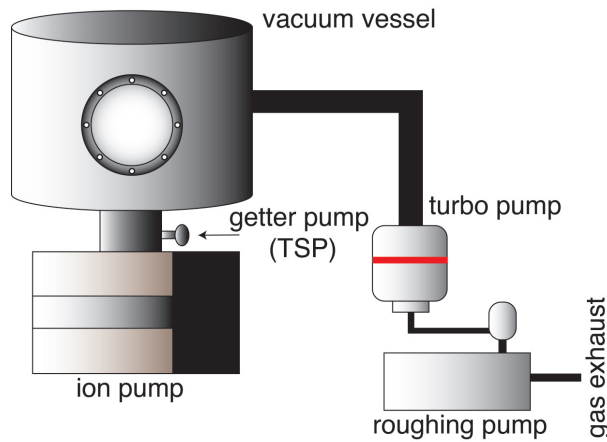


Figure 2.1: **Pump diagram.** A schematic of a simple pumps system used in a UHV experiment. Generally the vacuum vessel is connected directly to the ion pump, which is in series with a TSP. Roughing pump and turbo pump are in series.

Roughing pumps are used to put the system down to $\approx 10^{-3}$ mbar. The most common type of roughing pump is a rotary oil-sealed vane pump [9]. This pump consists of a rotor attached to two vanes at the center of a cavity. When the rotor is activated, the vanes rotate and they glide keeping touch to the inner surface of the cavity. This causes a compression of the gases inside the cavity which are delivered and then expelled through an exhaust gas-line.

Once the system reaches the minimum pressure permitted by the roughing pump, which as said is $\approx 10^{-3}$ mbar in an ideal situation, turbo pumps can be activated. A turbo pump consists of blades connected in series which rotate more than 80000 times per minute thanks to a rotor (see Fig. 2.2). These pumps have a big inlet also called vacuum receiver which allows the molecules

in the vacuum chamber to be efficiently collected. When the molecules hit the blades of the turbo pump they gain a momentum in the direction of the roughing pump and then they can be expelled (by the roughing pump). This mechanism can be so efficient that even pressures of 10^{-11} mbar can be obtained inside the vacuum vessel.

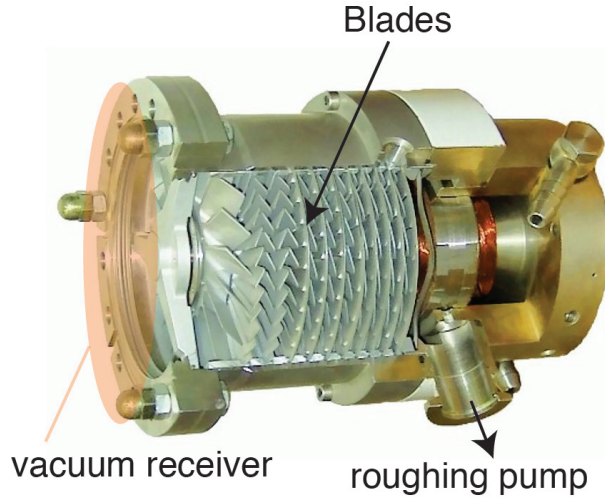


Figure 2.2: **Turbo pump.** Section of a turbo pump showing the blades which create the vacuum, the vacuum receiver which is where the vacuum vessel is attached and the connection to a roughing pump. Re-adapted from [10].

When roughing and turbo pumps are in operation and the vacuum setup reaches a stable pressure (generally at this step $P \approx 10^{-10}$ mbar), the pressure can be maintained by the ion pump. A schematic of an ion pump is illustrated in Fig. 2.3. Generally the minimum pressure to operate an ion pump is $\approx 10^{-7}$ mbar.

The rest gas inside the chamber is ionized by a plasma discharge caused by applying a high voltage (typically ≈ 7 kV) between an anode and a Ti cathode inside the ion pump cavity. The gas as a result of the ionization will be charged and directed towards the Ti cathode. The presence of a magnetic field causes the gas to move in spirals for increasing the probability of ionizing other molecules which contribute to the residual pressure and for increasing their chances to hit the Ti cathode. When the ionized particles

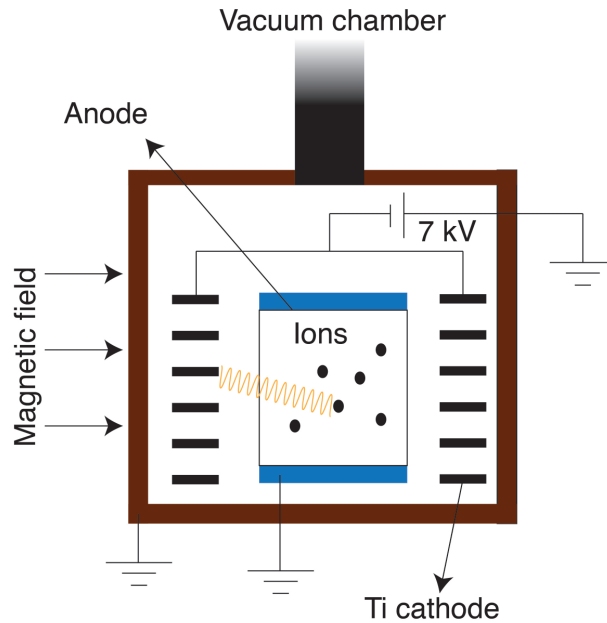


Figure 2.3: **Ion pump.** A schematic showing the working mechanism of an ion pump. A voltage applied between a cathode and an anode creates a plasma discharge which ionizes the rest gas in the pump cavity. The ionized gas hits the Ti cathode and sticks to it, reducing the net pressure of the system.

hit the Ti cathode, they stick to it (this process is facilitated also by the high reactivity of the Ti atoms) and even though they are not expelled directly out of the vacuum chamber, these molecules cannot contribute anymore to the system pressure since they will be stabilized onto the surface of the ion pump's cathode.

Getter pumps are also essential components for maintaining good vacuum conditions in a system and to reduce even further the number of impurities which can stick onto the surface of a sample. The basic idea behind these pumps is to sublime materials with a high reactivity inside the vacuum chamber. Thus, these materials can react with the impurities present in the vacuum vessel, forming a stable solid product which does not contribute anymore to the pressure of the system. The most used getter pump is the TSP. Such a pump consists of a Ti filament through which a current (typically

40 Å) is passed. The Ti is sublimated and the walls of the vacuum chamber will be coated by it. Because of the high reactivity of the Ti atoms, the impurities which hit the walls of the vacuum system will react and stick to them. In this way, the pressure is reduced. This operation is generally done periodically because the Ti coating formed onto the surfaces of the vacuum chamber after a while will not be clean anymore, therefore a new film is needed in order to preserve and improve the vacuum conditions.

2.3 Sample Cleaning

Sample cleaning is probably one of the most important steps in preparing a photoemission experiment. The clean UHV environment typical of a photoemission experiment and described in the previous section, is an important prerequisite to avoid that the system to be studied is affected by external contaminants, such as water, powders and gases present in our atmosphere. Such contaminants in fact can dramatically alter the electronic properties of a system [11], as well as they can be main reason for a reduced sample quality compromising often the ‘goodness’ of the photoemission data: impurities can indeed contribute to increase the scattering centers in the sample resulting, as we will discuss later in this Thesis, in an increase of the background intensity in photoemission data. Whilst UHV technology preserves the sample from external contamination, several materials are necessarily exposed to air after their growth (to be transported to the measurement facilities).

Cleaning such samples is thus a necessary task for ensuring the realization of a successful photoemission experiment and each cleaning procedure is material dependent, meaning that specific cleaning methods are applied to specific samples.

2.3.1 Annealing

Annealing samples is probably one of the most used approaches to remove water and other impurities such as CO_2 and N_2 accumulated onto the surface of the sample after exposure of the sample to air. Annealing consists in supplying thermal energy to a system larger than the thermal desorption energy of the contaminating species. The heat increases the volatility of such contaminants facilitating their removal from the solid matrix where they

stick. The thermal desorption process is generally accomplished by using two different approaches:

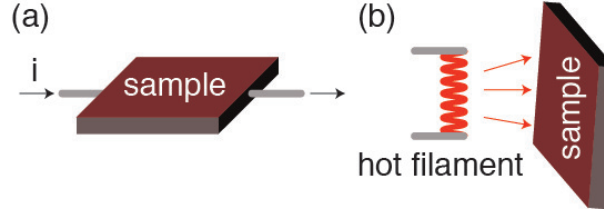


Figure 2.4: **Annealing approaches.** (a) Direct heating process: the current i flows through the sample which is the resistance of the system. As a consequence of this, the sample temperature increases. (b) Indirect heating process: a hot filament is put in proximity of the sample. Thermal irradiation is responsible for increasing the sample temperature.

- *Direct heating:* a voltage is applied to the sample and the current flows through it, limited by the resistance of the sample itself. The sample, acts as an ohmic component and its temperature is increased (Fig. 2.4(a)).

- *Indirect heating:* the heat is generated by an external source, as for example by a hot filament, which is put close to the sample. The sample is then irradiated and its temperature increases (Fig. 2.4(b)). Often, in order to increase the efficiency of this heating method, a positive bias is applied to the sample such that the electrons emitted during the indirect heating process are accelerated against it, further raising up the temperature of the sample. This method is generally called electron-beam heating.

Direct heating is generally used to clean semiconductors, while indirect heating is used for metals and/or insulating compounds.

2.3.2 Ion Sputtering Cleaning

Ion sputtering is an elegant approach able to prepare atomically precise clean surfaces in UHV by ion bombardment. A neutral gas is generally injected into the vacuum chamber at pressures typically on the order of $\approx 10^{-6}$ mbar and through an electron-ionization gun (called a sputter gun) the gas is ionized. A focused ion beam is directed against the sample whose surface is destroyed and hence removed. The gases used for this purpose are generally

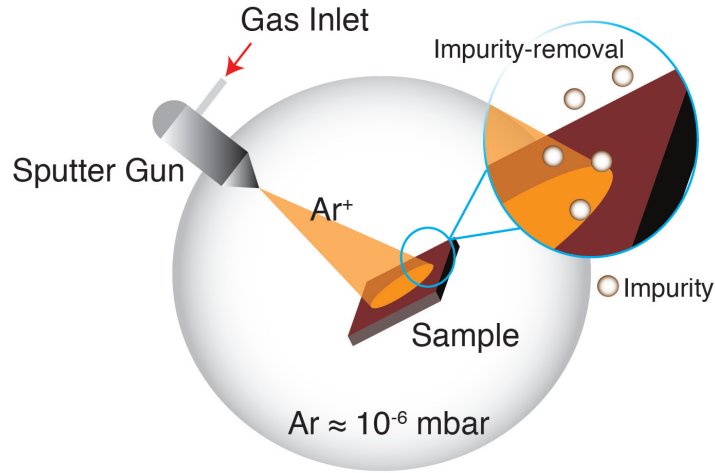


Figure 2.5: **Sputtering process.** An non-reactive gas, such as Ar (or Ne), is leaked into the vacuum chamber. A sputter gun ionizes the Ar gas and the Ar^+ ions are focused onto the sample surface. The ion bombardment removes the first layers of the sample.

Ne or Ar. These gases are chosen because they are inert, thereby they hardly stick onto the sample surface without the risk to be a further reason for contamination [12, 13, 14].

Ideally, by using sputtering, it is possible to remove the surface one monolayer at the time. Unfortunately when light atoms such as carbon are placed on heavy element substrates such as tungsten for example, sputtering can induce C-clusters onto the sample surface, which are difficult to be removed by using conventional cleaning procedures [15].

Generally, using ion sputtering to clean a sample surface creates a large number of defects induced by the ion bombardment. To repair such defects, each sputtering is generally accompanied by a thermal annealing. Indeed, the thermal energy supplied to the sample promotes and mediates the reconstruction of the first surface layers, previously damaged by the ion bombardment.

2.3.3 Cleaving

Cleaving a sample in UHV environment is certainly the best way to get a clean specimen. This method consists in removing a stack of layers at one time from the sample surface such that a new, atomically flat and clean surface is exposed to the UHV environment, preventing any unwanted contamination.

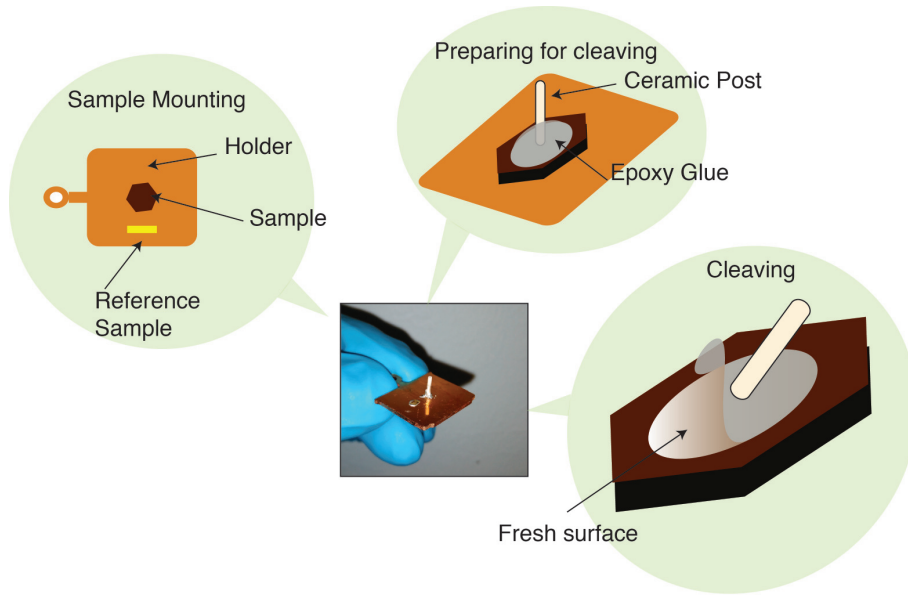


Figure 2.6: **Cleaving process.** At the center: picture of a WSe_2 sample glued on a Cu sample holder where a post used for cleaving is glued is glued, in turn, to the surface. Around: the cleaving process is illustrated. A sample is first glued to the sample holder, then a post is glued on the sample. Finally, by removing such a post, the glue comes away bringing with itself the first surface layers.

This method, despite it is the cleanest way of preparing a surface, it is only applicable to materials whose interlayer coupling strength can be won by mechanical exfoliation. Van der Waals layered compounds are typical examples, among which the most known system is probably graphite. The weak Van der Waals forces which keep the material layers together can be easily broken by mechanical cleavage and/or exfoliation which is commonly realized

by using standard tape or glue. This means that by mechanically pulling the top layers of the sample away from the substrate, a few layers material can be removed altogether and a new surface is obtained. Graphite, transition metal dichalcogenides and topological insulators are examples of these class of materials. A schematic and example of this method is illustrated in Fig. 2.6.

2.4 Sample Growth

In this section I will focus on different approaches we used to grow samples of different thicknesses and architectures. All methods described here are *in situ* growths, meaning that the growth processes have been entirely performed in UHV and that the samples have been transferred into the measurement chamber in such a clean UHV environment without any exposure to air.

2.4.1 Thermal evaporation

Thermal evaporation is a versatile, easy and precise approach to grow nanometer and sub-nanometer scale thin film materials on a substrate. The general idea behind this method is the ability of evaporating different elements or molecules in UHV by supplying them thermal energy. The evaporated substances hit the substrate and stick to it either weakly or strongly, depending on the interaction between the evaporated compounds and the substrate. The strength of the interaction is material dependent and is generally quantified by a material parameter called sticking-coefficient [16] which gives the ratio between the number of atoms which stick on a surface and the total number of atoms which hit the surface in the same amount of time.

The power of this approach truly relies on its versatility. As an example of this, in our works we used thermal evaporation to grow thin films Si (between 0.5 nm and 5 nm), bulk-like (more than 5 nm) and thin molecular films and a fraction of a monolayer alkali atoms. The design for a thermal evaporator is only limited by the designer imagination. For our work, we mostly built two kinds of evaporators: direct heating evaporator, where the material to be evaporated is used as a resistor (similarly to direct heating annealing illustrated in Fig. 2.4) and indirect heating evaporator, where a hot filament warms up a crucible containing the material to be evaporated

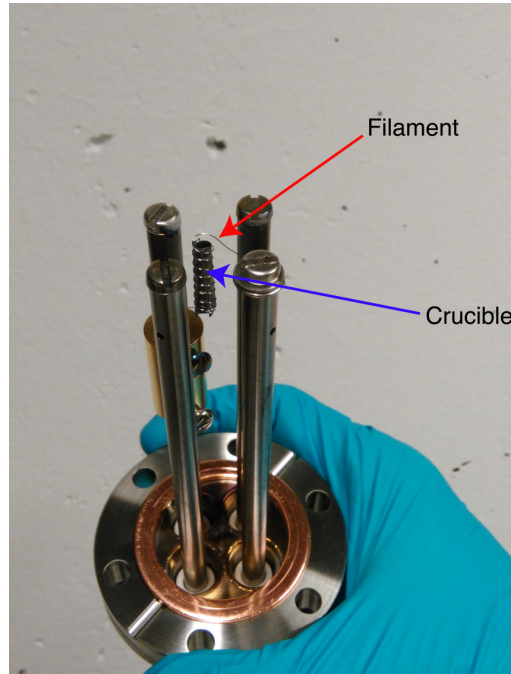


Figure 2.7: **Typical evaporator design.** A filament is wrapped around a crucible inside which the material to be evaporated is placed. When a current flows through the filament, this becomes hot and warms up the crucible. The temperature of the evaporator increases and reaches values comparable to the evaporation temperature of the material to be evaporated.

and for appropriate temperatures such material is evaporated and deposited onto the substrate surface. A home-made source showing an indirect heating evaporator design is illustrated in Fig. 2.7.

2.4.2 Gas dosing

Growing materials onto the top of various substrates is also realized by using gases. A famous example of this, is graphene on metals, realized by the chemistry reaction between the surface and a precursor gas containing carbon [17]. The general idea of this approach is dosing a certain quantity of a gas inside a chamber containing the sample and saturating the sample surface with the gas molecules. Depending on the kind of material, on the kind of

gas and on the kind of final product desired for a certain study, innumerable procedures can be developed exploiting complex chemical reactions, which can be induced by varying parameters such as sample temperature and gas pressure. Specifically, for the works presented in this Thesis, we used H and PH_3 gases on Si(001) to H-terminate and to incorporate P atoms onto the Si surface respectively.

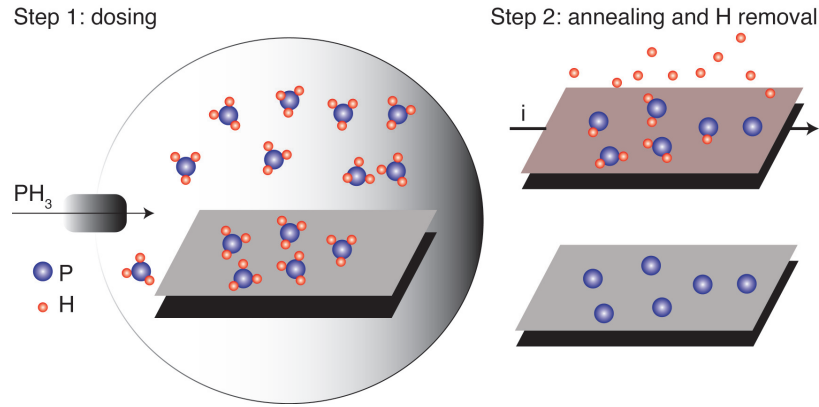


Figure 2.8: **PH_3 dosing.** The PH_3 is dosed into the UHV chamber and it sticks onto the sample surface. By annealing the surface the H is removed and the Si surface becomes covered by only P atoms.

Whilst H-terminated Si(001) is achieved by simply exposing the Si surface to atomic H, the method to incorporate P atoms into the Si lattice is more complicated. We can indeed describe this in two steps: *(i)* PH_3 gas is dosed into the UHV chamber at room temperature and at pressure $\approx 10^{-6}$ mbar. The PH_3 sticks onto the Si surface. Finally, *(ii)* a thermal annealing ($\approx 350^\circ\text{C}$) is sufficient to remove the H and leave behind the P atoms without upsetting their original positions in the sample. This process is a self saturating reaction which results in a P coverage equal to 0.25 monolayer. This process is illustrated in Fig. 2.8.

Chapter 3

Photoemission

3.1 The basic theory

The aim of a photoemission experiment is to describe the behavior of bound electrons in a solid state system. The rigorous formulation of photoemission involves solving the Schrödinger equation for such electrons including their interactions with the atoms and the surrounding environment.

The electrons are not independent from each other and from the solid which hosts them, but their behavior is the result of a thick net of *many-body* interactions. In such a many-body framework, one electron does not move freely into the solid but its dynamics is dominated by the interactions with other entities such as electrons, atoms and electric and magnetic fields which can be applied to the solid or which reside into the solid itself. Giving an exhaustive and advanced theoretical picture of photoemission is a challenging and complicated task which covers a large variety of phenomena and scientific areas, such as many-body physics, quantum-theory, relativity and topology. My goal in this section is to provide a basic theoretical picture of photoemission describing the main concepts which will be necessary for the understanding of the works presented here. Rigorous theoretical descriptions of photoemission have been also already published and available in very well known solid state physics text books [18, 19, 20].

3.1.1 Electronic states

The electrons in a solid can be naïvely divided into two categories: the *core electrons* and the *valence electrons*. The former indicate the strongly bound electrons which are responsible for the formation of the inner orbitals of a certain material. These electrons are, within a simple picture, almost unaffected by small changes in the chemical environment and by crystal field splitting [22]. They are so tight to the nuclei that external perturbations can be considered negligible. They are mostly responsible for screening the positive nuclear charges. Valence electron instead, are responsible for the formation of the energy bands and they are susceptible even to small changes in the local environment of an atom. They are weakly bounded to the nuclei and their modification can result in drastic changes in the material properties, often dominating the phase diagrams of several materials.

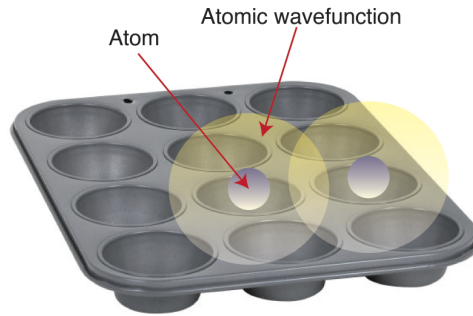


Figure 3.1: **Muffin Tin approximation.** The periodic atomic arrangement forms a periodic potential similar to a muffin tin. The atomic wavefunctions, even though they reside in each of the potential wells, have also a non negligible overlap between different sites. Such an overlap is the origin of the band structure.

A simple illustrative picture to visualize this situation is offered by the *Muffin-Tin* approximation introduced by Slater in 1937 [21]. A periodic array of ions in a solid state system can be regarded to as a periodic potential, whose shape can be picturesquely imagined as a muffin tin. Each hole of the muffin tin corresponds to a potential well where each ion of the lattice resides. For the sake of simplicity, we can imagine the ion to have a spherical wavefunction whose weight is centered in each quantum well. In the interstitial regions such wavefunctions can overlap and the superposition of such

waves gives rise to the electronic band structure of the system (Fig. 3.1). In the muffin tin picture we can immediately spot where the main contributions to the electronic structure of a material are: the shape and symmetry of the wavefunctions is important, as well as the distance between ions and the degree of overlap of their electron wavefunctions. It is also clear that in a crystal, disproportionating the length of the bonds which form the solid can modify the overlap of the wavefunctions and affect their symmetry, thus severe changes in the electronic properties can be naïvely expected.

More rigorously, a particle such as an electron in a periodically repeating environment can be described by a wave ψ , called electron wavefunction. The energies of an electron moving within the constraint of a periodic crystal and more generically of a periodic potential, are solutions to the Schrödinger equation [23]:

$$E\psi(r) = \left[\frac{-\hbar^2}{2\mu} \nabla^2 + V(r) \right] \psi(r) \quad (3.1)$$

In the equation (3.1), $V(r)$ represents the periodic potential created by the periodic arrangement of the atoms in a crystal, μ is the electron effective mass [19]. Given the origin of $V(r)$, this potential carries the same periodicity of the crystal which gives rise to it. If we call \mathbf{G} the vector which connects two repeating unit cells [20, 19], the potential is modeled such that $V(r + \mathbf{G}) = V(r)$. According to the Bloch theorem [24], the electron wavefunctions ψ can be also written in terms of a function $u(r)$ which carries the same periodic relation of $V(r)$ with the crystal, i.e. $u(r + \mathbf{G}) = u(r)$, thus:

$$\psi(r) = e^{i\vec{k}r} u(r) \quad (3.2)$$

where $\vec{k} = (k_x, k_y, k_z)$ is a vector of real number called crystal wave vector or crystal momentum [25] and i is the imaginary unit. The wavefunctions of equation 3.2 are eigenstates of the Schrödinger equation. Generally, the Schrödinger equation can allow for more than one solution for a certain \vec{k} , thus the wavefunction ψ take the more generic form $\psi_{n,\vec{k}}$, with n called the band index, indicating the number of solutions of the Schrödinger equation for a certain \vec{k} .

Fixing n corresponds to fixing a certain energy value (or eigenvalue of the Schrödinger equation). Within one band, \vec{k} varies continuously and so its

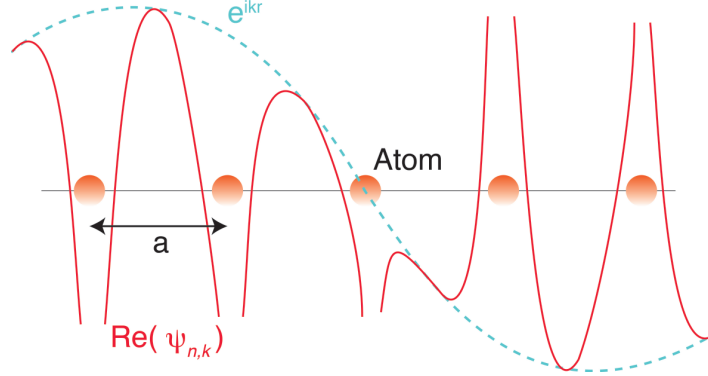


Figure 3.2: **Bloch wavefunction.** The wavefunction, according to the Bloch theorem is a complex quantity, as described by the equation 3.2. The e^{ikr} corresponds to an oscillating phase, dashed blue line in this schematic and its real part consists in a periodic potential created by the atomic arrangement (red solid line).

energy does too, $E_n(\vec{k})$. $E_n(\vec{k})$ is commonly called *electronic band structure*. We remind that the crystal vector \vec{k} is defined in the *reciprocal space* (or *k-space*), whose concept is very well known in condensed matter physics [18, 19, 20], therefore from now on when we refer to energy bands or electronic structures we will assume that these quantities ‘live’ in such a space, unless explicitly specified differently.

3.1.2 From bulk to surface states

In the previous section, I aimed to give a brief description of the main concepts behind an electronic state. Summarizing, an electronic state is described by a \vec{k} -dependent wavefunction $\psi_{n,\vec{k}}$ and by an energy level $E_n(\vec{k})$, which are the eigenstate and eigenvalue of the Schrödinger equation respectively.

Importantly, electronic states are generally described either as *bulk* or as *surface* states. Let us think of an electronic state where the momentum vector \vec{k} is fixed. The number of the possible energy levels at such a \vec{k} value is therefore determined by the numbers acquired by the wave index n . If n is big (theoretically it can acquire infinite values) and the $E_n(\vec{k})$ energies

are infinitely close to each other, the band will look like a whole continuum. Such a continuum is usually regarded to as a unique band, called bulk-band.

Understanding surface states requires understanding what happens to the Hamiltonian of the system when we approach a surface, thus when the material is abruptly interrupted by introducing a termination. For this purpose let us imagine a system which is infinite in two directions, for example x and y , and which presents a termination only at one side, for example along z as in Fig. 3.3(a). The existence of a surface implies a symmetry breaking along the direction orthogonal to the surface and this can introduce new solutions to the Schrödinger equation. Because they originate from the symmetry breaking in the direction orthogonal to the surface, such solutions reside only at the surface.

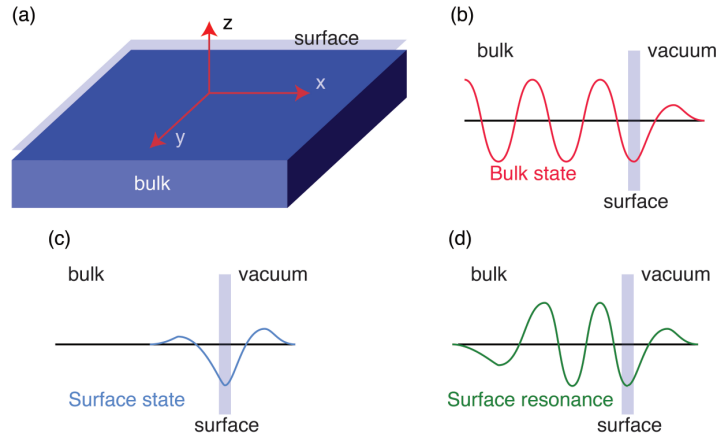


Figure 3.3: **Electronic states.** a) Crystal schematics; the introduction of the surface creates an interruption of the symmetry in the direction perpendicular to the surface itself, z . b) Bulk state: the wave shows a periodic oscillation into the bulk and decays to zero when it escapes the surface. c) Surface state: it is mostly localized at the surface and rapidly decays into the vacuum and into the bulk. d) Surface resonance: it has big amplitude at the surface but it penetrates much deeper into the bulk than a surface state.

Quantitatively, from a electronic wavefunction point of view, we can de-

scribe a bulk state as an oscillating wave which exponentially decays into the vacuum as it escapes the surface, exactly as dictated by the equation 3.2 and depicted in Fig. 3.3(b). A surface state instead, residing only at the material surface, will decay both into the vacuum and into the bulk (see Fig. 3.3(c)). Therefore, surface state solutions to the Schrödinger equation will mostly depend on the in-plane $\vec{k}_{||} = (k_x, k_y)$, whilst k_z contributes only for a phase-modulation. Such solutions can be written as:

$$\psi_{n,k}(r) = e^{i\vec{k}_{||}\vec{r}_{||}} u_{n,k_{||}}(\vec{r}_{||}) e^{-k_z z} \quad (3.3)$$

Equation 3.3 describes the wavefunction for a surface state. In order for such a surface state to exist, it must lie in an energy gap between the bulk bands, otherwise it would be degenerate with one of the bulk states itself.

It is important to mention that the Schrödinger equation admits also solutions which cannot be described neither in terms of surface states nor in terms of bulk states. This is the case of states called *surface resonances*, whose amplitude is exceptionally high at the surface but they decay into the bulk much more slowly than a surface state, penetrating over a long distance from the surface, as in Fig. 3.3(d).

3.1.3 Quantum well states

Another important electronic state of fundamental interest for photoemission and for its potential in possible technological applications is the *quantum well state*. Such a state can occur either when in a narrow region close to the surface a potential is applied to the system or when the physical size of a material is reduced to the atomic scale limit. In both cases, the bulk electronic wavefunctions can be quantized, meaning that the electrons of the bulk states can be ‘trapped’ into such a potential well. This picture is well captured by the famous problem of the ‘electron in a box’ [20, 19]. Such an electron loses its k_z character and it genuinely behaves as two-dimensional. The extent of the quantum confinement affects the breadth of the wavefunction into the solid. Also, states located into a shallower region of the quantum well will be less affected by the potential, thus they will extend more into the bulk than states confined in a deeper region of the quantum well. An example of this has been represented in Fig. 3.4, where I performed numerical simulations for solving the Schrödinger equation for a quantum well created by applying

an electric field at the surface of a certain material.

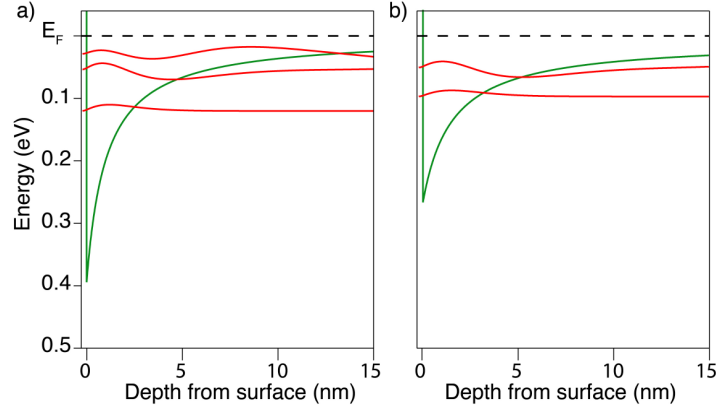


Figure 3.4: **Quantum well states.** Numerical simulation showing the solution of the Schrödinger equation under the assumption of quantum well states created by applying a potential at the surface of the system. The green curve represents the potential profile, the red curves are the wavefunctions. a) and b) only differ for the strength of the potential: the stronger is the potential the bigger the number of quantum states will be.

Now that we characterized the electronic states of a system, it is important to mention that the availability of the electrons residing in such states is dictated by the Fermi-Dirac distribution [26, 27]:

$$f(E, T) = 1/[e^{(E-\mu)/(k_B T)} + 1] \quad (3.4)$$

where E is the energy of the electrons, T is the temperature in Kelvin, μ is the chemical potential of the system considered and k_B is the Boltzmann constant. This law determines the distribution by which in a certain metallic system and at a given temperature, it is possible to find electrons. At $T = 0$ K, the maximum occupied energy level where an electron can be is called Fermi level, generally denoted with E_F . When for metals E_F represents the maximum energy level at which electrons can be found, in neutral semiconductors E_F falls within the bandgap region.

3.2 Introduction to photoemission

Photoemission can be considered a ‘fancy version’ of the photoelectric effect, introduced by Einstein in 1905 [1] and sketched in Fig. 3.5. A photon is

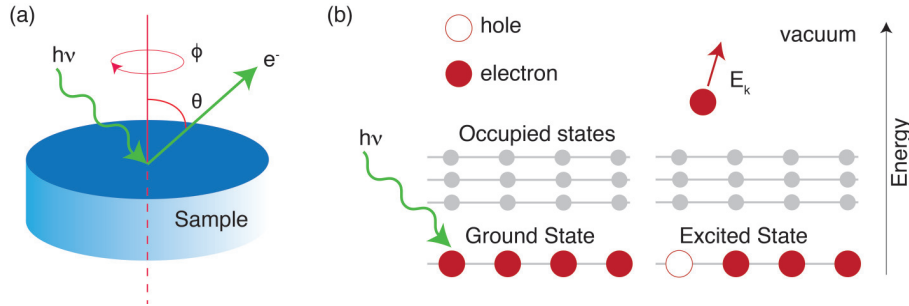


Figure 3.5: **Photoelectric effect.** a) A photon $h\nu$ impinges a sample and excite electrons which escape the material surface with a certain energy and momentum. b) A schematic of the photoemission process for a core level electron.

sent to the sample and impinges its surface. The energy of the photon $h\nu$ is sufficient to extract an electron from the sample and free it into the vacuum with a certain kinetic energy E_k and a certain direction which is a function of the emission angles θ and ϕ illustrated in Fig. 3.5a. In the photoemission process the energy must be conserved, thus:

$$h\nu = E_k + E_B + W_f \quad (3.5)$$

where E_B and W_f are the binding energy and the electron work function respectively. The binding energy is the minimum energy necessary for extracting a bound electron from a solid, the electron work function is the minimum energy necessary for removing an electron from a surface such that any extra amount of energy given to the electron can bring such an electron into the vacuum. In a very simple picture we can think of the photoemission process as divided into three steps. This approximation is called *three step model* [28]: (i) A photon excites an electron; (ii) this electron travels up to the surface and its energy is sufficient to win the electron work function of the material; (iii) the electron escapes the material and goes into the vacuum with kinetic energy E_k . This approach is very simple and unfortunately hides a huge wealth of information. In order to understand what actually is

measured in a photoemission experiment I must introduce a more complex model which goes beyond the simple three-steps approximation.

In this frame, called *one step model*, a photoemission process is described as a transition from an initial state ψ_i (initial electron wavefunction) to a final state ψ_f (final electron wavefunction). Such a transition occurs with a probability which is dictated by the *Fermi's golden rule* [29]:

$$P_{i,f} = \frac{1}{\hbar} |M_{i,f}|^2 \delta(E_f - E_i - h\nu) \quad (3.6)$$

In equation 3.6 the sub-indexes i and f are used to indicate quantities related to the initial and to the final state of the electron respectively. $\delta(E_f - E_i - h\nu)$ is the energy conservation law and tells that a transition between ψ_i and ψ_f can only occur when $h\nu = E_f - E_i$, thus when the photon energy matches the energy difference between the energies of initial and final states. However, the most important parameter in equation 3.6 is the interaction matrix element $M_{i,f}$. $M_{i,f}$ contains all the details regarding the electronic interactions in a system and is directly connected to the Hamiltonian which describes the energetic balance of the material, $M_{i,f} = \langle \psi_f | H | \psi_i \rangle$. H contains information about spins, charges and all the microscopic details dominating the electronic interactions in a solid, more generically it describes the *many-body* nature of the system, which will be discussed in more detail within the next section.

The one step model does not only offer a realistic approach to deal with photoemission but it can be also used to access quantities which are fundamental for transport properties of materials, such as carrier lifetime [30]. For example, without loss of generality we can write the final state for a single non interacting particle as $\psi_f = \sum_n c_f(t) \phi_n e^{\frac{-iE_n t}{\hbar}}$, where ϕ_n are the atomic wavefunctions, t describes the time-evolution of the system and $c_f(t)$ are complex coefficients (for a proper analytical derivation I suggest Ref. [31]). Importantly, we can write such coefficients as $c_f(t) = e^{-\frac{t}{2\tau}}$. In this form, we have access to the time-evolution of the system and in such evolution an important role is played by the constant τ , nominally the *lifetime* of a carrier. τ describes the mean time by which a minority carrier recombines, for example it tells how long it takes for an electron to fill a hole. This quantity is of crucial interest for devices, whose properties (i.e. carrier mobilities and resistivity) fully rely on the carrier lifetimes.

3.3 Many-Body interactions

In this section I want to explain a concept which has been only briefly introduced previously but not dealt in detail: *many-body* interactions in a solid. Let us imagine that a photon impinges a sample. An electron will be freed from the material and will travel into the vacuum. In order to understand what happens to the system and to the electron itself from the moment that such an electron is photo-excited, we need to understand how this electron interacts with the surrounding environment. For simplicity, let us consider the whole system as composed by two main parts: the single electron which is excited by the photoemission process and the remaining $(N - 1)$ -electron system, with N total number of electrons in the solid. The electron initial/final wavefunctions of the whole N -electron system can be now written as:

$$\psi_{i,f}^N = A\phi_{i,f}^k\phi_{i,f}^{N-1} \quad (3.7)$$

where $\phi_{i,f}^k$ is the single particle contribution and $\phi_{i,f}^{N-1}$ is the wavefunction of the remaining electrons. A is a normalization constant. With this definition, the interaction matrix element $\langle \psi_f | H | \psi_i \rangle$ takes the form:

$$\langle \psi_f | H | \psi_i \rangle = |A|^2 \langle A\phi_{i,f}^k\phi_{i,f}^{N-1} | H | A\phi_{i,f}^k\phi_{i,f}^{N-1} \rangle \quad (3.8)$$

This explicit form obtained for the interaction matrix element reveals that the probability of a transition from an initial to a final state does not only originate from the single particle wavefunctions but it also depends on the contributions given by the $(N - 1)$ -electrons and by their interactions with the single electron itself. In addition, the strength by which these interactions manifest is hidden in the Hamiltonian H . This picture is the basis of the *many-body theory*, where an electron is not regarded to as a single free particle but it must be ‘dressed’ with all possible interactions that it has with the atoms and the other electrons in the solid. In these terms, it does not anymore make sense to talk about the electron as a particle, but it would be instead correct to call it *quasiparticle* (quasiparticle=particle + interactions).

In this thesis I will mostly focus on three of the most influent many-body effects: *electron-phonon coupling* [34, 35, 36], *electron-impurity scattering* [36] and *electron-electron interactions* [37]. These effects are indeed visible in photoemission and they manifest with characteristic features in the pho-

toemission spectra. In order to understand these interactions and how they can be detected by using photoemission, I need to introduce the key link between the theory and the experiment. This can be done introducing a quantity called *spectral function* $A(E, k)$. $A(E, k)$ is a functional depending on the electron energy and momentum and it describes the behavior of an interacting electron system, which means the behavior of a system of quasi-particles [32]. In particular, $A(E, k)$ is related to the energy of the interacting electron system which corresponds to a quantity called *self-energy*, $\Sigma = \text{Re}(\Sigma) + i\text{Im}(\Sigma)$. $\text{Re}(\Sigma)$ describes the energy renormalization of the system due to the interactions, $\text{Im}(\Sigma)$ gives a measure of the quasi-particle lifetime. Thus,

$$A(E, k) = -\frac{1}{\pi} \frac{\text{Im}(\Sigma)}{(E - E_0(k) - \text{Re}(\Sigma))^2 + \text{Im}(\Sigma)^2} \quad (3.9)$$

where E_0 is the energy of a non-interacting particle [38].

3.4 Photoemission experiments

A photoemission measurement is closely related to the spectral function of a system; naïvely it can be considered a measure of $A(E, k)$ itself. Specifically, when we acquire photoemission spectra, we are measuring the following quantity:

$$I(E, k) \approx \sum_{i,f} | \langle \psi_f | H | \psi_i \rangle |^2 A(E, k) \quad (3.10)$$

Equation 3.10 is all we need to imagine how photoemission spectra look. As an example, if we combine equation 3.10 with the spectral function explicit form (equation 3.9), we can find out that the line-shape of photoemission spectra has a Lorentzian profile [38].

An important remark is that photoemission is a surface sensitive technique due to the short escape depth (nanometer-scale) of the outgoing electrons. In addition, because of the symmetry breaking at the surface of a crystal, k_z is not a good quantum number and the only component of \vec{k} conserved in the photoemission process is $\vec{k}_{||}$.

3.5 Mapping the electronic structure of solids

So far, I introduced how at the basis of the photoemission process, there is an electron excited by a photon. Such an electron carries a momentum \vec{k} and kinetic energy $E_{\vec{k}}$. In this section, I want to answer the question: how can we measure \vec{k} and $E_{\vec{k}}$ experimentally?

A typical experimental photoemission setup consists of three main parts: (i) the vacuum vessels (maintained in UHV through a pumps system, as described previously), (ii) an X-ray source and (iii) an electron analyzer. The *vacuum vessels* are generally non-standard and they are only limited by the designer imagination and by the kind of operations that a system is dedicated for. For example, it is common to find systems divided into two main chambers, an analysis chamber and a preparation chamber. The analysis chamber is supposed to be kept in good vacuum because is used for the measurements; in the preparation chamber materials can be grown and cleaned without necessarily having perfect UHV conditions (even though UHV is still desirable for a clean growth). As an example, in Fig. 3.6 I show the preparation chamber that we designed installed in our ‘home-lab’. We designed this chamber for growth purposes. It has 8 ports where evaporators and gas lines can be installed. In this system the sample is placed at the center of the main body and can be put in front of each of the 8 ports, ensuring a giant versatility for dosing different gases, molecules and atoms.

The *X-ray source* is a device used to produce photons, therefore necessary to start a photoemission process. Several kind of sources exist: lasers, ordinary X-ray generators (X-ray guns and gas-lamps) and synchrotrons. The differences between these sources are huge and a full description goes well beyond the aim of this work. I will only say that the essential difference between a synchrotron and usual lasers and X-ray generators is the possibility for the synchrotron to allow a broad photon energy range for the excitation process, in contrast to the other sources which only offer a few photon energies for this purpose. The works presented in this Thesis have been mostly carried out at synchrotron facilities because most of the samples’ spectra were visible only at particular values of photon energy. The photon energy used, in fact, limits the availability of final states and the probability of transitions between initial and final states. In other words the Fermi’s golden rule is photon energy-dependent.

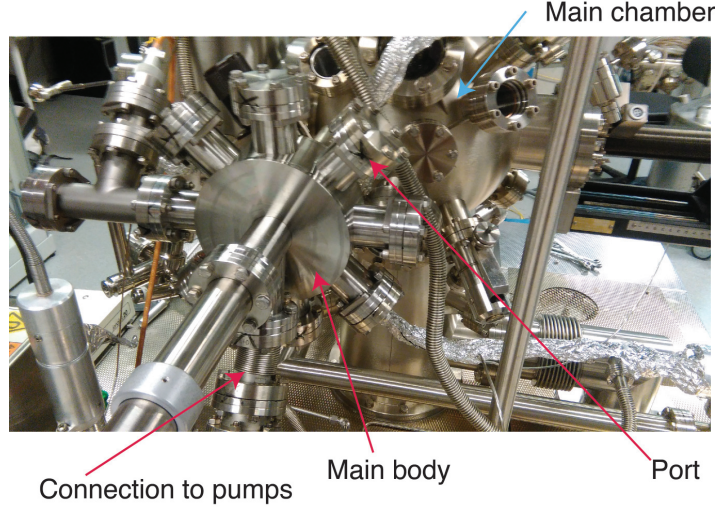


Figure 3.6: **Custom-made growth chamber.** Growth chamber designed and mounted in our lab at Trondheim. It consists of a main body where a sample can be placed and 9 ports. One port is used as a connection to the pump system, such that UHV can be ensured, the other 8 are versatile: evaporators and/or gas lines can be attached to each of the ports making the chamber small and powerful growth system.

When the electrons are extracted from the solid matrix and acquire energy and momentum, they must be collected and measured. This job is done by the *electron-analyzer*. A schematic of this important component is shown in Fig. 3.7. The analyzer, also called spectrometer, consists in a series of electrostatic lenses which focuses the photoemitted electrons into an entrance slit separating a hemispherical body from such lenses. The hemispherical body consists of two plates where different voltages are applied, creating in this way an energy band filter. The voltages applied to the hemispherical plates are tuned such that only electrons with energy $E_{orbit} = E_P \pm \Delta$ can pass through the plates without hitting them (the electrons which hit the plates will be at the same potential of the chamber and they will be lost). E_P is called pass energy and corresponds to the energy of an electron which goes through the plates of the spectrometer following a perfectly circular trajectory around the center of the analyzer. E_P also defines the resolution of a

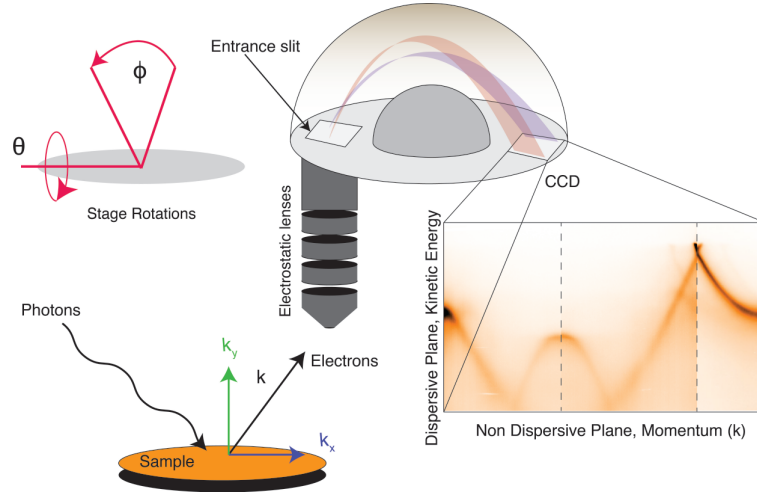


Figure 3.7: **Measuring electrons.** The electrons emitted by the sample during a photoemission process are collected by an electron analyzer. The electrons have a certain speed (thus energy) and momentum (\vec{k}). The spectrometer will collect them as function of both energy and momentum. The image color shown is a typical example of ARPES spectra, collected for graphene.

photoemission experiment. Δ is the energy window of a photoemission acquisition.

Once the electrons with energy E_{orbit} travels through the plates they will be collected by a CCD camera which measures their angular and energy distributions. The faster electrons will make a larger orbit with maximum energy $E_P + \Delta$, the slower will make a smaller orbit with minimum energy $E_P - \Delta$. The energy distribution is measured along the orbit direction, in the plane of the analyzer called ‘dispersive plane’ (see Fig. 3.7). In addition, the photoemitted electrons will escape from the sample at different angles. Thus, they will have an angular distribution (along the ‘non dispersive plane’ of Fig. 3.7) which is also measured by the analyzer. It is important to mention that the angular acceptance is selected by the lenses.

Whilst it is clear to understand that in a photoemission experiment the energy is measured, it is not obvious how this is also true for the momentum.

However, measuring angles and momentum is basically the same thing; taking into consideration of a sample with the degrees of rotation of Fig. 3.7, the momentum can be found as:

$$k_{\parallel} = (\sin \phi \hat{x} + \cos \phi \sin \theta \hat{y}) \sqrt{\frac{2m_e E_k}{\hbar^2}} \quad (3.11)$$

where m_e is the electron mass and all the other quantities have been already introduced.

Summarizing; by using photoemission we are able to detect the energy and momentum distributions of the photoemitted electrons.

3.6 2D and 3D mapping

When measuring a sample, we always have to bear in mind that the presence of a surface constitutes the breaking of the crystal translation symmetry along the direction orthogonal to the surface plane. This is the reason for which in a photoemission process the only conserved component of the momentum \vec{k} is \vec{k}_{\parallel} . Therefore, photoemission spectra are snapshots of the energy (kinetic energy or binding energy related by equation 3.5) as function of the momentum \vec{k}_{\parallel} . However, we briefly mentioned already that the transition between initial to final states occur with a certain probability, which depends on photon energy. In addition $A(E, k)$ depends on photon energy too. At first glance, it is difficult to see how $A(E, k)$ depends on $h\nu$. This anyway becomes clear as one considers that every quantity which depends on \vec{k} , contains also a contribution from the non-conserved quantity of the momentum k_z , which is energy dependent. Indeed we can write k_z as:

$$k_z = \sqrt{\frac{2m_e}{\hbar^2}(V_0 + (h\nu - E_B - W_f)\cos^2(\theta))} \quad (3.12)$$

where the only new quantity introduced here is the *inner potential* V_0 , which corresponds to an averaged-value of the electrostatic potential in a volume of the material considered (typically $V_0 \approx 10$ eV).

Equation 3.12 not only is important because it dictates whether a photoemission process is feasible but it also suggests that a route to measure the electronic structure of a system along k_z is to vary photon energy. This

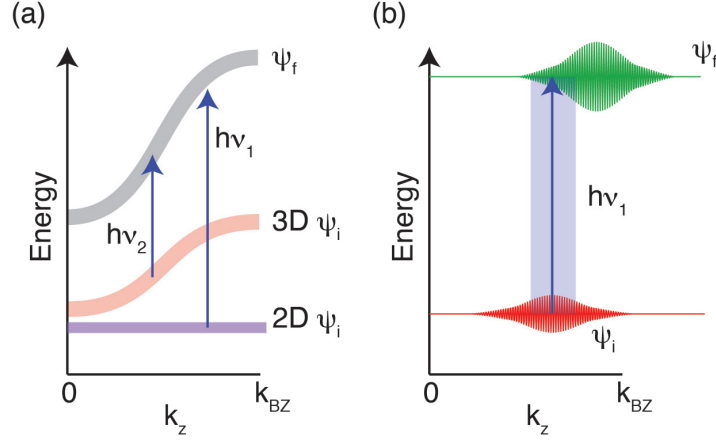


Figure 3.8: **Electronic states, 2D and 3D.** a) Schematic of a photoemission process from 2D states and 3D states to a final state. b) Photoemission process for a generic final state: the transition from an initial to a final state can occur when the convolution of the initial and final wavefunctions is non-zero. In other terms, the broadening in k_z must be taken into account for possible transitions from an initial to a final state.

leads to an important consideration: for materials which are purely two-dimensional (2D) or whose wavefunctions are localized within single layers (such that the out-of-plane orbitals have a negligible overlap along the direction orthogonal to the layers), the electronic structure will be dispersionless in k_z . Conversely, materials whose out-of-plane orbitals strongly overlap in the z direction will have an electronic dispersion in k_z .

In conclusion, even though k_z is not a good quantum number, it is a quantity of fundamental interest to understand the dispersion of the electronic structure along the direction orthogonal to the surface, the selection rules which dictate the probability of a photoemission process and ultimately, the electronic dimensionality of materials.

In Fig. 3.8(a) I show the difference between initial 2D and 3D states: for a certain value of k_z , photoemission to a final state (of known shape) will be possible only at a particular value of photon energy. A 2D electronic band

has a dispersionless initial state in k_z , while a 3D state disperses along this direction. This simple picture can be more realistic if we do not make any assumption regarding the form of the final state. In such a situation, illustrated in Fig. 3.8(b), both initial and final states are well described by generic Bloch wavefunctions. Such Bloch wavefunctions have a finite extension in k_z captured by their envelop. An electronic transition can occur when the overlap between the initial and final wavefunctions is not zero. This means that a transition between a certain initial state to a certain final state will not necessarily occur at one particular match of $h\nu$ and k_z , but there are more combinations of $h\nu$ and k_z for which transitions are allowed. This fully reflects the finite extension of the electronic wavefunctions in k_z . However, such transitions will occur with different probability depending on the degree of overlap between initial and final states, nominally their convolution. When the convolution is maximum, the intensity of the photoemission event is maximum too, in agreement with equation 3.10.

Chapter 4

Main photoemission techniques used in this work

Photoemission is an incredibly versatile tool to access the electronic properties of solid state systems. Over the last five decades several techniques have been developed exploiting this fascinating effect and all of them constitute a powerful approach to investigate different aspects of spin and charge degrees of freedom of materials. Each technique exploits the same photoemission principles discussed so far but technical and instrumental differences make each technique unique and specialized for a particular purpose. An example is spin- and angle resolved photoemission spectroscopy where the addition of a spin-detector to the photoemission system not only allows us to resolve the energy and momentum but it also accesses the knowledge of the spin-polarization of the electronic bands. My goal here is not to give the details of the technical design and characteristics of the instruments based on photoemission, but I will briefly summarize which techniques I used for the works in this Thesis and give an idea of what such techniques can do and resolve.

4.1 Angle-resolved photoemission spectroscopy, ARPES

Angle-resolved-photoemission spectroscopy (ARPES) is a powerful experimental technique which allows to access the electronic structure of materials, resolved in angle (therefore momentum) and energy. It is probably the best

technique to directly match a data acquisition with the theoretical spectral function $A(E, k)$ introduced in the previous chapters. The visual information we get out from an ARPES experiment is the number of photoelectrons resolved in energy and momentum, as represented by equation 3.10. Each ARPES spectrum carries information about the many-body effects in the solid, exactly as $A(E, k)$ does. An important task is therefore to understand how it is possible to disentangle all these contributions within a single measurement.

In order to understand what ARPES can offer, let us start by taking a theoretical band structure for a free-electron gas, represented by a simple parabolic dispersion as in Fig. 4.1a. To make such a dispersion more realistic we can add a broadening in energy and momentum to account for the experimental resolutions of the instrument (see Fig. 4.1b). However, in a real experiment the measurement system is not the only factor which contributes to a band broadening but also many-body effects must be considered. Such many-body effects modify the real and imaginary part of the self energy ($Re(\Sigma)$ and $Im(\Sigma)$ respectively), quantities introduced in the previous sections and directly responsible for the outcome of ARPES spectra. This means, that the energy renormalization and energy-momentum broadening will be dominated by the effects that many-body interactions will have on the self energy. Among the many-body interactions, the biggest contribution comes usually from electron-impurity scattering, electron-phonon coupling and electron-electron scattering.

Electron-impurity scattering can be generically described as a constant contribution to $Im(\Sigma)$, manifesting as an increase of the line-widths of the ARPES spectra both in energy and momentum. Adding this effect to the spectral function leads to the spectra in Fig. 4.1c: such a band looks broader than the one illustrated in Fig. 4.1b. Electron-impurity scattering is always present in real ARPES experiments and contributes to the lifetime of the quasiparticles. The quasiparticle lifetime is indeed related to $Im(\Sigma)$ ($\propto Im\Sigma^{-1}$) and changing $Im(\Sigma)$ produces changes in the spectral line-width. Therefore, giving an estimate for the line-width broadening of ARPES spectra can be regarded to as an estimate for the quasiparticle lifetime.

Electron-impurity scattering also contributes for the intensity of the background in ARPES spectra. Indeed, the presence of impurities in a sample

opens possible channels for the electrons in the material to scatter. In order to simulate realistic ARPES spectra, a random scattering background has been considered in Fig. 4.1 for all our simulations.

Electron-phonon coupling is a many-body effect which manifests when an electron couples with a lattice vibration, i.e. a phonon. This effect, has important implications for transport properties, for example in metallic conductors it is usually the main responsible for an increase of the material resistance. In addition, whilst electron-phonon coupling is primarily responsible for electrical losses in standard conductors, it is also able to give superconductivity. Only including electron-phonon coupling, according to the standard theory of BCS superconductors introduced by Bardeen, Cooper and Schrieffer [43], two electrons with opposite spin can be coupled together (forming a Cooper pair) and move through the lattice free of resistance. Thus, by understanding and controlling electron-phonon coupling, we could potentially go from high-loss systems to lossless ones, which is a very up-to-date problematic concerning the energy consumption.

The central property in the description of electron-phonon coupling is the Eliashberg function [42], a quantity which contains information about the phonon density of states and their coupling with the electrons (Eliashberg function: $\alpha^2 F(\omega)$; α quantifies the strength of the coupling between the electrons and the phonons; ω is the energy and $F(\omega)$ the phonon density of states). Through this function, we can write the electron-phonon coupling contribution to the self energy as:

$$E_{el-ph} = \int dE_0 \int_0^{\hbar\omega_{max}} d(\hbar\omega) \alpha^2 F(\omega) \times \left[\frac{1 - f(E_0, T) + n(\hbar\omega, T)}{E - E_0 - \hbar\omega} + \frac{f(E_0, T) + n(\hbar\omega, T)}{E - E_0 + \hbar\omega} \right] \quad (4.1)$$

where $\hbar\omega_{max}$ is the maximum phonon energy of the system, $f(E, T)$ and $n(E, T)$ are the Fermi and Bose electrons distributions respectively. The equation 4.1 represents the integral over all the electrons and phonons states including their coupling probability. An important quantity which can be extracted from the Eliashberg function is the strength by which electrons and phonons can couple. Such a strength is generally described either in terms of α or, more commonly in terms of the renormalization parameter λ :

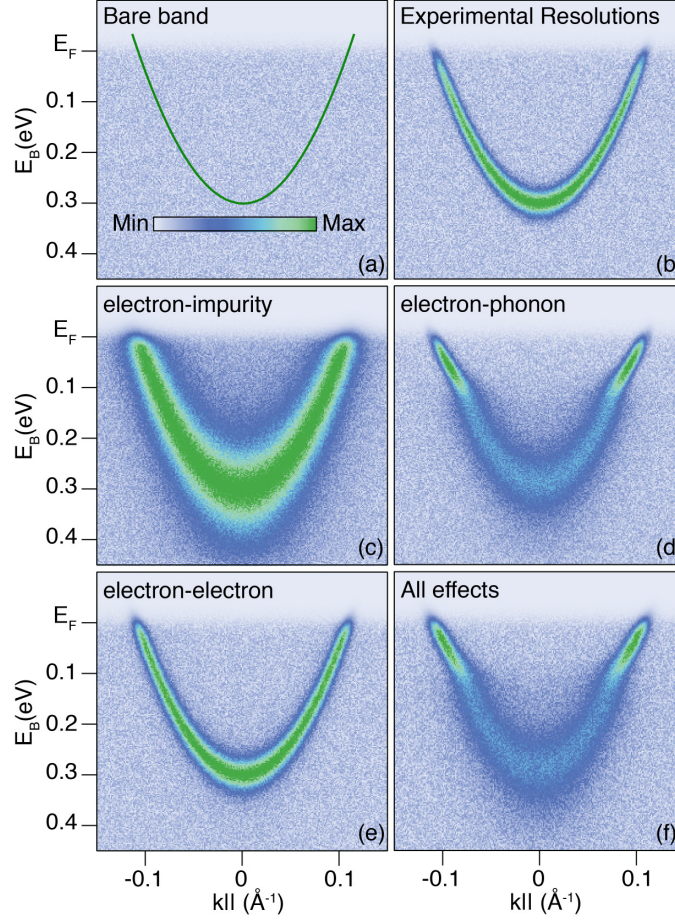


Figure 4.1: **Many Body Interactions.** a) A bare band over a background for a free electron represented by a parabola. b) The bare band has been broadened by 40 meV and 0.01 \AA^{-1} to account for the energy and momentum resolutions respectively. c-e) The band structure of (b) which has now been dressed with many-body effects, specifically electron-impurity, electron-phonon and electron-electron interactions. f) All effects have been included into the model to simulate a realistic dispersion.

$$\lambda = 2 \int_0^{\hbar\omega_{max}} d(\hbar\omega) \frac{\alpha F(\hbar\omega)}{\hbar\omega} \quad (4.2)$$

λ , also called mass-enhancement parameter, is a measure of the increase in the quasiparticle mass once the electron-phonon coupling is turned on: the single electron particle is indeed ‘dressed’ by many-body effects and the new system, i.e. quasiparticle, will appear heavier. This parameter is essential in the description of superconductivity and qualitatively one can state that, at least for BCS theory, it becomes the driving force for the Cooper pairs formation when it reaches values $\lambda \approx 1$, or alternatively when the quasiparticle mass doubles as effect of the electron-phonon coupling. In order to estimate this parameter from ARPES spectra, several methods have been developed. The works in this Thesis are based on the Debye and Einstein approximations. Their description goes beyond the aim of this work, but details about these models can be found in Ref. [38]. Electron-phonon coupling in ARPES spectra generally manifests with a ‘kink’ in the electronic dispersion as in the bands of Fig. 4.1d, due to a sudden increase in $Re(\Sigma)$.

Electron-electron scattering is probably the most complicated effect to be understood. The interplay of Coulomb repulsions between the electrons and their mutual interactions can be orbital and element dependent. This effect can lead a material to undergo several exotic phase transitions, such as metal-insulator, superconducting and charge density wave transitions. It is also strongly influenced by the atomic arrangement of the crystal and even small modifications in the lattice (for example induced by the crystal field and/or Jahn-Teller effects [44]) can strongly redistribute the energetic balance of the material, breaking the quasiparticles into collective excitations. In the simplest 3D Fermi liquid scenario, electron-electron scattering can be well approximated as:

$$E_{el-el} = \gamma E + i\beta[E^2 + (\pi k_B T)^2] \quad (4.3)$$

where γ and β constant parameters which quantify the energy renormalization and strength of the broadening respectively [39, 40, 41]. Fig. 4.1e is a simulation of an ARPES measurement where electron-electron scattering has been included, according to the equation 4.3, with temperature $T = 300$ K. Generally, at energies close to the Fermi level, electron-electron scattering is considered negligible and the many-body nature of the system is dominated

by electron-phonon coupling.

In Fig. 4.1f we introduced a model which takes into consideration of all the many body contributions described and the experimental resolutions of the instrument. In this particular case, electron-phonon coupling is the most influent effect, as demonstrated by a ‘kink’ happening at energy close to the Fermi level.

4.2 Spin-ARPES

Understanding and controlling the spins of electrons has recently attracted enormous interest. Developing new technology where currents can be produced without requiring the motion of charged particles but obtained through a change in the particle spin, can pave the way for low-dissipation electronic devices. If in a material each spin can be manipulated, a spin-current can be realized too. Such a current will be produced without moving the electrons of the system, thus heat loads generated could be reduced and the yield of devices enhanced. Producing spin-currents is the concept at the basis of exotic spin-based devices such as spintronics and valleytronics [45, 46], conjectured as possible substitutes of the technological devices that we know today.

Over the last decades, several methods to detect the electron spin have been suggested. I will here focus on Mott polarimeters, due to the relevance of these devices for the works presented in this Thesis. In order to understand such devices, I need to introduce the concept of Mott-electron-scattering, a process named after the physicist Nevil Mott who first understood, in 1929, how the scattering of an electron from a heavy target is spin-dependent [48].

For simplicity, let us consider an electron moving towards a heavy-element target. Materials with high atomic number generally host a big *spin-orbit-coupling*, which is the property of an electron to couple its spin to its orbital motion. The presence of this effect introduces a spin-dependence in the scattering cross section: when an electron travels towards the target, an electric and a magnetic field are created. Because the electron has a spin-angular momentum the force exerted by the magnetic field on the electron will depend on the spin carried by the electron, thus affecting its scattering.

If a beam of electrons has in average equal spins ‘LEFT’ and ‘RIGHT’, the scattering between such a beam and the target will give in average the same number of electrons having been scattered left and right as in Fig. 4.2(a). Otherwise, if the number of electrons with spins ‘LEFT’ and ‘RIGHT’ is in average not equal, the electrons will scatter preferentially towards one direction, as illustrated in Fig. 4.2(b). In this case the beam is called *spin-polarized*.

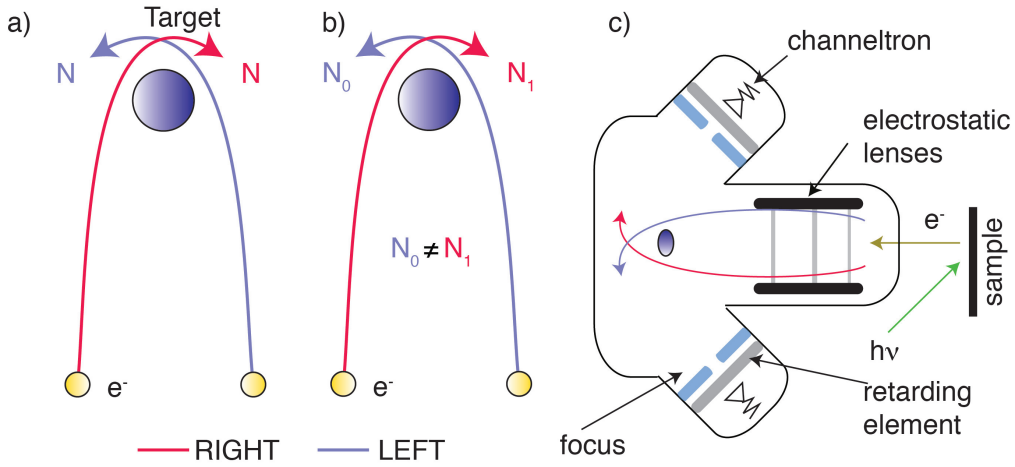


Figure 4.2: **Spin-dependence of the electron scattering.**

a) A beam of electrons with equal number of spin ‘LEFT’ and ‘RIGHT’ scatters from a target. The scatter will be symmetric: the electrons will be scattered in equal number towards the left and the right. b) A polarized beam is directed towards the target. The electrons will be scattered mostly towards a certain direction, in this example towards the left.

A Mott-polarimeter is a detector with a target made of heavy elements, which is able to detect the electron currents in different directions after the electrons have scattered with the target (Fig. 4.2(c)). This means, that in terms of electron currents, a Mott-polarimeter will detect the asymmetry in the backscattering events as:

$$P = \frac{I_L - I_R}{I_L + I_R} \frac{1}{S} \quad (4.4)$$

where I_L and I_R are the currents of the scattered electrons in ‘LEFT/RIGHT’ directions. P defines the spin-polarization of a system and S is the *Sherman function*, a normalization parameter which describes the polarimeter’s analyzing power. S mostly depends on the target material, on the energy of the incident electrons and on the target thickness.

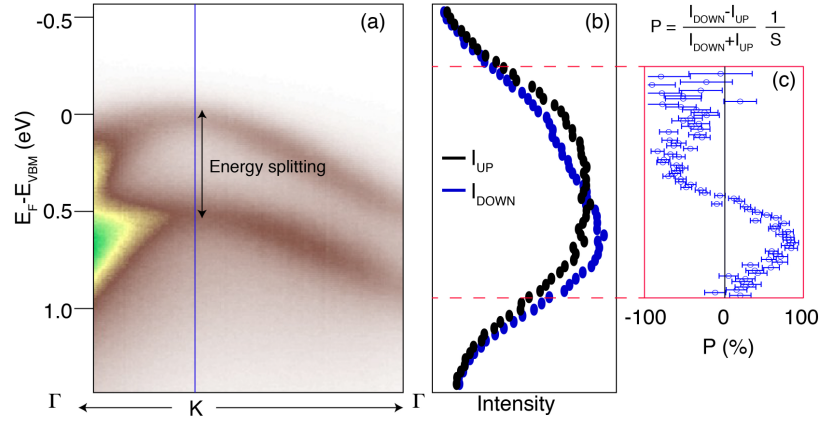


Figure 4.3: **Spin-polarization in WSe₂** a) ARPES measurement for ₂ acquired along the direction $\Gamma - K$ of its Brillouin zone. The energy scale is relative to the maximum of the system’s valence band. b) Electron currents collected for the spin ‘UP’ and spin ‘DOWN’ electrons using a Mott-polarimeter. The measurement has been performed along the cut represented by the blue line in b). c) Spin-polarization P extracted from b) using equation 4.4.

Spin-ARPES experiments are generally really slow, because Mott detectors are quite inefficient. For certain materials it can take up to more than 12 hours of acquisition time for a single measurement. For some materials however, with bands hosting a big spin-orbit coupling, this technique can be the turning point to understand the spin-polarization of such bands. As an example, in Fig. 4.3 I reported a typical spin-ARPES acquisition for measuring the spin-polarization of the bands of WSe₂ at the K point of its Brillouin

zone. In this case, we measured the out-of-plane spin polarization along the energy cut shown in Fig. 4.3a (blue line). The detector measures separately the electron current of electrons with spin ‘UP’ and of those with spin ‘DOWN’ (Fig. 4.3b). Then, the polarization P is found using the equation 4.4 (Fig. 4.3c).

In conclusion, even though Mott polarimeters are inefficient devices, they still constitute a valuable and powerful approach to broaden the understanding of the collective behavior of the spin of the electrons in a solid. This can open important routes towards manufacturing electronic devices, able to generate currents by controlling the electron spins.

4.3 X-ray photoemission spectroscopy

X-ray photoemission spectroscopy (XPS) is an experimental technique able to measure the chemical composition and the electronic state of a certain system. This technique measures the number of photoelectrons with a certain kinetic energy and emitted at a certain angular range. The angular range, as mentioned previously, is fixed by the lens modes.

For the sake of visualizing the outcome of this technique, single XPS spectra can be naïvely thought as ARPES spectra which have been integrated in angle (or momentum). Even though this might appear as a disadvantage with respect to ARPES due to the lack of angular resolution, XPS is extraordinarily powerful for other kinds of analysis, such as X-ray core level spectroscopy. This name reveals that the available photon energies used for this technique are able to reach even deep core levels (generally between 100 eV and 10 keV).

We must remember, that when an electron is emitted from an initial state, the photoemission selection rules dictate the final state of the photoemission process [49]. Thus we can expect that the line-shape of XPS spectra not only will carry information about the interacting electron initial state, but also about final state effects. This adds another layer of complexity to this technique whose spectra can be used to understand complicated physics processes, elusive to several other technique such as ARPES and spin-ARPES.

XPS has also the advantage over many techniques to be applied to a large

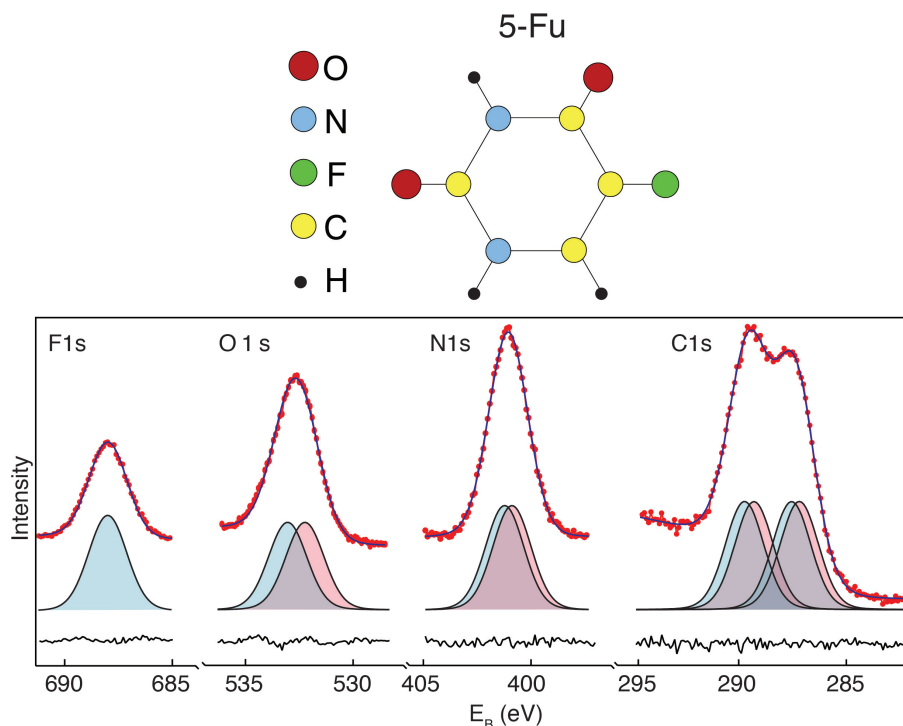


Figure 4.4: **Quantitative analysis of 5-Fu bulk.** F1s, N1s, C1s and O1s core levels acquired using XPS. The red curve with markers represents the raw data while the blue solid line is the fit of the experimental data. The intensity areas of the components inferred by the fit results and the residual (difference between experiment and fit) are plotted to give a quantitative estimate of the molecular stoichiometry and goodness of the fit, respectively.

variety of materials, without necessarily the restriction of dealing with single crystals domains. It has been demonstrated over the years to be extremely powerful in revealing the chemical and physical properties of organic materials, allowing the detection of rather complicated molecules.

As an example of this, in Fig. 4.4 I show how we used XPS to characterize the most used drug in the treatment of cancer, 5-Fluorouracil (5-Fu). 5-Fu is an organic molecule composed of four C, two N, two O and one F, arranged as in Fig. 4.4. We evaporated this molecule on a substrate and we want to

check whether the molecule gets damaged by the evaporation process. XPS measurements from 5-Fu bulk (a thick enough layer to be considered bulk-like within our depth sensitivity, i.e. more than 5 nm) reveal details of the single molecular constituents, nominally the core level F1s, O1s, N1s and C1s. The XPS spectra can be fitted assuming a Lorentzian lineshape (predicted for photoemission spectra as discussed previously) convoluted to a gaussian which accounts for the energy resolution of the instrument. By analyzing the areas of the photoemission peaks, we can infer the stoichiometry of the molecule, giving F:O:N:C corresponding to 1 : 2 : 2 : 4, in agreement with the configuration of an ‘intact’ molecule. There is more than this: XPS peaks are sensitive to the atomic arrangement. For example, the N1s peaks in Fig. 4.4 fall almost at the same binding energy; this is not unexpected either, because the two N atoms which give rise to such peaks have a very similar atomic surrounding. Hypothetically, if the atomic surrounding is dramatically changed, we can expect that the two peaks giving the N1s lineshape would appear as distinct features.

It is relevant to mention that XPS on these organic molecules can be done very efficiently and with a very low beam-flux. Thus, within the short time needed for acquiring single XPS spectra, we can even measure molecules which would in principle be affected by radiation-damage. In the case of 5-Fu, no beam damage was observed within the acquisition time.

4.4 Resonant Photoemission Spectroscopy

Resonant photoemission spectroscopy (RPES) is an approach which exploits a basic photoemission technique (such as XPS and ARPES) to probe and track the atomic and orbital character of the wavefunctions which give rise to the electronic structure of a certain system.

In other words, the band structure of a solid originates from the bonding and antibonding combination of the orbitals of the material. In a complex material where many elements are present, each element can contribute, to a different extent to the orbital character of the system. If we now want to probe a particular elemental contribution to the band structure, we need to ‘select’ the element we want to study, i.e. consider an arbitrary element ‘A’.

This can be done by choosing the photon energy to match an absorption edge of ‘A’. Doing this corresponds to selectively enhance the signal intensity of an electronic band structure whose contribution comes from the element ‘A’. If now we repeat this procedure for all the other elements which contribute to the electronic structure of a material, we can ‘see’ how they contribute to the band structure separately. The intensity of a spectral feature which originates from a particular element is therefore resonantly enhanced in the photoemission process if the photon energy is chosen to match the energy of the absorption edge of the element itself, hence the name resonant-PES.

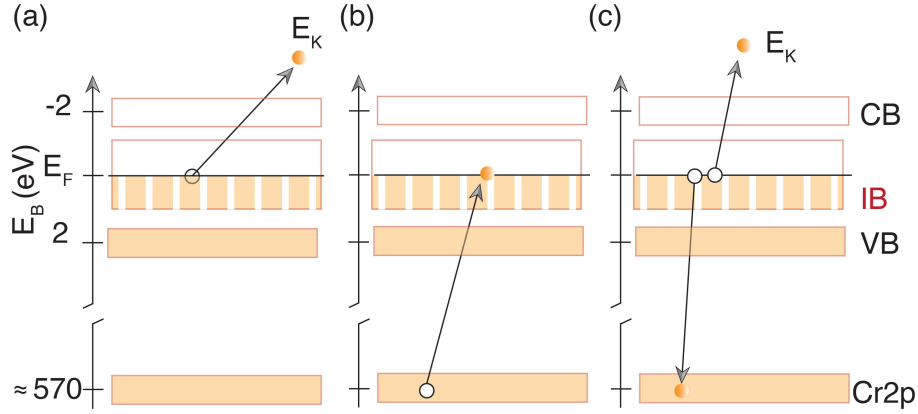


Figure 4.5: **Example of RPES for Cr-doped ZnS, a schematic.** (a) Representation of the standard photoemission process: an electron is emitted from the IB (Cr3d in this illustration). (b) and (c) A secondary, 2-step, process: (b) the electron can be first excited from Cr2p into the Cr3d/IB state. (c) The Cr3d electron may then decay back to the Cr2p band by emission of another Cr3d electron. Both process ultimately lead to emission of a Cr3d electron and have the same initial and final states.

This technique can be also elegantly applied to several materials with no particular *a priori* restriction on their crystallinity. RPES is generally used to disentangle orbital contributions to targeted electronic states, even though the absence of a large area single crystal domain would not allow the band structure to be resolved by conventional photoemission techniques. Let us

imagine a semiconductor with a wide bandgap and let us assume that a very low content of impurities (less than 5% of the total amount of the semiconductor's components) have been implanted into the bulk to create partially-filled electronic states with energies within the band-gap (also called, in this particular case, intermediate band, IB). In normal circumstances, it would be difficult to 'see' such states at all by using XPS or ARPES because of the low contents of impurities, polycrystallinity and background intensity. By 'usual' photoemission, electrons residing in these partially filled states will be emitted and they will escape into vacuum with kinetic energy E_k .

By using photon energy corresponding to the energy of the absorption edge of these impurities two processes can happen. First, the 'usual' photoemission process takes place emitting an electron with energy E_k , as in Fig. 4.5a. Second, an electron can be promoted, selection rules allowing [49], into the partially-filled state within the band gap. Such an electron leaves behind a hole which is filled by another electron in the partially-filled states (Fig. 4.5b). To equilibrate the energy balance, a third electron is emitted with energy E_k (Fig. 4.5c). The two electrons photoemitted in this process have the same kinetic energy, hence the same final states, and they interfere creating a resonant enhancement of the photoemission intensity. In this way, the partially-filled state within the band gap can be directly accessed, giving information about the electron filling and orbital contributions; these quantities would not be otherwise detected for energies other than the absorption edge because of a too small photoemission signal. In addition, RPES is a powerful approach to understand the selection rules of the excitation process, and ultimately the nature of the excited state.

Chapter 5

Main Materials

In the previous chapters I tried to give the ingredients necessary to understand photoemission and I also briefly introduced the main photoemission-based techniques which have been used for the papers presented here. Several materials have been also mentioned but I have never given a full and exhaustive description of what they actually are and only referred so far to literature references. This chapter has the aim to fill such a gap and give a brief description of the materials used in my works. I remind that the growth methods and samples preparation have been previously introduced.

5.1 2D-systems

5.1.1 Graphene

Graphene is a monolayer of C atoms arranged in a honeycomb lattice [53]. It is probably one of the most famous materials of the last century, the one which certainly stimulated an unprecedented interest in 2D materials and for which Geim and Novoselov won the Nobel prize for physics in 2010.

The huge interest for this system is not by chance. Graphene hosts nearly unique mechanical and electronic properties, such as room temperature quantum Hall effect [54], a giant carrier mobility of $10^6 \text{ cm}^2/\text{Vs}$ [55] which exceeds by more than two orders of magnitude that one of Si and it is an inert material [56]. The interesting aforementioned electronic properties of graphene originate from its peculiar electronic structure with two linearly dispersing

bands touching in a single charge neutrality point called Dirac-point [53].

Whilst a large variety of experimental and theoretical works have been carried out on graphene and graphene-like materials, its properties are so surprising that a large portion of them has still to be investigated. In particular, details of many-body interactions and the role of electron-phonon coupling away from energies close to the Fermi level are still not fully addressed. This gives me the intriguing possibility to fill this missing piece of information and directly explore this material to contribute to the gain of the general understanding of its properties.

5.1.2 δ -layers

One of the major achievements since the eighties in the semiconductor industry is the possibility to dope semiconductors with nearly atomic precision. When the high-density doping profile approaches the micrometer-scale limit, the doped system is called δ -layer, alluding to the δ -function shape that a very narrow profile would assume into the semiconducting bulk. In principle, δ -doping can be either carried out onto the surface of a material or within a bulk system. In both cases, the idea is to incorporate into the system either donor or acceptor species to modify and control the electronic properties of the system.

Donor species, such as phosphorus for example, give electrons to the system (n-doping) while acceptor species, such as boron, receive electrons (p-doping). Doping a material can be thought as an alternative route to apply to the material an electric field. As a consequence of such an electric field the electronic bands of the system will be modified. Adding electrons will fill empty states and the Fermi level will be shifted towards lower values of binding energy. Conversely, removing electrons from the system will empty states, and this will cause a Fermi level shift towards higher binding energy values. This is represented in Fig. 5.1.

Nowadays, δ -doping can be realized on silicon to create an hybrid material with metallic properties, also called silicon-phosphorous δ -layer (Si:P δ -layer). To realize this system, a clean silicon surface is prepared through series of direct heating flashes up to $\approx 1200^\circ\text{C}$. Once the Si has been cleaned, i.e. XPS does not show any sign of contaminants but the only visible peaks

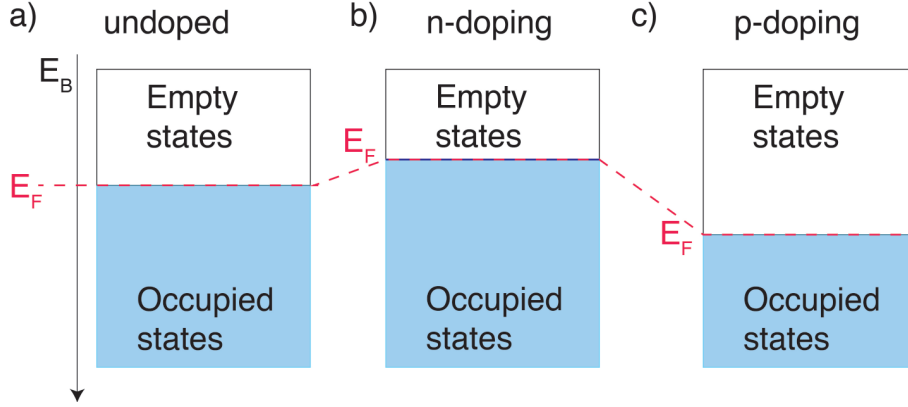


Figure 5.1: **Doping a system.** a) Undoped system: the electrons fill the states up to the Fermi level. The occupied density of states is represented by the blue area, the unoccupied by the white. b) Effect of n-doping to the system: adding electrons will increase the number of occupied states, therefore E_F will shift towards lower E_B . c) Conversely, p-doping will remove electrons and E_F will shift down.

belong to Si, phosphine gas is dosed and it will stick onto the surface. P is substitutionally incorporated into the Si lattice by annealing the system at 350°C for one minute, resulting in a self-saturating P coverage of $1/4$ of a monolayer. Finally, nm-scale ($\approx 2 - 6$ nm) epitaxial Si is deposited onto the system to activate the doping field. This is the standard procedure I used for the fabrication of Si:P δ -layers in the works presented here. Variants of this recipe can be realized by varying the amount of P concentration or depositing P simultaneously with Si; in particular, we performed all slightly different growths from the standard one presented and the details are all well described in each work. A schematic for this material is illustrated in Fig. 5.2a.

In Si:P δ -layers, because of the exceptionally high density dopant profile, the n-doping electric field will be so strong (more than 0.5 eV) that the orbital nature of the system will be dramatically affected. Such an orbital change will drive electronic confinement giving rise to metallic nearly 2D states dispersing across the Fermi level (see Fig. 5.2b-c).

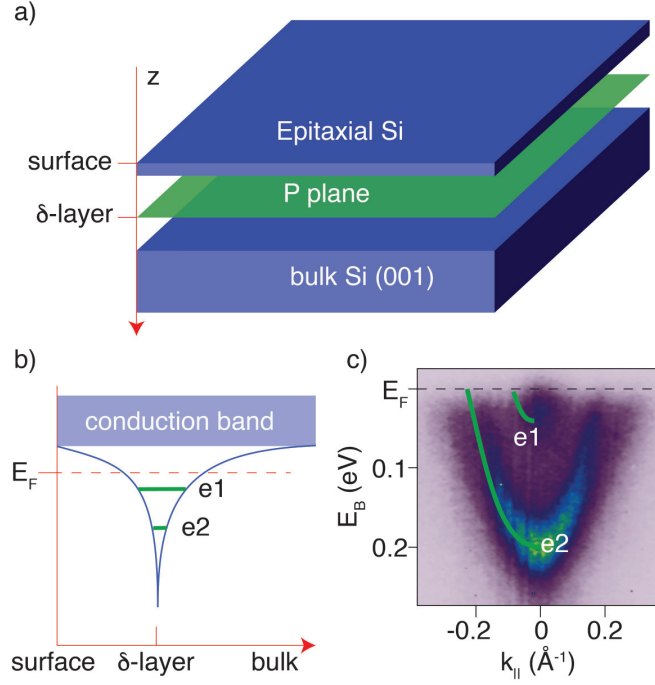


Figure 5.2: **Si:P δ -layer.** a) A schematic of a Si:P δ -layer. b) The phosphorous doping induces a strong band bending nearby the region where the P is placed creating a quantum well. The Si conduction band electrons will be quantized, forming discrete energy states dispersing across the Fermi level. c) ARPES spectra of Si:P δ -layer band structure at the Fermi level.

In paper 6, I also carried measurements on boron δ -doped diamond. These samples, conversely to silicon, have been doped at the surface. In this case, the boron induces an ‘upward’ band bending, realizing a strong p-doping around the boron location. Through systematic ARPES measurements we found that by reducing the thickness of the boron-doped region, electron-electron correlations are responsible for a strong band renormalization even though the general properties of the bulk-like systems are preserved. Details about this system in paper 6 and in ref. [57].

5.2 Layered compounds: transition metal dichalcogenides (TMDs)

Transition metal dichalcogenides (TMDs) are a class of layered materials exhibiting unusual and exotic electronic properties, such as unconventional superconductivity [58], charge density wave transitions [58, 59] and spin polarization of the electronic bands locked to valley and momentum degrees of freedom [8].

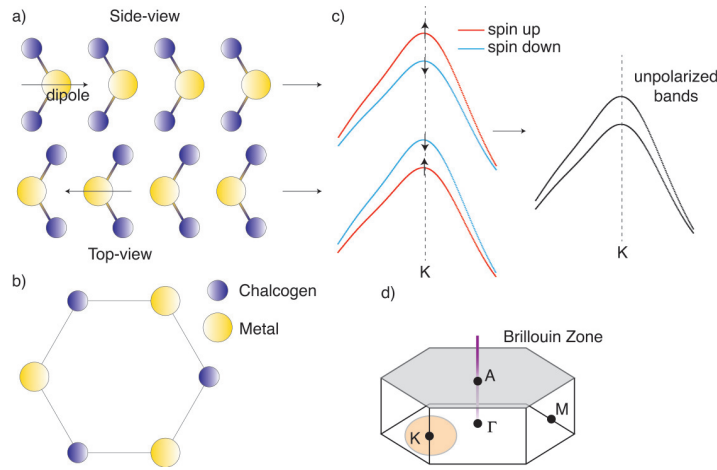


Figure 5.3: **Transition metal dichalcogenides.** a) Schematic of TMDs' crystal structure showing how in each layer an electric dipole is formed. The two closest layers have opposite electric dipole, hence their effect in the unit cell seen as a total is zero. b) Top-view of TMDs. The lattice develops in a honeycomb fashion with alternating sites. c) Band structure of the TMDs band structure around the BZ point K (obtained from tight-binding, which will be treated later in this thesis). The unit cell of the system is supposed to give spin-unpolarized bands. d) BZ of TMDs.

These materials attracted a giant interest over the last few years, offering a powerful alternative route to graphene for tailoring unusual properties in low dimensions. TMDs are present in various phases and compositions and each system constitutes a nearly-unique bed-test for experiments. Here, I will only limit my attention to the 2H-type TMDs, with centrosymmetric bulk samples' structure, such as 2H-WSe₂. From now on, when I will talk of

TMDs I will only refer to the 2H phase.

The crystal structure of TMDs can be seen in Fig. 5.3a-b: it consists of two monolayers stacked together staggered in an ‘AB’ configuration. From the top-view, as in Fig. 5.3b, the system develops in a graphene-like fashion with metal and chalcogen atoms placed at two consecutive inequivalent sites. The unit cell of the system, which is composed of two layers, preserves inversion symmetry. The combination of inversion symmetry ($E(\uparrow, \vec{k}) = E(\uparrow, -\vec{k})$) and time reversal symmetry ($E(\uparrow, \vec{k}) = E(\downarrow, -\vec{k})$) forbids any lifting of the spin and energy degeneracy for the electronic bands. Each layer is non centrosymmetric, hence alone it would potentially have a spin polarization for its bands, as indicated in Fig. 5.3c for bands around the K point. However, the spin polarization is opposite in sign and equal in magnitude in each layer, thus the two-layers unit cell has unpolarized bands.

In our works (paper 7 [8]) we show how, even though the electronic structure of systems such as bulk WSe₂ is expected to be unpolarized, the system still show a net spin polarization which can be resolved by spin-ARPES. We attribute this to the local breaking of inversion symmetry in each layer constituting the unit cell combined with the extreme surface sensitivity of spin-ARPES. The details about the implications that this property can lead to, can be found in paper 7 [8].

5.3 Cr-doped ZnS

Cr-doped ZnS is a semiconductor with a wide energy gap ($\approx 3.6 - 3.9$ eV) where due to the Cr impurities, electronic states can be created within such a gap. Such electronic states are generally called *intermediate bands* (IBs). This material is considered to be a promising candidate for high-efficiency solar cells, indeed the presence of extra states within the bandgap allows multiple electronic transitions to take place: (i) electrons can be promoted from the valence into the conduction band, as in ordinary Si-based solar cells, (ii) electrons excited by a lower wavelength can be first promoted into the intermediate bands, then from such an IB into the conduction band. IB creates additional channels to generate electron-hole pairs, therefore additional current making this material suitable for photovoltaics.

For paper 11 ([51]), where we discuss how we can access information about the nature of an intermediate band in Cr-doped ZnS by using RPES.

5.4 5-Fluorouracil, 5-Fu

5-Fu is one of the most used drug in the treatment of cancer. It is a molecule constituted by four C, two N, two O, one F and three H, as illustrated already in Fig. 4.4. It is a thymidine inhibitor: thymidine is a nucleoside necessary for DNA to reproduce. If thymidine is damaged by the effect of 5-Fu, the cancer cells cannot reproduce, limiting the spread of the tumor in the human body and ultimately annihilating its effect.

In paper 12 we show the surface reaction between 5-Fu and Ag, a study motivated by the fact that Ag is a common coating material for catheters used for the chemotherapy drugs' delivery. In order to prepare the system 5-Fu/Ag(111), the silver surface undergoes cycles of sputtering and annealing up to the point where no contaminants are seen in the XPS spectra. Then, 5-Fu in powder form is evaporated by indirect heating through a crucible directed towards the Ag(111). By using XPS, as reported in paper 12 [50], we demonstrated that this method is a good strategy to evaporate the molecules intact without altering their compositions.

5.5 A self-assembled organic monolayer, porphyrin

Porphyrins are a group of heterocyclic macrocycle organic compounds, i.e. big organic complicated molecules composed of aromatic C rings, N, O and H present in different amount. Whilst the details of these molecules can be found in Ref. [62], the only thing we need to know for understanding paper 5 of this thesis [63] is the possibility for such molecules to self-assemble in a monolayer forming a periodic array of quantum dots when evaporated onto the top of a certain surface, in this case Ag(111). This can be regarded to as a superstructure made of quantum-wells connected to each other. Such an array of quantum-wells manifests in ARPES as a nearly-free electron like state dispersing at an energy just above the Fermi level ([63]).

The molecule is evaporated by indirect heating from their powder form. Details about the molecule's structure can be found in paper 5. My main contribution to this paper has been to demonstrate and study the nature of the electronic state originating from the molecular quantum confinement by using ARPES. I here anticipate that such a state disperses at energies slightly above the Fermi level, we carried the ARPES measurement at 300 K, exploiting the broadening of the Fermi-Dirac cutoff for accessing part of the unoccupied states. Importantly, similarly to 5-Fu (previously introduced), porphyrin is an organic molecule, thus in order to carry photoemission measurements without the risk of beam-damage we had to use a low beam-flux and monitor any possible molecular degradation within the time of a single measurement. In order to do this, we detuned the beamline undulator and used a big spot size. Generally, the bigger the spot-size is, the lower the momentum resolution will be; in this case, we could compensate for this effect using relatively low photon energies.

5.6 Curved samples, the Bi case

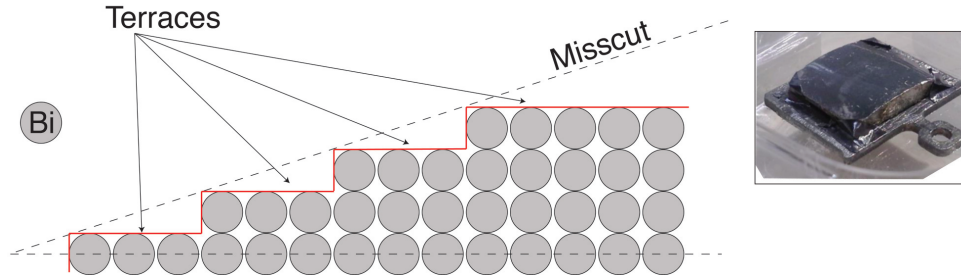


Figure 5.4: **Curved Bi sample.** Schematics of a curved Bi sample. The surface runs over multiple vicinal surfaces of the Bi(111). The sample has been polished such that multiple atomically precise step terraces can form.

Recently, it has been shown that even topologically trivial states of matter, such as Bi exhibit interesting topological-insulator properties when the dimensionality of the system is reduced. In order to investigate these topological-

insulator states, Bi(111) vicinal surfaces must be investigated.

For achieving this purpose, a Bi crystal has been electro-polished such that its surface exhibits a curved shape with multiple vicinal surfaces around the Bi(111) covering a smooth 22° angular range, as in Fig. 5.4.

Chapter 6

Analysis and Modeling

This section is dedicated to the description of the analytical methods which have been used for the analysis of the results presented in this Thesis.

6.1 Data Fitting

Data fitting is one of the most powerful approaches to get information from photoemission spectra. Whether we want to extract useful features from XPS or from ARPES spectra, the idea behind this procedure is the same: photoemission spectra have a certain lineshape which can be modified by electronic interactions (for example by many body effects) and that must be convoluted by the resolutions of the instrument. Moreover, we know that such a lineshape can be described by particular functions (Lorentzian is generally a good choice for a non interacting electronic system as already introduced by equation 3.9). By using those functions and varying their parameters we can create a model which ‘fits’ our experimental results and that consequently gives quantitative information about the spectra.

As an example let us consider the ARPES spectra collected for bulk WSe₂ of Fig. 6.1a. This data set represents the strong Zeeman-split of the material’s valence band around the BZ high symmetry point K (along the direction $\Gamma'-K-\Gamma$). We want, for example, to accurately and quantitatively estimate the extent of such a Zeeman split in energy. One way to do this is to ‘track’ the valence band structure ‘point by point’. This can be done by extracting from the ARPES spectra intensity profiles either as function

of energy or as function of momentum and then by fitting such curves with a proper fit-function. The distribution curves are called energy-distribution-curves (EDC) and momentum-distribution-curves (MDC), whether they are function of energy or momentum respectively. One EDC extracted from the data of Fig. 6.1a at $k_{||} = 0$ is shown in Fig. 6.1b.

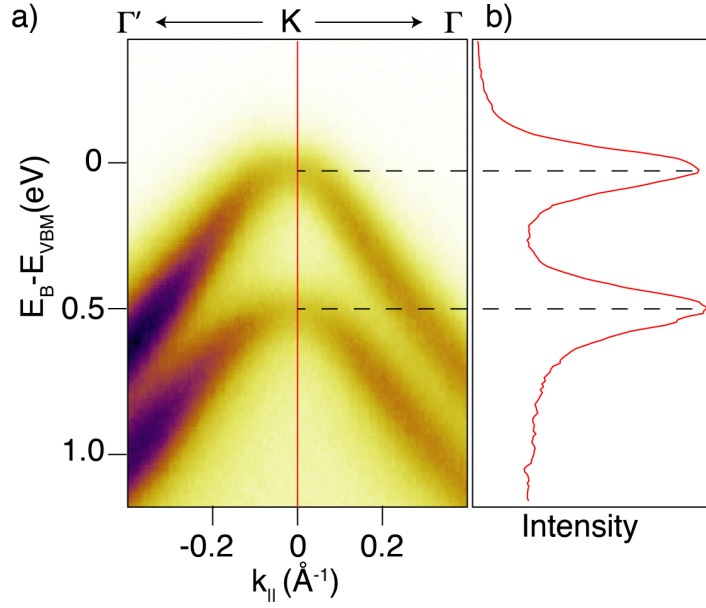


Figure 6.1: **EDC example.**a) ARPES measurement of WSe₂ valence band structure around the K point showing the Zeeman-like spin splitting which characterizes this material. The energy scale is represented relative to the valence band maximum energy (E_{VBM}). b) EDC extracted from the data for a value of momentum $k_{||} \approx 0$

Such an EDC shows two clear peaks, corresponding to the spin-split valence band of this material around K . Such an EDC carries also a background which must be correctly removed before the fit can be performed. In this case, I removed from the data a Shirley background [66]. The data without their background are illustrated in Fig. 6.2a.

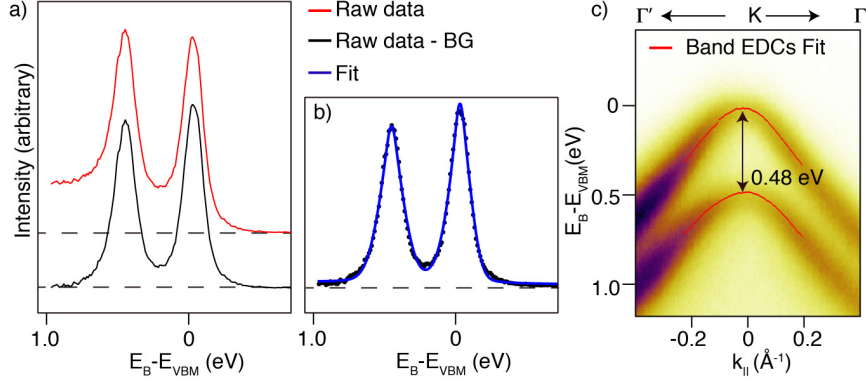


Figure 6.2: **Band fitting.** a) Raw data (red) and raw data after a Shirley background removal (black). b) After background subtraction the data have been fitted by Lorentzian curves convoluted with a Gaussian to account for the experimental energy and momentum resolutions. c) The ARPES bands are fitted column by column (EDC by EDC) to obtain a quantitative information about the valence band location.

After background removal, the data can be fitted with a function representing the spectral lineshape. For example, a good model can be built using Lorentzian functions (with a variable degree of asymmetry included) convoluted with a Gaussian which accounts for the resolution of the instrument. This leads to the results shown in Fig. 6.2b. From the fit results we can understand parameters such as peaks locations and widths.

If we now do this procedure for all the ARPES data points, we are able to fit the whole ARPES spectra and to ‘track’ its electronic dispersion, as in Fig. 6.2c. Quantitative information from the ARPES spectra, such as the spin-splitting which is found to be (0.48 ± 0.03) eV, can be found.

6.1.1 2D-fit and many body interactions

Specifically for ARPES, when the non-interacting electronic structure (we will call the non-interacting band the *bare band*) is known by calculations such as tight-binding (which will be dealt within the next section), it is

possible to obtain information about many body interactions in the solid from the spectra by using a ‘2D-fit’. When I talked previously about many body interactions, I introduced a simple way to simulate ARPES spectra with inclusion of electron-phonon coupling, electron-electron interaction and electron-impurity scattering. The same model can be used for fitting ARPES data: once the lineshape of the bare band is known we can dress it with interactions and then compare it to the real data. The real data must have undergone a proper background subtraction.

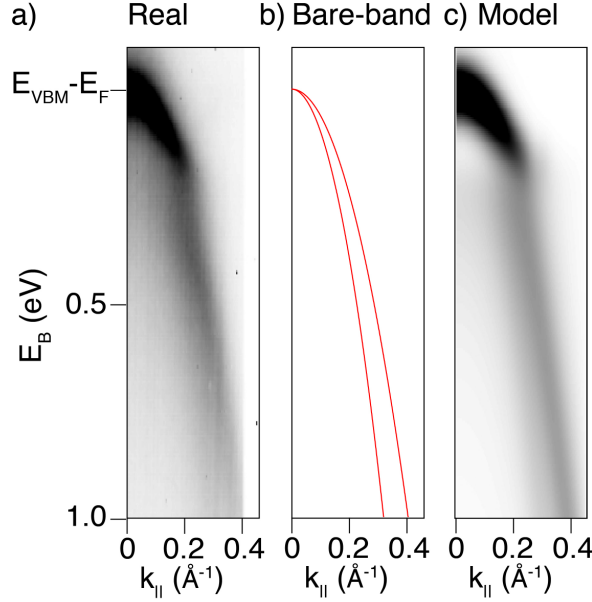


Figure 6.3: **Example of 2D fit on Graphene’s σ -band.** a) Raw ARPES data showing the electronic structure of graphene’s σ -band near the top of the valence band. b) Bare band of graphene’s σ -band composed of two parabolas. c) Model obtained by the 2D fit which shows a good agreement with the ARPES measurement and the strong kink caused by electron phonon coupling.

The main idea to perform this fit is to vary one or more parameters at the time and compare the model obtained to the raw ARPES data. The model whose difference with the real measurement is the smallest gives the

best simulation. Therefore, the best fit contains the many-body physics parameters which have been used to give the best description of the spectra.

In paper 8 [35] and 1 [36] we used this method to describe the many-body interactions in graphene and in Si:P δ -layers respectively. In Fig. 6.3 we show how the 2D-fit can be applied to ARPES spectra. In Fig. 6.3a an ARPES measurement of the graphene's σ -band around its maximum is shown. The theoretical bare-band is well described by two parabolas (Fig. 6.3b) but as visible from the data, there is a strong 'kink' at ≈ 200 meV below the band maximum. Such kinks are a typical signature of electron-phonon coupling and are generally observed at the Fermi level. In Ref. [35] we argue how it is possible to observe such a kink also close to the σ -band maximum (≈ 3.5 eV below E_F), far away from energies close to E_F . This is possible because the presence of the σ -band is responsible for a sudden increase of the electron DOS, thus mimicking the behavior of a Fermi-cutoff but at energies far below E_F . Thus, the physics happening at E_F and related to the Fermi-cutoff must also occur close to the top of the σ -band. We used the 2D fit to quantify the strength of the electron phonon coupling in terms of the parameter λ (previously introduced) and we found an unusually big value $\lambda \approx 0.75$, comparable in strength to the electron-phonon coupling found for BCS superconductors. In Fig. 6.3c we show the best fit results (the resolutions of the instrument have been included) which demonstrate an excellent agreement with the ARPES measurement. This method is quite general and once the bare band of a material is known can be applied to extract information about the interactions in the solid.

6.2 Tight-binding

A useful method to describe the electronic band structure of solids is the *tight-binding* approximation. This approach consists in approximating the electronic structure of a material with the superposition of its atomic wavefunctions, i.e. the wavefunctions which describe the electronic properties of each atom of the lattice. Whereas this approach is a one-electron model, it offers a good pathway to describe relativistic effects such as spin-orbit coupling and it gives a good description of surface states and lattice reconstructions.

The idea behind this method is to consider the atomic wavefunctions

mostly localized within each atom, therefore the atomic wavefunction will be similar to the atomic orbital of the free atom. Even though an ideal phenomenological description of the electronic bands in a solid would be provided by a rather complicated Hamiltonian, the tight binding approximation gives already a good description of the physics of the electronic structure considering only the so called *bond energies*, the energies by which atoms in the lattice interacts by means of their orbitals overlap.

Let us make a generic example of the tight binding approximation. Let us consider a wavefunction $\phi_m(r)$ which describes the atomic orbital of an atom m . Such a wavefunction is the eigenstate of the atomic Hamiltonian H_{at} . When the lattice is formed by adjacent atomic sites, the single wavefunctions will overlap. If the electrons are tightly bounded to the atoms (from which the name tight-binding derives) the overlap is not strong. In this situation, the Hamiltonian of the whole system is:

$$H(r) = \sum_{R_n} H_{at}(r - R_n) + H_1 \quad (6.1)$$

where H_1 includes correcting factors which account for more complicated interactions and interactions. A wavefunction which is solution to the Schrödinger equation, dominated by the Hamiltonian in equation 6.1, can be found as a linear combination of the single atomic wavefunctions:

$$\psi(r) = \sum_{m, R_m} a_m(r) \phi_m(r) \quad (6.2)$$

By solving the Schrödinger equation and figuring out the system eigenvalues it is possible to reconstruct the electronic band structure of a certain system. For example, let us solve a tight binding model for the π -band of graphene. In paper 10, I used the tight binding approximation for calculating also the σ -band of this system, but for the sake of the understanding the π -band is already a good example.

6.2.1 π -band of graphene, a simple tight-binding approach

First of all let us define the graphene's lattice \vec{a}_1 and \vec{a}_2 and the lattice vectors and let us assume $a = 1.42 \text{ \AA}$ to be the distance separating two C atoms.

This is represented in Fig. 6.4.

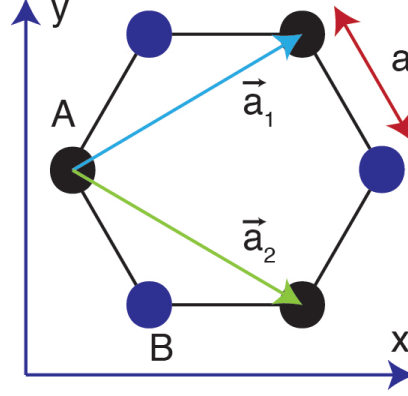


Figure 6.4: **Defining graphene's lattice vectors.** The atomic lattice of graphene is composed of two inequivalent C atoms, called 'A' and 'B' and indicated by the color black and blue respectively. Adjacent C atoms are separated by a and the lattice vectors of the unit cell are defined as \vec{a}_1 and \vec{a}_2 .

In the coordinate system defined in Fig. 6.4 developing the xy -plane, the lattice vectors can be expressed as:

$$\vec{a}_{1,2} = \left(\frac{\sqrt{3}}{2} a_{LC}, \pm \frac{a_{LC}}{2} \right) \quad (6.3)$$

where $a_{LC} = \sqrt{\vec{a}_1^2 + \vec{a}_2^2} = 2.46 \text{ \AA}$ is the lattice constant of graphene. Our task is to calculate the π -band of this system. Such a band originates from the orbitals p_z of the carbon system, therefore, for this purpose I will consider only these orbitals without allowing any possibility for overlapping with orbitals different from the p_z . In addition, to further simplifying the problem, I can consider only interactions with the first neighboring atoms. In this way the electronic structure of the π -band of graphene will be given only by the overlap and interactions between the p_z orbitals of an 'A' atom and three nearest neighbors 'B' atoms located at distances $\vec{R}_1 = (-a, 0)$, $\vec{R}_2 = (\frac{a}{2}, \frac{\sqrt{3}}{2}a)$ and $\vec{R}_3 = (\frac{a}{2}, -\frac{\sqrt{3}}{2}a)$.

Since two inequivalent atoms of only one orbital type contribute to this approximation, we will expect only two solutions, i.e. two eigenstates. The

next step is to build the transfer Hamiltonian H and the overlap Hamiltonian S . H contains all the terms which describe the interactions of electrons from one site to another one, S describes the overlap between atomic orbitals. Then, the problem is solved by finding solutions to the secular equation:

$$|H - E(k)S| = 0 \quad (6.4)$$

$E(k)$ defines the system's band structure. The Hamiltonian H for the atoms 'A' and 'B' can be found as:

$$H = \begin{matrix} & A - p_z & B - p_z \\ \begin{matrix} A - p_z \\ B - p_z \end{matrix} & \begin{pmatrix} H_{AA} & H_{AB} \\ H_{BA} & H_{BB} \end{pmatrix} \end{matrix} \quad (6.5)$$

with matrix elements $H_{BB} = H_{AA}$ and $H_{BA} = H_{AB}^*$, where:

$$H_{AA} = \langle \phi_{pz}^A | H | \phi_{pz}^A \rangle = E_{pz} \langle \phi_{pz}^A | \phi_{pz}^A \rangle = E_{pz} \quad (6.6)$$

with E_{pz} energy of the interaction of an atomic wavefunction with itself; and:

$$H_{AB} = \langle \phi_{pz}^A | H | \phi_{pz}^B \rangle = t_{AB} \sum_{R_i} e^{i\vec{k}\vec{R}_i} \quad (6.7)$$

with $\vec{k} = (k_x, k_y)$ and $i = 1, 2, 3$ and t_{AB} describing the interaction between atoms 'A' and 'B'. Thus, the matrix H takes the new form:

$$H = \begin{matrix} & A - p_z & B - p_z \\ \begin{matrix} A - p_z \\ B - p_z \end{matrix} & \begin{pmatrix} E_{pz} & t_{AB} \sum_{R_i} e^{i\vec{k}\vec{R}_i} \\ t_{AB} \sum_{R_i} e^{-i\vec{k}\vec{R}_i} & E_{pz} \end{pmatrix} \end{matrix} \quad (6.8)$$

Similarly, we can find a form for S as:

$$S = \begin{matrix} & A - p_z & B - p_z \\ \begin{matrix} A - p_z \\ B - p_z \end{matrix} & \begin{pmatrix} 1 & s_{AB} \sum_{R_i} e^{i\vec{k}\vec{R}_i} \\ s_{AB} \sum_{R_i} e^{-i\vec{k}\vec{R}_i} & 1 \end{pmatrix} \end{matrix} \quad (6.9)$$

By using these matrices the equation 6.4 can be solved and $E(k)$ also described, giving the electronic structure of graphene's π -band as in Fig. 6.5. As a remark, the integrals E_{pz} , t_{AB} and s_{AB} can be evaluated by using other

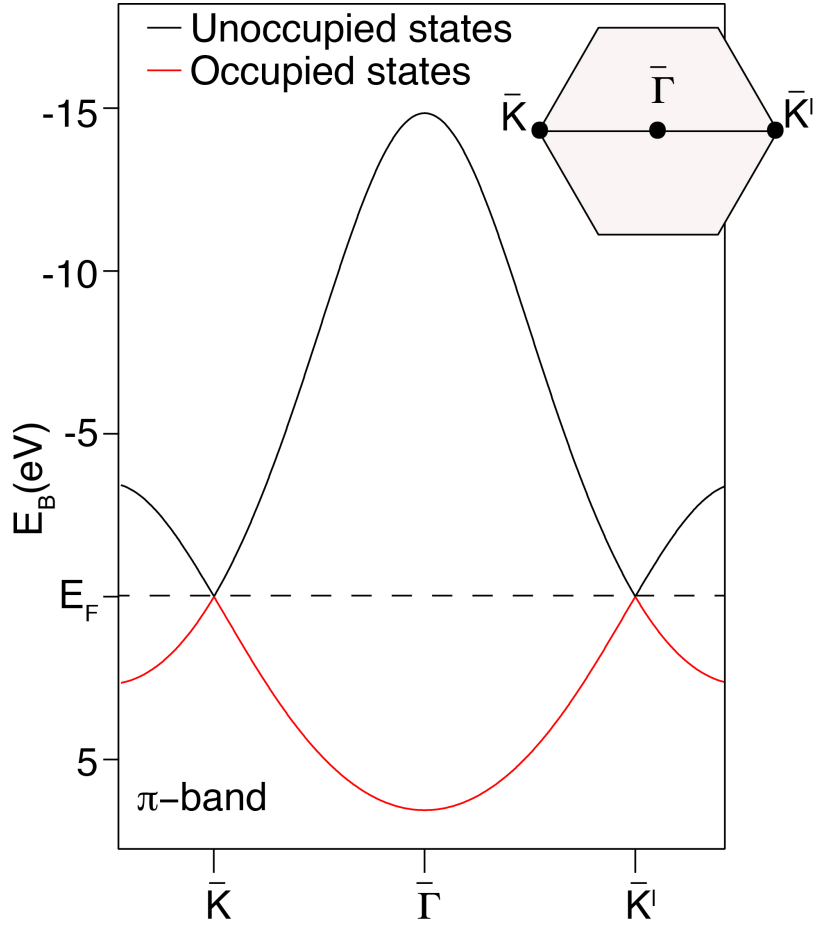


Figure 6.5: **Numerical tight binding for the π -band of graphene.** The π -band of graphene has been obtained by using the tight binding calculation extended to the first nearest neighbors. It is shown only along the K - Γ - K' direction of the BZ as illustrated in the inset.

numerical approaches such as density functional theory calculation and, for graphene, found in several literature works [67]. The real power of tight-binding is its simplicity and at the same time a rather good description of complicated physics.

Chapter 7

Papers included in the Thesis

“Disentangling phonon and impurity interactions in δ -doped Si(001)”

Appl. Phys. Lett. 104, 173108 (2014)



Disentangling phonon and impurity interactions in δ -doped Si(001)

Federico Mazzola,¹ Craig M. Polley,^{2,3} Jill A. Miwa,⁴ Michelle Y. Simmons,³ and Justin W. Wells^{1,a)}

¹Department of Physics, Norwegian University of Science and Technology (NTNU), N-7491 Trondheim, Norway

²MAX IV Laboratory, Lund University, 221 00 Lund, Sweden

³School of Physics, Centre of Excellence for Quantum Computation and Communication Technology, University of New South Wales, Sydney, NSW 2052, Australia

⁴Department of Physics and Astronomy, Interdisciplinary Nanoscience Center (iNANO), University of Aarhus, 8000 Aarhus C, Denmark

(Received 14 February 2014; accepted 22 April 2014; published online 2 May 2014)

We present a study of the phonon and impurity interactions in a shallow two dimensional electron gas formed in Si(001). A highly conductive ultra-narrow n -type dopant δ -layer, which serves as a platform for quantum computation architecture, is formed and studied by angle resolved photoemission spectroscopy (ARPES) and temperature dependent nanoscale 4-point probe (4PP). The bandstructure of the δ -layer state is both measured and simulated. At 100 K, good agreement is only achieved by including interactions; electron-impurity scattering ($W_0 = 56$ to 61 meV); and electron-phonon coupling ($\lambda = 0.14 \pm 0.04$). These results are shown to be consistent with temperature dependent 4PP resistance measurements which indicate that at 100 K, $\approx 7/8$ of the measured resistance is due to impurity scattering with the remaining $1/8$ coming from phonon interactions. In both resistance and bandstructure measurements, the impurity contribution exhibits a variability of $\approx 9\%$ for nominally identical samples. The combination of ARPES and 4PP affords a thorough insight into the relevant contributions to electrical resistance in reduced dimensionality electronic platforms. © 2014 AIP Publishing LLC. [<http://dx.doi.org/10.1063/1.4874651>]

Intense efforts are continuously being made to reduce the physical dimensions of electronic devices and components with few nanometer length scales becoming commonplace.^{1–3} The current state-of-the-art of this miniaturisation is the realisation of few-atom wide conductive wires^{4,5} and few dopant devices,⁶ with a single dopant transistor recently being demonstrated.⁷ In these examples, the underlying platform is δ -doped Si(001)—silicon in which an ultra dense and narrow two dimensional (2D) plane of phosphorous dopants exists beneath the surface, forming a highly conductive sheet.^{8,9} Due to the buried location of the 2D layer, direct measurements of the bandstructure have been challenging and have only recently been performed.^{10,11} Instead, a reliance on the abundant spectrum of calculational approaches^{6,12–17} has dominated the understanding of the electronic properties of δ -doped Si(001). With few exceptions,¹⁸ calculations have neglected interactions such as electron-phonon coupling, and thus a non-interacting bandstructure is commonly presented. This is unfortunate, since phonon interactions influence physical properties,¹⁹ including conductance, for which δ -layers are prized.

In this Letter, we quantitatively address the interactions which contribute to the electrical resistance and discuss the implications for lifetimes (which are important for δ -layer derived devices). We combine of 4-point probe (4PP) measurements and the highest quality angle resolved photoemission spectroscopy (ARPES) data available with ARPES simulations.

The 4PP resistance, R_{4PP} , (proportional to the sample's resistivity²⁰) was measured using an Omicron Nanoprobe.⁸

^{a)}quantum.wells@gmail.com

Samples were prepared *in situ* using standard methods;^{21,22} a clean Si(001) surface was prepared by annealing ($>1200^\circ\text{C}$) in ultra high vacuum ($\approx 2 \times 10^{-10}$ millibars), a saturation coverage ($\approx 1/4$ monolayer) of P dopants was formed by exposure to phosphine gas (5 min at 5×10^{-9} millibars), incorporated into the Si(001) surface by annealing at 350°C and encapsulated under 4 nm of epitaxial silicon (grown by thermal evaporation). Variable spacing measurements reveal the dimensionality of the conductance^{23,24} and confirm 2D behaviour.⁸ The measurements presented here were performed using a co-linear arrangement of the four probes with a spacing of $100\ \mu\text{m}$.

Typically R_{4PP} is $\approx 125\ \Omega$ at 50 K, increasing to $175\ \Omega$ at 310 K. For a particular sample, the uncertainty is $\approx 2\%$ (at 310 K). Contrary to semiconducting systems where increasing carrier density dominates the temperature dependence of the resistance, the δ -layer state is metallic and the thermal promotion of carriers in this temperature range is not significant.^{25,26} Instead, the resistance is seen to increase with increasing temperature, consistent with increased electron-phonon coupling (EPC), as previously described for other 2D metals.^{20,27}

A typical dataset is shown in Fig. 1(a) atop a schematic representation of the electron-electron scattering (EES, region I), EPC (region II), and electron-impurity scattering (EIS, region III) contributions. EES is only important at significantly lower temperatures²⁸ and is not relevant here, and EIS and EPC contributions to the resistance can be separated by their temperature dependence;²⁰ EIS is typically constant²⁹ (R_0) and EPC has a distinctive temperature dependence of the form αT^γ . Thus, the data can be well described by $R = R_0 + \alpha T^\gamma$, where R_0 is found to be $120\ \Omega$ and γ is found

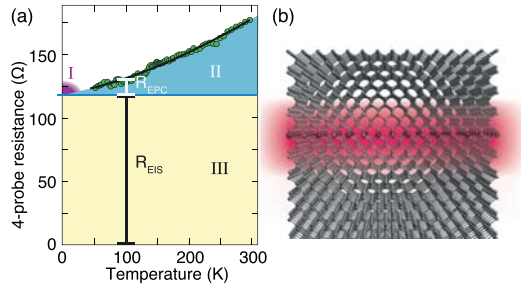


FIG. 1. (a) Temperature dependent 4-probe resistance of δ -doped Si(001) (green circles) with a modelled $T^{1.5}$ dependence overlaid (black line). The regions I (purple), II (blue), and III (yellow) show schematically the contributions of EES, EPC, and EIS to the resistance, respectively. At 100 K, black and white bars indicate the assumed EIS and EPC contributions to the resistance, respectively. (b) Idealised schematic of δ -Si(001), with the P dopants shown as larger black spheres and the approximate distribution of the carriers indicated by red shading.

to be 1.5, as expected.²⁵ Thus, for a given temperature, for example, $T = 100$ K (as depicted in Fig. 1(a)), the measured resistance can be described as $R_{4pp} = R_{EES} + R_{EPC} + R_{EIS}$, where $R_{4pp} \approx 135 \Omega$, $R_{EES} \approx 0 \Omega$, $R_{EPC} \approx 15 \Omega$, and $R_{EIS} \approx 120 \Omega$ (see Fig. 1(a)). In other words, at 100 K, EIS is by far the largest contribution.

It is important to consider which region of the δ -doped system is relevant for charge transport; even in the ideal case where the dopants are located in an atomically sharp plane, the donated electrons are not confined within this atomic plane (see schematic in Fig. 1(b), or for a more precise depiction, Ref. 14). Calculations¹² indicate that the carrier distribution is well described as Lorentzian, with a full width half maximum of 0.6 nm, i.e., 80% of the carriers reside within ± 1.0 nm of the δ -layer. Thus, although the phonon modes and impurity/defect density are likely to be modified in the atomic plane of the dopants, the charge conduction takes place mostly in the neighbouring silicon.

ARPES measurements facilitate a further insight into the interacting bandstructure. Samples were prepared *in situ* at beamline I4 of the synchrotron light source “MAX-III”. ARPES measurements of buried states are notoriously challenging,^{10,30} thus to maximise the data quality, a thinner encapsulation (1 nm) and a 500 °C post-anneal were necessary. The Si2p and P2p core levels were monitored throughout, indicating negligible segregation and diffusion of the dopants. The energy and momentum resolutions have been confirmed to be better than 40 meV and 0.01 \AA^{-1} , respectively.^{31,32}

Unlike the available calculations, ARPES reveals the bandstructure with interactions intrinsically included. More specifically, ARPES can be thought as a direct measure of the spectral-function $\mathcal{A}(\omega, k)$, containing the non-interacting band dispersion, $\epsilon(k)$, and the real and imaginary parts of a self energy (Σ' and Σ'' , respectively), which describe the relevant interactions.³³ Σ' and Σ'' are manifested in measurements as renormalization of the band dispersion and an increased linewidth, respectively.

ARPES data, collected for two nominally identical samples, “Sample I” and “Sample II,” are displayed in Figs. 2(a) and 2(b), respectively. In both cases, only the 1Γ band is

occupied. The experimental valley splitting of ≈ 200 meV is large compared to calculated values,¹¹ thus the next band (so-called 2Γ) has its minima very close to the Fermi level and is barely visible. From the occupancy 1Γ , the carrier density is estimated as $n_s \approx 2.4 \times 10^{13} \text{ e/cm}^2$ (i.e., above the metal-insulator transition³⁴).

Calculating $\epsilon(k)$ has been the centre of an intense effort, thus, the full bandstructure (for a wide variety of doping scenarios) has been reported extensively.^{6,11–17} The 1Γ band minimum is well approximated as parabolic, with an effective mass of $\approx 0.2 m_e$ —the same as the bulk conduction band minimum from which it is derived.^{6,11,15} The calculated non-interacting 1Γ band is reproduced in Fig. 2(c) and is largely consistent with the measured bandstructure, except for the linewidth. After including the experimental energy and momentum resolutions (Fig. 2(d)), the band is broader but is still much sharper than the ARPES measurement. After including interactions (Figs. 2(e)–2(g)), a much more realistic representation of the bandstructure is achieved.

Developing a simulation is straightforward since $\epsilon(k)$ has been calculated,¹¹ and a realistic Σ (which depends on the nature of the interaction) can be built. Thus, a modelled spectral function $\mathcal{A}(\omega, k)$ is constructed, convolved with the experimental resolutions, and directly compared to the ARPES data.³⁵ For the case of EIS, $\Sigma' = 0$ and $\Sigma'' = W_0$, where W_0 is a constant value describing for the impurity contribution to the self energy.^{36,37} The root mean square (rms) difference between the measured and simulated dispersions normalised to the average intensity (so-called Δ) is calculated and used to judge the agreement. For a realistic range of trial values of W_0 , Δ exhibits a minima, which allows us to estimate $W_0 = 70 \pm 12$ meV for Sample I and 65 ± 8 meV for Sample II (the uncertainty is evaluated from the 95% confidence interval). Fig. 2(e) shows good agreement, confirmed by the small rms difference; $\Delta = 1.14\%$ (for Sample I). The magnitude of W_0 indicates that electron-impurity scattering is particularly small (c.f. high quality graphene³⁸).

An alternative approach is to model the interaction as being purely phononic, in which case Σ'' is no longer constant since phonon interactions dramatically increase for electron binding energies which are larger than the phonon energy.²⁰ Thus, at the phonon energy below the Fermi level, the lifetime, which is closely related to Σ'' , will increase dramatically, and, equivalently the effective mass of the interacting electron will increase by a factor $(1 + \lambda)$ causing a renormalisation of the band dispersion, described by Σ' (and related to Σ'' by a Kramers Kronig transform), to occur.

Such a model is straightforward to construct^{37,39} (see Fig. 2(f)), and has routinely been applied to a range of materials.^{36,40,41} Although multiple phonon modes may be present, the optical phonon is particular noticeable since it allows the transfer of a significant amount of energy (60 meV (Ref. 42)) and any amount of momentum. Thus, a satisfactory simplified model can be constructed, based on the Debye approximation,³⁹ in which Σ' exhibits a peak at 60 meV. Evaluating Δ for a range of trial values of λ yields $\lambda = 1.2 \pm 0.2$ for Sample I (Sample II; $\lambda = 1.1 \pm 0.2$)—indicating strong EPC more typical of a superconductor. The large uncertainty occurs because Δ has a broad minimum, indicating that the model does not describe the data as

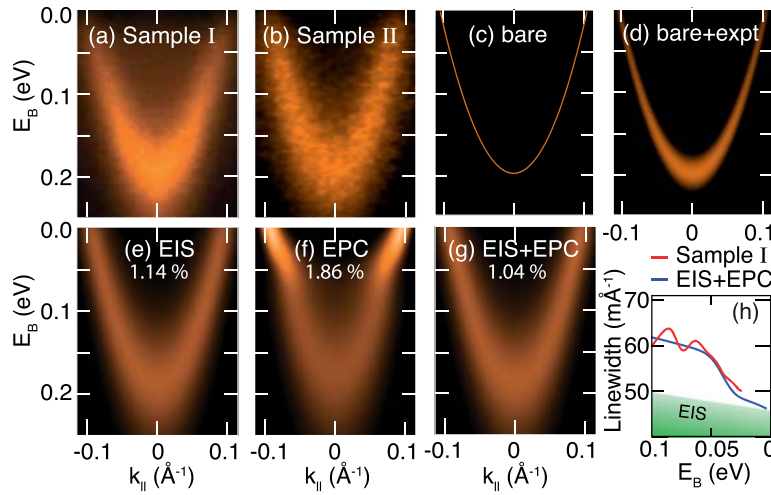


FIG. 2. ARPES measurements and simulations: (a) and (b) ARPES measurements for two nominally identical samples. Measurements are made in the $\langle 100 \rangle$ direction at $T = 100$ K and with photon energy 36 eV. (c) Calculated non-interacting “bare” 1Γ band (from Ref. 11). (d) Bare 1Γ band convolved with experimental momentum and energy resolutions. Simulations of the 1Γ state, including interactions; (e) EIS model ($W_0 = 70 \pm 12$ meV and $\lambda = 0$), (f) EPC model ($W_0 = 0$ meV and $\lambda = 1.2 \pm 0.2$) and (g) combined EIS + EPC model ($W_0 = 61$ meV and $\lambda = 0.14 \pm 0.04$), with Δ (the normalised rms difference for Sample I), quoted in each case. (h) Measured (red) and simulated (blue) linewidths extracted in the energy range 0 to 0.1 eV for the EIS + EPC model. The EIS contribution is represented in green. The Fermi level in the simulations (c)–(g) has been matched to the experimental data.

accurately as the EIS model. This is also manifested in the magnitude of $\Delta = 1.86\%$ (66% worse than the EIS model in relative terms). In other words, the EIS model is significantly more accurate than the EPC model. The superiority of the EIS model over the EPC model is not at all surprising; at 100 K, the 4PP measurements indicate that EIS accounts for $\approx 7/8$ of the resistance, whereas EPC accounts for $\approx 1/8$.

Because EIS and EPC exhibit quite different self-energies, the two simulations (Figs. 2(e) and 2(f)) are dissimilar. In the EPC case, the horizontal linewidth of the state increases dramatically at binding energies larger than the phonon energy (whereas for EIS it varies little across this energy range), thus the energy dependence of the linewidth can be used to disentangle the various contributions.⁴³ By considering the measured and simulated linewidth (Fig. 2(h)), it is therefore possible to construct a realistic EIS + EPC combined model (Fig. 2(g)). In order to reproduce the ARPES data, $W_0 = 61$ meV is chosen and $\lambda = 0.14 \pm 0.04$ is found from minimising Δ .

It should be restated that it is quite straightforward to disentangle the EPC and EIS contributions to the linewidth; W_0 is chosen such that the approximately constant part of the linewidth matches the measurement (indicated by the shaded green region in Fig. 2(h)), whereas the phonon energy (coincidentally very similar; 60 meV) causes a ‘step’ in the linewidth. The good agreement between the simulated and measured linewidth increase at 40 to 60 meV (Fig. 2(h), blue and red traces, respectively) confirms 60 meV to be relevant phonon energy.

For the combined EIS + EPC model, $\Delta = 1.04\%$. This small improvement (9% relative to the EIS model) is significant considering that the EPC part of the EIS + EPC model is small. A similar approach has been used for Sample II, and very similar results are gained. Notably, the EIS contribution is smaller ($W_0 = 65 \pm 10$ meV for the EIS model and 58 ± 8 for EIS + EPC).

Additionally, a small feature at ≈ 80 meV is observed in the linewidth of the experimental data (and is also present

for Sample II), suggesting that another phonon mode is contributing. No such phonon is expected in bulk silicon,⁴² and cannot be easily explained by P dopants, since the associated change in mass by substituting Si with P is very small. Naively applying a diatomic chain model, a mass of ≈ 11 nucleons would be required to create such a change in the optical phonon energy, suggesting that a lattice vacancy, or a very light contaminant, are more reasonable candidates.

EIS is expected to be strongly dependent on the impurity density and nominally identical samples may differ slightly in this respect.⁴³ The two samples were grown using different Si evaporation sources; probably the source of non-identical impurity densities. Indeed, although δ -doped samples can be easily reproduced, it is not surprising that even a slight change in the preparation conditions, can give rise to slightly different impurity levels. EPC, on the other hand, is well described primarily by coupling to bulk silicon phonon modes, and hence it is less sensitive to the preparation. 4PP measurements are consistent with this interpretation; for three nominally identical samples the impurity contribution varied by $\approx 20\%$.

Finally, it is interesting to notice from Fig. 2(g) that $\approx 7/8$ of the total linewidth can be accounted for by EIS, and $\approx 1/8$ by EPC—a very similar relationship seen in the relative contributions to the electrical resistance. Indeed, if EPC is ignored then W_0 increases by a similar proportion, from 61 meV (in the EIS + EPC model) to 70 meV, in order to falsely compensate for the EPC contribution.

In conclusion, the combination of ARPES measurements and simulations with 4-probe resistance measurements allows a better understanding of carrier interactions in electrical properties of δ -layer device platforms. Over the measured temperature range, EIS is the dominant mechanism (accounting for $\approx 7/8$ of the total interaction at $T = 100$ K), with the remaining $\approx 1/8$ accounted for by EPC (and EES is negligible). Specifically, the EPC is best understood primarily as a bulk silicon optical phonon interacting with the 1Γ

state of the δ -layer—an interaction which cannot occur in semiconducting silicon and is hence particular to region around the δ -layer. An intriguing implication is that accurately placed extrinsic dopants can be used as a local probe of phonon modes.

The impurity interaction appears to vary even for nominally identical samples, indicating that control of contamination and crystal defect densities is important for δ -layer derived devices. Nevertheless, the impurity level contributing to the self energy of the system is found to be small in absolute terms and comparable with the impurity level of high quality monolayer graphene samples.³⁸ A further insight into the impurity nature is gained from the observation of a 80 meV feature, which cannot be explained as a bulk silicon mode and is perhaps due to low mass impurities or lattice vacancies. Having a direct measure of impurity interactions will facilitate further optimisation of the growth and allow finer details of the bandstructure to be revealed.

Significantly, the approach used here is not limited to Si(001) δ -layers and could be applied to other crystallographic directions, or other materials where understanding interactions in reduced dimensions is important; in particular, in the development and performance of nanoscale electronics and quantum computation components.

M.Y.S. is supported by the ARC Centre of Excellence for Quantum Computation and Communication Technology (Project No. CE110001027) and the U.S. National Security Agency and the U.S. Army Research Office under Contract No. W911NF-08-1-0527. M.Y.S. acknowledges the ARC for providing a Laureate Fellowship. J.A.M. acknowledges the Lundbeck Foundation for providing financial support.

¹M. Lundstrom, *Science* **299**, 210 (2003).

²M. Jeong, B. Doris, J. Kedzierski, K. Rim, and M. Yang, *Science* **306**, 2057 (2004).

³E. Vogel, *Nat. Nanotechnol.* **2**, 25 (2007).

⁴B. Weber, S. Mahapatra, H. Ryu, S. Lee, A. Fuhrer, T. C. G. Reusch, D. L. Thompson, W. C. T. Lee, G. Klimeck, L. C. L. Hollenberg *et al.*, *Science* **335**, 64 (2012).

⁵F. J. Ruess, M. El Kazzi, L. Czornomaz, P. Mensch, M. Hopstaken, and A. Fuhrer, *Appl. Phys. Lett.* **102**, 082101 (2013).

⁶M. Fuechsle, S. Mahapatra, F. Zwanenburg, M. Friesen, M. Eriksson, and M. Simmons, *Nat. Nanotechnol.* **5**, 502 (2010).

⁷M. Fuechsle, J. A. Miwa, S. Mahapatra, H. Ryu, S. Lee, O. Warschkow, L. C. L. Hollenberg, G. Klimeck, and M. Y. Simmons, *Nat. Nanotechnol.* **7**, 242 (2012).

⁸C. M. Polley, W. R. Clarke, J. A. Miwa, M. Y. Simmons, and J. W. Wells, *Appl. Phys. Lett.* **101**, 262105 (2012).

⁹C. M. Polley, W. R. Clarke, J. A. Miwa, G. Scappucci, J. W. Wells, D. L. Jaeger, M. R. Bischof, R. F. Reidy, B. P. Gorman, and M. Simmons, *ACS Nano* **7**, 5499 (2013).

¹⁰J. A. Miwa, P. Hofmann, M. Y. Simmons, and J. W. Wells, *Phys. Rev. Lett.* **110**, 136801 (2013).

¹¹J. A. Miwa, O. Warschkow, D. J. Carter, N. A. Marks, F. Mazzola, M. Y. Simmons, and J. W. Wells, *Nano Lett.* **14**, 1515 (2014).

¹²D. W. Drumm, A. Budi, M. C. Per, S. P. Russo, and L. C. L. Hollenberg, *Nanoscale Res. Lett.* **8**, 111 (2013).

¹³D. J. Carter, O. Warschkow, N. A. Marks, and D. R. McKenzie, *Phys. Rev. B* **79**, 033204 (2009); **80**, 049901 (2009).

¹⁴D. J. Carter, N. A. Marks, O. Warschkow, and D. R. McKenzie, *Nanotechnology* **22**, 065701 (2011).

¹⁵S. Lee, H. Ryu, H. Campbell, L. C. L. Hollenberg, M. Y. Simmons, and G. Klimeck, *Phys. Rev. B* **84**, 205309 (2011).

¹⁶D. W. Drumm, L. C. L. Hollenberg, M. Y. Simmons, and M. Friesen, *Phys. Rev. B* **85**, 155419 (2012).

¹⁷J. S. Smith, J. H. Cole, and S. P. Russo, *Phys. Rev. B* **89**, 035306 (2014).

¹⁸S. R. McKibbin and D. A. Micha, *J. Phys. Chem. Lett.* **1**, 1073 (2010).

¹⁹T. Vazhappilly and D. A. Micha, *Chem. Phys. Lett.* **570**, 95 (2013).

²⁰P. Hofmann and J. W. Wells, *J. Phys.: Condens. Matter* **21**, 013003 (2009).

²¹L. Oberbeck, N. J. Curson, M. Y. Simmons, R. Brenner, A. R. Hamilton, S. R. Schofield, and R. G. Clark, *Appl. Phys. Lett.* **81**, 3197 (2002).

²²S. R. McKibbin, W. R. Clarke, A. Fuhrer, and M. Y. Simmons, *J. Cryst. Growth* **312**, 3247 (2010).

²³J. W. Wells, K. Handrup, J. F. Kallehauge, P. Bøggild, M. B. Balslev, J. E. Hansen, P. R. E. Petersen, and P. Hofmann, *J. Appl. Phys.* **104**, 053717 (2008).

²⁴E. Perkins, L. Barreto, J. Wells, and P. Hofmann, *Rev. Sci. Instrum.* **84**, 033901 (2013).

²⁵T. Ando, A. B. Fowler, and F. Stern, *Rev. Mod. Phys.* **54**, 437 (1982).

²⁶J. W. Wells, J. F. Kallehauge, and P. Hofmann, *J. Phys.: Condens. Matter* **19**, 176008 (2007).

²⁷J. W. Wells, J. F. Kallehauge, T. M. Hansen, and P. Hofmann, *Phys. Rev. Lett.* **97**, 206803 (2006).

²⁸K. E. J. Goh, M. Y. Simmons, and A. R. Hamilton, *Phys. Rev. B* **76**, 193305 (2007).

²⁹Here, we extend the definition of “impurity” to include surface localised defects, non-surface physical defects and foreign particles.

³⁰G. Berner, M. Sing, H. Fujiwara, A. Yasui, Y. Saitoh, A. Yamasaki, Y. Nishitani, A. Sekiyama, N. Pavlenko, T. Kopp *et al.*, *Phys. Rev. Lett.* **110**, 247601 (2013).

³¹B. Jensen, S. Butorin, T. Kaurila, R. Nyholm, and L. Johansson, *Nucl. Instrum. Methods Phys. Res., Sect. A* **394**, 243 (1997).

³²P. Dziawa, B. J. Kowalski, K. Dybko, R. Buczko, A. Szczerbakow, M. Szot, E. Łusakowska, T. Balasubramanian, B. M. Wojek, M. H. Berntsen *et al.*, *Nature Mater.* **11**, 1023 (2012).

³³P. Hofmann, I. Y. Sklyadneva, E. D. L. Rienks, and E. V. Chulkov, *New J. Phys.* **11**, 125005 (2009).

³⁴S. V. Kravchenko and M. P. Sarachik, *Rep. Prog. Phys.* **67**, 1 (2004).

³⁵The ARPES data first undergo a background subtraction, and an intensity normalisation.

³⁶G. Grimvall, *The Electron-Phonon Interaction in Metals* (North-Holland, 1981).

³⁷J. E. Gayone, C. Kirkegaard, J. W. Wells, S. V. Hoffmann, Z. Li, and P. Hofmann, *Appl. Phys. A: Mater. Sci. Process.* **80**, 943 (2005).

³⁸J. C. Johannsen, S. Ulstrup, M. Bianchi, R. Hatch, D. Guan, F. Mazzola, L. Hornekar, F. Fromm, C. Raidel, T. Seyller *et al.*, *J. Phys.: Condens. Matter* **25**, 094001 (2013).

³⁹C. Kirkegaard, T. K. Kim, and P. Hofmann, *New J. Phys.* **7**, 99 (2005).

⁴⁰J. Kröger, *Rep. Prog. Phys.* **69**, 899 (2006).

⁴¹F. Mazzola, J. W. Wells, R. Yakimova, S. Ulstrup, J. A. Miwa, R. Balog, M. Bianchi, M. Leandersson, J. Adell, P. Hofmann *et al.*, *Phys. Rev. Lett.* **111**, 216806 (2013).

⁴²S. Wei and M. Y. Chou, *Phys. Rev. B* **50**, 2221 (1994).

⁴³R. C. Hatch, M. Bianchi, D. Guan, S. Bao, J. Mi, B. B. Iversen, L. Nilsson, L. Hornekar, and P. Hofmann, *Phys. Rev. B* **83**, 241303 (2011).

“Determining the Electronic Confinement of a Subsurface Metallic State”

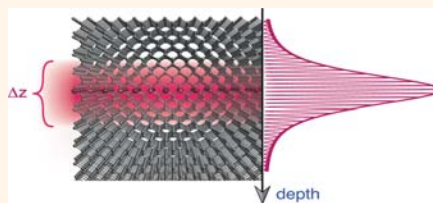
ACS Nano 8, 10 pp 10223-10228 (2014)

Determining the Electronic Confinement of a Subsurface Metallic State

Federico Mazzola,[†] Mark T. Edmonds,[‡] Kristin Høydalsvik,[†] Damien John Carter,[§] Nigel A. Marks,[§] Bruce C. C. Cowie,^{||} Lars Thomsen,^{||} Jill Miwa,[⊥] Michelle Yvonne Simmons,[#] and Justin W. Wells^{*,†}

[†]Department of Physics, Norwegian University of Science and Technology (NTNU), N-7491 Trondheim, Norway, [‡]School of Physics, Monash University, Clayton, Victoria 3800, Australia, [§]Nanochemistry Research Institute, Curtin University, Perth, WA 6845 Australia, ^{||}Australian Synchrotron, Clayton, Victoria 3168, Australia, [⊥]Department of Physics and Astronomy, Interdisciplinary Nanoscience Center (iNANO), University of Aarhus, 8000 Aarhus C, Denmark, and [#]Centre of Excellence for Quantum Computation and Communication Technology, School of Physics, University of New South Wales, Sydney, NSW 2052, Australia

ABSTRACT Dopant profiles in semiconductors are important for understanding nanoscale electronics. Highly conductive and extremely confined phosphorus doping profiles in silicon, known as Si:P δ -layers, are of particular interest for quantum computer applications, yet a quantitative measure of their electronic profile has been lacking. Using resonantly enhanced photoemission spectroscopy, we reveal the real-space breadth of the Si:P δ -layer occupied states and gain a rare view into the nature of the confined orbitals. We find that the occupied valley-split states of the δ -layer, the so-called 1Γ and 2Γ , are exceptionally confined with an electronic profile of a mere 0.40 to 0.52 nm at full width at half-maximum, a result that is in excellent agreement with density functional theory calculations. Furthermore, the bulk-like Si $3p_z$ orbital from which the occupied states are derived is sufficiently confined to lose most of its p_z -like character, explaining the strikingly large valley splitting observed for the 1Γ and 2Γ states.



KEYWORDS: Si:P δ -layers · photoemission · 2D confinement · quantum computation

Exceptionally sharp and high-density doping profiles in semiconductors (known as δ -layers) have been attracting interest over the past few years both because of their role as a platform for prototype quantum computation components^{1–3} and for the fascinating insight into reduced dimension electronics.^{4–9} Shallow buried layers of phosphorus (P) in bulk silicon (Si) are found to be a particularly suitable platform because of the high doping densities¹⁰ (and hence low sheet resistances^{11,12}) and the almost atomically sharp confinement potentials which can be formed.¹³ Such physical confinement gives rise to a nearly free-electron-like occupied band dispersion, the calculation of which has been the center of much effort.^{13–19} The occupied band structure has also recently been verified by photoemission spectroscopy (PES).^{6,20} The experimental verification is only possible because of a strongly enhanced photoemission intensity which occurs when an electron from a two-dimensional (2D) initial state is photoemitted via a well-matched bulk-like final state.^{20,21}

While the growth and characterization of Si:P δ -layers have been widely studied using

a range of techniques, important questions remain about the physical confinement of the 2D electronic states. The physical placement of the dopant atoms can be controlled and measured,^{10,11,22} but the electronic confinement, which is the key to understanding electronic parameters such as valley splitting, has been accessible only through calculations.^{6,13–19} Here we show that the strongly peaked photoemission enhancement, which allows the δ -layer states to be visible, also allows the physical profile of their wave function to be extracted. In particular, we demonstrate that the breadth of the spectral envelope and the Bloch-like part of the wave function and the photoionization cross section can be investigated. These parameters are found to be related to the bulk-like conduction band minimum (CBM) from which the occupied δ -layer states are derived and give a further insight into the nature of the δ -layer electronic states and their confinement.

The presence of a high density, atomically sharp, n-type dopant layer in a bulk semiconductor causes the bulk CBM to become partially occupied in the region close to the

* Address correspondence to quantum.wells@gmail.com.

Received for review June 19, 2014 and accepted September 22, 2014.

Published online September 22, 2014
10.1021/nn5045239

© 2014 American Chemical Society

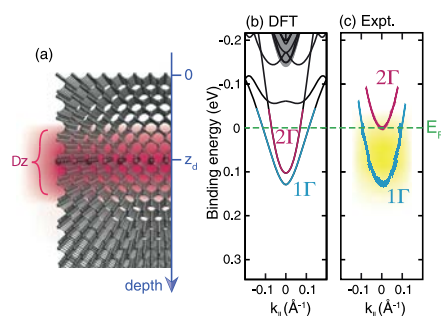


Figure 1. δ -Layer band structure and density of states. (a) Idealized schematic of the δ -layer sample where depth $z = 0$ corresponds to the sample surface and $z = z_\delta$ is the depth at which the dopants are placed. Δz and the red shading indicate the breadth of the electrical confinement (dopant atoms are indicated as larger dark spheres). (b) DFT-calculated band structure for an atomically sharp dopant plane (bulk CBM is shaded gray) and (c) corresponding measured band structure (adapted from ref 6; copyright 2014 American Chemical Society). The yellow shading indicates the region that contributes to the angle-integrated photoemission intensity in Figure 2.

dopant plane, thus creating a confined metallic layer (see Figure 1a). Density functional theory (DFT) and angle-resolved photoemission spectroscopy (ARPES) have revealed that the two partially occupied states, referred to as 1Γ (cyan) and 2Γ (magenta), have a dispersion which is well-approximated as parabolic, with the band minimum at the center of the layer's 2D Brillouin zone (see Figure 1b,c, respectively). The measured valley splitting, or energy separation of 1Γ and 2Γ , is large compared to the DFT-calculated valley splitting shown in Figure 1b. However, the valley splitting in DFT calculations has been shown to be highly sensitive to the in-plane arrangement of phosphorus atoms in the δ -plane (see ref 13 and the Supporting Information of ref 6), the details of which have not been observable experimentally. In all aspects other than the valley splitting, the agreement between DFT and measurements is excellent.

RESULTS

A photoemission experiment performed around normal emission, with a suitable angular integration ($\pm 1.7^\circ$), can be taken as a measure of the occupied density of states (DOS). The DOS integrated in this range consists of contributions from both 1Γ and 2Γ (see Figure 1c). Photoemission is also sensitive to the available unoccupied states; in order to transport the excited electron from the buried δ -layer to the surface, the final state must be delocalized from the δ -layer; in other words, it is a 3D bulk-like state. Since both energy and momentum are conserved in the excitation,²³ the photoemission probability depends strongly on the availability of a final state of suitable energy and momentum. Probing this condition ultimately allows

us to measure the real-space profile of the 2D initial state.

Since the photoexcitation conserves energy, varying the excitation energy changes the availability of final states. This is seen in the experimental data (Figure 2a) as a change in the photoemission intensity near the Fermi level. Using the relationship $k_\perp \approx [(2m/\hbar^2)(V_0 + h\nu - E_b - \Phi)]^{1/2}$, where V_0 is the inner potential and Φ is the sample work function,²³ the photon energy scale can be converted simply into units of crystal momentum (Figure 2b). Integrating the binding energy region of -0.1 to $+0.1$ eV (*i.e.*, the total intensity from the δ -layer initial states; 1Γ and 2Γ) makes the resonant behavior more clear; the integrated intensity from Figure 2b is plotted in Figure 2d. The photoemission intensity can generally be described as a function that is periodic in momentum, with a characteristic width in k_\perp . A synchrotron beamline with a lower photon energy range allows an additional period at lower k_\perp to be observed (Figure 2c).²⁴

Due to the 3D nature of the bulk-like final state (b_f), the final state will show a periodic dispersion in energy as a function of momentum k_\perp .^{21,23,25} The 2D nature of the initial states 1Γ and 2Γ results in a lack of such dispersion, thus they are depicted at constant binding energy (see Figure 3a). Since the photoexcitation involves a well-defined amount of energy, and a negligible amount of k_\perp ,²³ it is naïvely possible to see where the photoexcitation can occur. At two different photon energies chosen for illustration, $h\nu_1$ and $h\nu_2$, excitation from 2Γ to the bulk state can only occur for the particular values of k_\perp indicated in Figure 3a. In fact, it is this consideration (in combination with the assumption of a free-electron-like vacuum state) which allows the experimental data (Figure 2b–d) to be plotted in units of k_\perp .²³

DISCUSSION

Although the initial states are dispersionless in k_\perp , they are not of uniform intensity. This can be seen from a Fourier transform (FT) of the real-space distribution, which reveals that the distribution in k_\perp has a width defined by the inverse of the real-space breadth, centered on the Bloch momentum (Figure 3e). 1Γ and 2Γ are derived from the bulk CBM close to the out-of-plane Brillouin zone boundary; hence, they have Bloch momentum similar to that of the BZ boundary, k_{BZ} .²⁰ The strongly peaked FT intensity is the origin of the strongly peaked photoemission intensity; at particular photon energies, photoexcitation can occur at values of k_\perp which match the initial state Bloch momentum where the majority of the initial state spectral weight is found, with a suitable final state.

In fact, the situation is not quite so simple since the final state breadth must also be considered. Since the final state is bulk-like, it can be depicted as a Bloch-like oscillation extending infinitely into the bulk (Figure 3c).

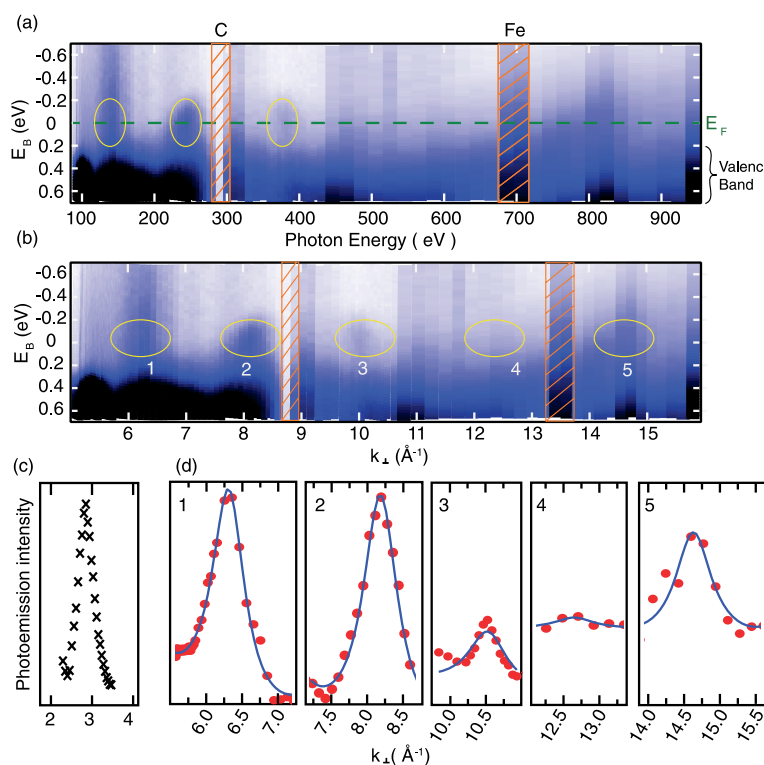


Figure 2. Photoemission measurements of the δ -layer states. (a) Photoemission intensity around the Fermi level for a range of photon energies (darker shades indicate higher intensity). The Fermi level (E_F) and the approximate energy of the valence band are indicated. The intensity has been normalized to the beamline flux. The markers “C” and “Fe” indicate where normalization is hindered by strong absorption by the beamline optics. Within the band gap, the photoemission intensity is enhanced at particular photon energies (enclosed in yellow ellipses). (b) Same photoemission intensity, converted into units of k_\perp with five enhancements indicated by yellow ellipses. (c) Integrated photoemission intensity for a similar sample, at smaller k_\perp (the absolute intensity cannot be compared between panels). (d) 1–5: Photoemission intensity (integrated in the energy range of -0.1 to $+0.1$ eV) for the range of k_\perp corresponding to each enhancement (as numbered in panel b). The blue line is a curve of form $I \propto (\chi - 1)^2 / (1 + \chi^2 - 2\chi \cos(k_\perp a - \pi))$ (see main text for details).

However, the final state probed by photoemission is attenuated into the bulk by an exponential decay, and the exponent depends on the mean free path (MFP) of the photoelectron, which in turn depends on the kinetic energy. Figure 3d depicts a final state modulated by a realistic MFP. The FT of this final state now has a nonzero width in k_\perp (see Figure 3e).

The implication of the finite FT widths is that the simplified picture of photoemission presented in Figure 3a needs to be modified; photoexcitation can occur at values of k_\perp which are not well matched to a final state, but the probability is reduced. This is illustrated in Figure 3f, where the photoexcitation is depicted by the broad arrow terminating at the right-hand side of the final state while originating from the left-hand side of the initial state. By comparison with the FT amplitudes presented in Figure 3e, it can be seen that such a photoexcitation *can* occur since both the initial and final states have a non-negligible

intensity here. In other words, the photoemission probability at a particular photon energy depends on the overlap of the initial state and final state FTs. As the photon energy is varied, there will be values at which the overlap is maximized, thus accounting for the peaked photoemission intensity observed in the measurements. The peak shape is determined by the convolution of the initial and final states (Figure 3g). More specifically, the full width at half-maximum (fwhm) of the peaked photoemission intensity depends on the real-space breadth of the initial state and the MFP assumed for the final state. The fwhm of the photoemission intensity is evaluated for a realistic range of MFP (0.6 to 1.2 nm for the energy range of 150 to 1000 eV)²⁶ and for a realistic range of initial state breadths (Figure 3h).

The simulation presented above focuses on the novel case of a subsurface 2D dopant plane. However, photoemission from other 2D initial states (in

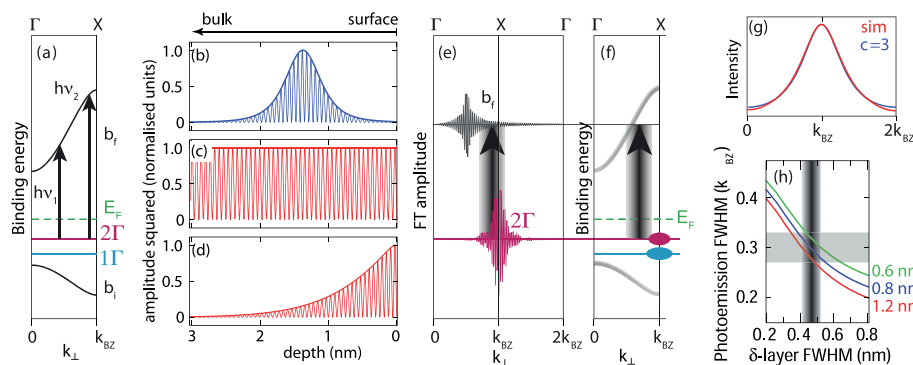


Figure 3. Schematic of the photoemission process. (a) Photoemission between a 2D initial state (2Γ) and a bulk-like final state (b_i). In the simple picture, for specific photon energies ($h\nu_1$ and $h\nu_2$), the photoexcitation can only occur at particular values of k_\perp such that energy and momentum are conserved. (b) Initial state and (c) final state models; the states are described by Lorentzian and semi-infinite distributions, respectively, but also comprise a Bloch-like part. The initial state (1Γ or 2Γ) is centered around the dopant plane 1.4 nm beneath the surface. (d) Same final state with an exponential decay describing the accessibility to photoemission by including a photoelectron MFP. (e) Fourier transform of initial and final states, showing that they have spectral weight over a range of k_\perp . The broad black arrow shows that photoexcitation can occur, even though the center values of k_\perp are mismatched. (f) Same photoexcitation in the schematic band structure. Although 2Γ is nondispersive, the spectral weight is strongly enhanced at particular k_\perp (indicated by the magenta ellipse). The final state is dispersive with a nonzero width in k_\perp . (g) Intensity of the convolution of the initial and final states, showing a strongly peaked distribution. Our numerical simulation (red) together with the expression from ref 21, with $\chi = 3$. In this particular case, a photoelectron MFP of 1 nm and an initial state fwhm of 0.3 nm are used. (h) Dependence of the fwhm of the simulated photoemission intensity on the initial state fwhm and photoelectron MFP. The horizontal gray band indicates the experimentally determined fwhm = $0.3k_{BZ} \pm 10\%$, and the vertical gray band indicates the corresponding range of initial state fwhm.

particular, surface states) is well understood, and a peaked photoemission intensity also occurs.^{21,25} This peaked intensity has been described by $I \propto (\chi - 1)^2 / (1 + \chi^2 - 2\chi \cos(k_\perp a - \pi))$, where I is the photoemission intensity, a is the reciprocal unit cell, and χ is a parameter describing the bandwidth of the 2D orbital relative to the bulk and the self-energy of the surface state (see ref 21 for full description). In order to facilitate a comparison between our simulation involving a subsurface 2D initial state and earlier work on surface-localized states, a curve of this form has been overlaid on both our numerical simulation presented in Figure 3g and the data in Figure 2d. In our case, χ is unknown, but the best agreement with our simulation is found when $\chi \approx 3$ (cf. $\chi = 1.6$ and 1.8 for the two surface states considered in ref 21). In other words, although our initial state has quite another origin than the surface states considered in earlier works, the photoemission model is very similar.

The fwhm of the measured photoemission intensity peaks has been found to be $\approx 0.9 \text{ \AA}^{-1}$, equivalent to $\approx 0.3k_{BZ}$, with an uncertainty of $\approx 10\%$. Our simulations show that this corresponds to a real-space fwhm of the initial state of just 0.40 to 0.52 nm (assuming an MFP in the range of 0.6 to 1.2 nm). Although the estimate for the initial state's fwhm depends on the estimate of the MFP, in this range, the dependence is weak, as seen in Figure 3h. This initial state breadth is exceptionally sharp, especially given that the distribution of dopant atoms is thought to be somewhat broader than this.¹¹

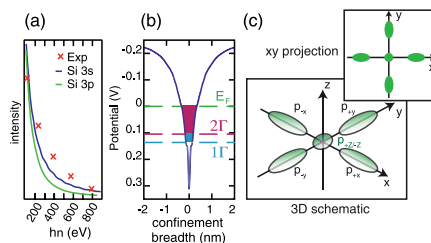


Figure 4. (a) Calculated Si 3s (blue) and 3p (green) photoionization cross sections²⁹ together with the experimental photoemission intensity (corrected for beamline flux and integration time). (b) DFT-calculated confinement potential, with the experimentally determined Fermi level and the approximate energies of the 1Γ and 2Γ band minima indicated. The breadth of the confinement potential at these energies is 0.68 nm (E_F), 0.36 nm (2Γ), and 0.30 nm (1Γ). (c) Schematic of the confined 3p orbitals, showing the s-like shape of the confined p_z orbital.

However, the same DFT calculation used to generate the band structure in Figure 1b yields a confinement potential on this length scale (Figure 4b). By aligning the DFT energy scale with the experimentally determined Fermi level, the confinement breadth at particular energies can be estimated. The breadth of the confinement potential is 0.68 nm (at E_F), 0.36 nm (at the 2Γ band minimum), and 0.30 nm (at the 1Γ band minimum).²⁷

As well as periodic oscillations in the photoemission intensity, the peak intensity rapidly diminishes with increasing k_\perp .²⁸ This is due to a decreasing

photoionization cross section and is a common observation which is well understood.²⁹ Since the 1Γ and 2Γ states are primarily derived from bulk Si $3p_z$ orbitals, one could expect that their photoionization cross section follows the calculated Si $3p$ values (see Figure 4a). However, the observed decay is weaker than the calculated curve and is more similar to (but still weaker than) the calculated Si $3s$ cross section. This is another consequence of the strong confinement; in the δ -layer, the p_z orbital is so strongly confined that it is more akin to a small, nearly spherical s orbital (see Figure 4c). Thus, the weakly decaying cross section is indicative of an orbital that is very small compared to a bulk-like Si $3p_z$.

It is intriguing that such a sharp δ -layer confinement can exist when the distribution of dopant atoms is known to be broader.¹¹ Since the photoemission experiment gives information on the initial states only when they are occupied, the relevant breadth corresponds to a metallic dopant density; in other words, it is the breadth at the "tip" of the dopant distribution that is relevant rather than its fwhm. By comparison with ref 11, it can be inferred that phosphorus densities on the order of $\approx 5 \times 10^{20} \text{ cm}^{-3}$ exist over a similar breadth (*i.e.*, 0.40 to 0.52 nm); thus it appears that dopant densities of this magnitude are needed to create a metallic 2D layer—this doping density is significantly higher than that in a 3D degenerate semiconductor, presumably because not all of the donated carriers remain in the 2D metallic region but also contribute to the strong (but not metallic) n -type doping of the surrounding silicon.

The out-of-plane confinement of the δ -layer states has wider implications for complex dopant arrangements; for example, the fact that we observe a confinement fwhm equivalent to just a few atomic spacings brings with it the implication that multiple δ -layers could be treated as independent if their separation is much larger than this confinement length scale. Conversely, multiple stacked δ -layers with a separation comparable to this length scale would be expected to interact. This view is supported by recent

calculations^{17,30} and forms the basis of novel 3D device architectures based on stacked δ -layers.³¹ Although our work has focused on the out-of-plane confinement of uniform 2D dopant structures, it is reasonable to assume that a similar length scale defines the in-plane confinement of patterned dopant structures, such as 1D wires⁷ and 0D quantum dots¹ and interacting multiple quantum dot devices.^{2,3}

CONCLUSION

The combination of synchrotron photoemission, simulations, and DFT calculations provides a detailed insight into the confinement of the Si $3p_z$ derived states (1Γ and 2Γ) that are responsible for the metallic 2D properties of a Si:P δ -layer.^{6,20} Strongly peaked photoemission intensity is a consequence of a strongly confined initial state, and from the peak width, it is possible to reconstruct the real-space breadth. Excellent agreement is found when the initial state is modeled as a Lorentzian envelope with a fwhm of 0.40 to 0.52 nm, containing a Bloch-like wave function similar to that of the bulk CBM from which the 1Γ and 2Γ states are derived. Such strong confinement results in the cross section of the orbital being modified away from that of an unconfined Si $3p$ orbital, as well as contributing to an unusually large valley splitting. By comparison with measurements of the phosphorus distribution, it appears that the confinement is derived from the high density "tip" of the dopant distribution, indicating that the formation of a 2D metallic layer requires a particularly high dopant density of around $5 \times 10^{20} \text{ cm}^{-3}$. DFT calculations are in good agreement not only in reproducing the band structure but also in producing a confinement potential which is consistent with the experimental observations. Importantly, the approach described here is not limited to Si:P but is applicable to understanding any 2D metallic layer which can be observed by photoemission. Furthermore, these results should provide valuable insight into the robustness of such doping profiles and their bearing on nanoscale electronics.

METHODS

Experimental Details. δ -Doped Si(001) samples are made *in situ* by first preparing a clean Si(001) sample (thermal annealing up to $\approx 1520 \text{ K}$ at a base pressure of $\approx 2 \times 10^{-10} \text{ mbar}$), and a sharp Si 2×1 reconstruction is seen by low-energy electron diffraction. This is followed by deposition of $\approx 1/4$ of a monolayer of phosphorus dopants (from phosphine gas dosed at room temperature for 5 min at a pressure of $5 \times 10^{-9} \text{ mbar}$) and subsequently incorporated into the surface by annealing to 520 K (as described elsewhere^{10,11,22}). A $\approx 1 \text{ nm}$ thick silicon epilayer is formed atop the dopant layer using a thermal evaporator, and the coverage is monitored and estimated by the relative intensities of the Si and P core levels acquired during the experiment. Such a coverage is selected to ensure that a confinement potential is formed that remains accessible by photoemission.^{6,20} Core-level

spectroscopy measurements confirmed minimal phosphorus dopant segregation for all annealing steps during sample preparation.

The data were collected at two beamlines, the soft X-ray beamline (SXR) at the Australian synchrotron (Melbourne)³² and at I4 beamline in MAX-IV laboratory (Lund, Sweden).³³ The measurements were performed at room temperature, and the angular acceptance was chosen to be approximately the same in both cases ($\pm 1.7^\circ$ centered at normal emission).

The data presented here have undergone an intensity normalization to the beamline flux, and the binding energy has been calibrated using a gold Fermi level.

DFT Methods. The 1Γ and 2Γ states (Figure 1b) have been calculated using the SIESTA code,³⁴ and the methods are described by Carter *et al.*¹⁷ An elongated three-dimensional unit cell, a double numerical plus polarization atom-centered basis set, and the generalized gradient approximation³⁵ were used

in order to represent the δ -layer. A suitable degree of electronic separation in the direction normal to the dopant plane is guaranteed by the separation of 40 atomic layers between the δ -layer and its periodic images. In the direction parallel to the dopant plane, a 4×4 simulation cell of 16 atoms has been adopted (in particular, 4 P and 12 Si in the δ -layer, the same as the experimental concentration of $1/4$ ML, or $2.2 \times 10^{14} \text{ cm}^{-2}$, ref 10). The resulting band structure, showing the 1Γ and 2Γ states, is represented in Figure 1b.

Conflict of Interest: The authors declare no competing financial interest.

Acknowledgment. We thank J. Adell for technical support at the MAX-IV laboratory, and O. Warschkow for assisting with the measurements and DFT calculations. J.M. acknowledges the Lundbeck Foundation via L. Hornekær for providing financial support. M.T.E. is supported by the ARC Laureate Fellowship project M.S. Fuhrer. M.Y.S. is supported by the Australian Research Council (ARC) Centre of Excellence for Quantum Computation and Communication Technology (project number CE110001027), and M.Y.S. is also supported by the U.S. National Security Agency and the U.S. Army Research Office under contract number W911NF-08-1-0527. M.Y.S. and N.A.M. acknowledge the ARC for providing fellowships. J.W.W. acknowledges NTNU's TSO materialer program for supporting the collaboration. This research was partially undertaken on the soft X-ray beamline at the Australian Synchrotron, Victoria, Australia.

REFERENCES AND NOTES

- Fuechsle, M.; Miwa, J. A.; Mahapatra, S.; Ryu, H.; Lee, S.; Warschkow, O.; Hollenberg, L. C. L.; Klimeck, G.; Simmons, M. Y. A Single-Atom Transistor. *Nat. Nanotechnol.* **2012**, *7*, 242–246.
- Weber, B.; Tan, Y. H. M.; Mahapatra, S.; Watson, T. F.; Ryu, H.; Rahman, R.; Hollenberg, L. C. L.; Klimeck, G.; Simmons, M. Y. Spin Blockade and Exchange in Coulomb-Confined Silicon Double Quantum Dots. *Nat. Nanotechnol.* **2014**, *9*, 430–435.
- Watson, T. F.; Weber, B.; Miwa, J. A.; Mahapatra, S.; Heijnen, R. M. P.; Simmons, M. Y. Transport in Asymmetrically Coupled Donor-Based Silicon Triple Quantum Dots. *Nano Lett.* **2014**, *14*, 1830–1835.
- Polley, C. M.; Clarke, W. R.; Miwa, J. A.; Simmons, M. Y.; Wells, J. W. Microscopic Four-Point-Probe Resistivity Measurements of Shallow, High Density Doping Layers in Silicon. *Appl. Phys. Lett.* **2012**, *101*, 262105.
- Ohno, K.; Heremans, F. J.; Bassett, L. C.; Myers, B. A.; Toyli, D. M.; Jayich, A. C. B.; Palmström, C. J.; Awschalom, D. D. Engineering Shallow Spins in Diamond with Nitrogen Delta-Doping. *Appl. Phys. Lett.* **2012**, *101*, 082413.
- Miwa, J. A.; Warschkow, O.; Carter, D. J.; Marks, N. A.; Mazzola, F.; Simmons, M. Y.; Wells, J. W. Valley Splitting in a Silicon Quantum Device Platform. *Nano Lett.* **2014**, *14*, 1515–1519.
- Weber, B.; Mahapatra, S.; Ryu, H.; Lee, S.; Fuhrer, A.; Reusch, T. C. G.; Thompson, D. L.; Lee, W. C. T.; Klimeck, G.; Hollenberg, L. C. L.; Simmons, M. Y. Ohm's Law Survives to the Atomic Scale. *Science* **2012**, *335*, 64–67.
- Drumm, D. W.; Smith, J. S.; Per, M. C.; Budi, A.; Hollenberg, L. C. L.; Russo, S. P. *Ab Initio* Electronic Properties of Monolayer Phosphorus Nanowires in Silicon. *Phys. Rev. Lett.* **2013**, *110*, 126802.
- Ryu, H.; Lee, S.; Weber, B.; Mahapatra, S.; Hollenberg, L.; Simmons, M.; Klimeck, G. Atomistic Modeling of Metallic Nanowires in Silicon. *Nanoscale* **2013**, *5*, 8666–8674.
- McKibbin, S. R.; Clarke, W. R.; Fuhrer, A.; Simmons, M. Y. Optimizing Dopant Activation in SiP Double δ Layers. *J. Cryst. Growth* **2010**, *312*, 3247–3250.
- Polley, C. M.; Clarke, W. R.; Miwa, J. A.; Scappucci, G.; Wells, J. W.; Jaeger, D. L.; Bischof, M. R.; Reidy, R. F.; Gorman, B. P.; Simmons, M. Exploring the Limits of n-Type Ultra-shallow Junction Formation. *ACS Nano* **2013**, *7*, 5499–5505.
- Mazzola, F.; Polley, C. M.; Miwa, J. A.; Simmons, M. Y.; Wells, J. W. Disentangling Phonon and Impurity Interactions in δ -Doped Si(001). *Appl. Phys. Lett.* **2014**, *104*, 173108.
- Carter, D. J.; Marks, N. A.; Warschkow, O.; McKenzie, D. R. Phosphorus δ -Doped Silicon: Mixed-Atom Pseudopotentials and Dopant Disorder Effects. *Nanotechnology* **2011**, *22*, 065701.
- Carter, D. J.; Warschkow, O.; Marks, N. A.; McKenzie, D. R. Electronic Structure Models of Phosphorus δ -Doped Silicon. *Phys. Rev. B* **2009**, *79*, 033204; **2009**, *80*, 049901.
- Lee, S.; Ryu, H.; Campbell, H.; Hollenberg, L. C. L.; Simmons, M. Y.; Klimeck, G. Electronic Structure of Realistically Extended Atomistically Resolved Disordered Si:P δ -Doped Layers. *Phys. Rev. B* **2011**, *84*, 205309.
- Drumm, D. W.; Hollenberg, L. C. L.; Simmons, M. Y.; Friesen, M. Effective Mass Theory of Monolayer δ -Doping in the High-Density Limit. *Phys. Rev. B* **2012**, *85*, 155419.
- Carter, D. J.; Warschkow, O.; Marks, N. A.; McKenzie, D. R. Electronic Structure of Two Interacting Phosphorus δ -Doped Layers in Silicon. *Phys. Rev. B* **2013**, *87*, 045204.
- Drumm, D. W.; Budi, A.; Per, M. C.; Russo, S. P.; Hollenberg, L. C. L. *Ab Initio* Calculation of Valley Splitting in Monolayer δ -Doped Phosphorus in Silicon. *Nanoscale Res. Lett.* **2013**, *8*, 111.
- Smith, J. S.; Cole, J. H.; Russo, S. P. Electronic Properties of δ -Doped SiP and GeP Layers in the High-Density Limit Using a Thomas–Fermi Method. *Phys. Rev. B* **2014**, *89*, 035306.
- Miwa, J. A.; Hofmann, P.; Simmons, M. Y.; Wells, J. W. Direct Measurement of the Band Structure of a Buried Two-Dimensional Electron Gas. *Phys. Rev. Lett.* **2013**, *110*, 136801.
- Louie, S. G.; Thiry, P.; Pinchaux, R.; Petroff, Y.; Chanderis, D.; Lecante, J. Periodic Oscillations of the Frequency-Dependent Photoelectric Cross Sections of Surface States: Theory and Experiment. *Phys. Rev. Lett.* **1980**, *44*, 549–553.
- Goh, K. E. J.; Simmons, M. Y. Impact of Si Growth Rate on Coherent Electron Transport in Si:P Delta-Doped Devices. *Appl. Phys. Lett.* **2009**, *95*, 142104.
- Himpel, F. J. Experimental Determination of Bulk Energy Band Dispersions. *Appl. Opt.* **1980**, *19*, 3964–3970.
- Since the data in Figure 2c,d were collected on two different beamlines, a direct comparison of the absolute intensity has not been possible.
- Hofmann, P.; Søndergaard, C.; Agergaard, S.; Hoffmann, S. V.; Gayone, J. E.; Zampieri, G.; Lizzit, S.; Baraldi, A. Unexpected Surface Sensitivity at High Energies in Angle-Resolved Photoemission. *Phys. Rev. B* **2002**, *66*, 245422.
- Seah, M. P.; Dench, W. A. Quantitative Electron Spectroscopy of Surfaces: A Standard Data Base for Electron Inelastic Mean Free Paths in Solids. *Surf. Interface Anal.* **1979**, *1*, 2–11.
- Note that both 1Γ and 2Γ contribute to the photoemission intensity.
- A precise normalization of the intensity of the peak marked “5” in Figure 2b is difficult.
- Yeh, J. J.; Lindau, I. Atomic Subshell Photoionization Cross Sections and Asymmetry Parameters: $1 \leq Z \leq 103$. *At. Data Nucl. Data Tables* **1985**, *32*, 1–155.
- Drumm, D.; Per, M.; Budi, A.; Hollenberg, L.; Russo, S. *Ab Initio* Electronic Properties of Dual Phosphorus Monolayers in Silicon. *Nanoscale Res. Lett.* **2014**, *9*, 443.
- Scappucci, G.; Capellini, G.; Klesse, W. M.; Simmons, M. Y. New Avenues to an Old Material: Controlled Nanoscale Doping of Germanium. *Nanoscale* **2013**, *5*, 2600–2615.
- Cowie, B. C. C.; Tadich, A.; Thomsen, L. The Current Performance of the Wide Range (90–2500 eV) Soft X-ray Beamline at the Australian Synchrotron. *AIP Conf. Proc.* **2010**, *1234*, 307–310.
- Jensen, B.; Butorin, S.; Kaurila, T.; Nyholm, R.; Johansson, L. Design and Performance of a Spherical Grating Monochromator Used at MAX. *Nucl. Instrum. Methods Phys. Res., Sect. A* **1997**, *394*, 243–250.
- Soler, J. M.; Artacho, E.; Gale, J. D.; García, A.; Junquera, J.; Ordejón, P.; Sánchez-Portal, D. The Siesta Method for *Ab Initio* Order- N Materials Simulation. *J. Phys.: Condens. Matter* **2002**, *14*, 2745.
- Perdew, J. P.; Burke, K.; Ernzerhof, M. Generalized Gradient Approximation Made Simple. *Phys. Rev. Lett.* **1996**, *77*, 3865–3868.

“Controlling and tuning simultaneous conduction and valence band quantization in artificial, nearly atomic-scale doping profiles in semiconductors”

Work in progress

Is not included due to copyright

Paper 4

“Sub-band structure in asymmetric doping-profiles”

Work in progress

Is not included due to copyright

Paper 5

“Adsorbate induced modification of the confining barriers in a quantum box array”

Work in progress

Is not included due to copyright

Paper 6

“Boron-doped diamond preserving bulk-like properties at the near atomic scale”

Work in progress

Is not included due to copyright

Paper 7

“Direct observation of spin-polarized bulk bands in an inversion-symmetric semiconductor”

Nature Physics 10, 835{839} (2014)

Is not included due to copyright

“Kinks in the σ -Band of Graphene Induced by Electron-Phonon
Coupling”

Phys. Rev. Lett. 111, 216806 (2013)

Kinks in the σ Band of Graphene Induced by Electron-Phonon CouplingFederico Mazzola,¹ Justin W. Wells,^{1,*} Rositza Yakimova,² Søren Ulstrup,³ Jill A. Miwa,³ Richard Balog,³ Marco Bianchi,³ Mats Leandersson,⁴ Johan Adell,⁴ Philip Hofmann,³ and T. Balasubramanian⁴¹*Department of Physics, Norwegian University of Science and Technology (NTNU), N-7491 Trondheim, Norway*²*Department of Physics, Chemistry, and Biology, Linköping University, S-581 83 Linköping, Sweden*³*Department of Physics and Astronomy, Interdisciplinary Nanoscience Center (iNANO), Aarhus University, 8000 Aarhus C, Denmark*⁴*MAX IV Laboratory, Lund University, P. O. Box 118, 221 00 Lund, Sweden*

(Received 26 May 2013; published 21 November 2013; corrected 22 November 2013)

Angle-resolved photoemission spectroscopy reveals pronounced kinks in the dispersion of the σ band of graphene. Such kinks are usually caused by the combination of a strong electron-boson interaction and the cutoff in the Fermi-Dirac distribution. They are therefore not expected for the σ band of graphene that has a binding energy of more than ≈ 3.5 eV. We argue that the observed kinks are indeed caused by the electron-phonon interaction, but the role of the Fermi-Dirac distribution cutoff is assumed by a cutoff in the density of σ states. The existence of the effect suggests a very weak coupling of holes in the σ band not only to the π electrons of graphene but also to the substrate electronic states. This is confirmed by the presence of such kinks for graphene on several different substrates that all show a strong coupling constant of $\lambda \approx 1$.

DOI: 10.1103/PhysRevLett.111.216806

PACS numbers: 73.22.Pr, 63.70.+h, 81.05.ue

Many-body interactions can strongly affect the spectral function of solids, and their presence is frequently heralded by so-called kinks in the dispersion of the electronic states near the Fermi energy, as observed by angle-resolved photoelectron spectroscopy (ARPES). Such kinks are primarily caused by electron-boson interactions and many cases of electron-phonon [1–3] or electron-magnon [4] induced kinks have been reported. In the cuprate high-temperature superconductors, strong kinks have been found near the Fermi energy [5,6], and their origin as well as their significance for the mechanism for high-temperature superconductivity have given reason to some debate [7]. The observed kinks in the spectral function contain a wealth of information about the underlying many-body interactions, such as the strength of the coupling as a function of position on the Fermi surface, as well as the energy of the bosons [8]. Note, however, that the presence of kinks does not necessarily imply the presence of bosonic interactions in correlated materials [9].

The observation of a kink signals a strong change in the real part of the self-energy Σ' that describes the deviation of the observed dispersion from the single-particle picture [10]. The origin of this structure can most easily be understood by considering the imaginary part of the self-energy Σ'' that is inversely proportional to the lifetime of the ARPES photohole and related to Σ' via a Kramers-Kronig transformation. Far away from the Fermi energy E_F , a photohole can be filled by electrons from lower binding energies dropping into the hole, emitting a boson of energy $\hbar\omega_E$ to conserve energy and momentum. For binding energies smaller than $\hbar\omega_E$, this is no longer possible, leading to a marked increase in lifetime. The

corresponding decrease in Σ'' leads to a maximum in Σ' , and this gives rise to the kink [10].

The lack of occupied states above E_F (at low temperature) is thus crucial for the appearance of the kink, and many-body effect related dispersion kinks are only expected near E_F , at least for the coupling to bosonic modes. In this Letter, we report the observation of pronounced kinks near the top of the σ band in graphene or graphite (see Figs. 1 and 2). Since these states are found at a binding energy of >3.5 eV, the presence of such kinks is unexpected. We show that the observed spectral features can still be explained by a strong electron-phonon interaction but the role of the Fermi-Dirac distribution cutoff is assumed by the density of σ states. This novel mechanism suggests that the hole in the σ band primarily decays through electrons from the same band instead of electrons from the π band or the substrate. This is confirmed by the observation of a similarly strong coupling for a large variety of graphene systems.

ARPES data were collected for six different material systems at three different synchrotron radiation beam lines: graphite, epitaxial monolayer (MLG) and bilayer (BLG) graphene on SiC [11] at beam lines I3 [12] and I4 [13] of MAX-III, as well as MLG graphene on Ir(111), oxygen-intercalated quasi-free-standing monolayer graphene (QFMLG) on Ir(111), with and without Rb doping, on the SGM-3 line of ASTRID [14]. Measurements were carried out under ultrahigh vacuum and temperatures which are low compared to those required for the excitation of optical phonon modes (see Table I). The energy and momentum resolutions were better than 35 meV and 0.01 \AA^{-1} , respectively.

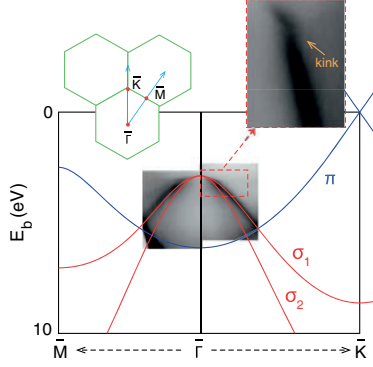


FIG. 1 (color online). Noninteracting (tight-binding) band structure of graphene, depicting the σ bands (red lines) and the π band (blue line) [15]. The Brillouin zone is depicted in the inset. The σ band consists of two branches σ_1 and σ_2 meeting at a common maximum at $\bar{\Gamma}$, with a binding energy of 3.5 to 4.0 eV. ARPES data for MLG graphene on SiC (gray scale) are superimposed. The detailed dispersion in the vicinity of the σ band maximum in the $\bar{\Gamma}$ - \bar{K} direction is magnified. The measured dispersion deviates from the noninteracting behavior, showing a clear kink accompanied by a band narrowing near the top of the σ band. The photon energy and temperature of data acquisition were $h\nu = 36$ eV and $T = 100$ K, respectively.

Figures 1 and 2 illustrate the strong renormalization of the σ band for different graphene systems. An overview is given in Fig. 1 showing the noninteracting (tight-binding) band structure of graphene [15] together with the ARPES data for MLG graphene on SiC (acquired at 100 K) near the top of the σ band. The general agreement of data and calculated band structure is satisfactory. However, a closer

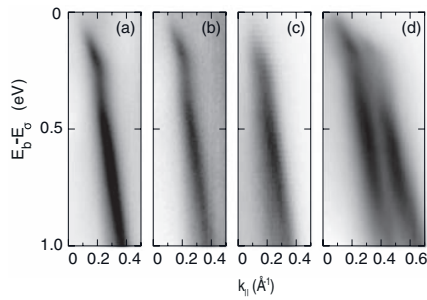


FIG. 2. ARPES data acquired for (a) quasi-free-standing monolayer graphene on Ir(111), (b) Rb-doped quasi-free-standing monolayer graphene on Ir(111), (c) monolayer graphene on SiC, and (d) bilayer graphene on SiC. The energy scales are plotted relative to the σ band maximum ($E_\sigma \approx 3.5$ eV). The dispersion direction corresponds to the $\bar{\Gamma}$ - \bar{K} for all the three systems. The photon energy of data acquisition was $h\nu = 36$ eV.

inspection shows the formation of a pronounced kink in the dispersion near the top of the band, accompanied by a band narrowing, the characteristic sign of a strong electron-boson interaction. While such kinks are expected and observed for doped graphene near the Fermi energy [8,16,17], their appearance at a high binding energy of ≈ 3.5 eV is unexpected. Results for graphene and bilayer graphene show that the strong renormalization is an ubiquitous feature (see Fig. 2). The energy scale in this figure has been defined relative to the top of the σ band extrapolated from the high energy dispersion of the bands. For these graphene systems, matrix element effects can strongly suppress the photoemission intensity of one or both of the σ bands at the chosen photon energy and experimental geometry [18]. Indeed, near normal emission, either it is only possible to see a single branch of the two forming the σ band or the intensity of one branch is drastically reduced compared to the other (see Fig. 2). Note that the loss of intensity near normal emission is a mere interference effect and should not be confused with the loss of spectral weight near the Fermi energy that is observed in the case of polaron formation [19].

While the electron-phonon coupling appears to be an obvious candidate for the appearance of the kinks, the mechanism must be very different from the situation near the Fermi level where the Fermi-Dirac function cutoff is ultimately responsible for the strong change in the self-energy. Consider the imaginary part of the self-energy Σ'' for the electron-phonon coupling [10,20]:

$$\Sigma''(\epsilon_i, T) = \pi \int_0^{\omega_{\max}} \{ \alpha^2 F^A(\epsilon_i, \omega) [1 + n(\omega) - f(\epsilon_i - \omega)] + \alpha^2 F^E(\epsilon_i, \omega) [n(\omega) + f(\epsilon_i + \omega)] \} d\omega + \Sigma''_0, \quad (1)$$

where $\alpha^2 F^{A(E)}$ are the Eliashberg coupling functions for phonon absorption (emission), ϵ_i is the initial state energy of the hole with respect to the top of the σ band, and ω is the phonon energy. n and f are Bose-Einstein and Fermi-Dirac distributions, respectively, and Σ''_0 accounts for electron-defect and electron-electron scattering, which is assumed to be independent of ϵ_i in the small energy range of interest here. Far from E_F , as in the present situation, we can approximate $f = 1$. If we assume that the electron-phonon interaction is dominated by an optical Einstein mode of $\hbar\omega_E \approx 190$ meV, we further find that $n(\omega_E) \ll 1$. The expression simplifies to

$$\Sigma''(\epsilon_i, T) = \pi \int_0^{\omega_{\max}} \alpha^2 F^E(\epsilon_i, \omega) d\omega + \Sigma''_0. \quad (2)$$

The crucial point now is that the Eliashberg function is strongly energy dependent: if we only consider electron-phonon scattering events within the σ band, a hole that is closer than $\hbar\omega_E$ to the top of the σ band cannot decay by the emission of an optical phonon, but a hole at a slightly larger binding energy can. More precisely, the phase space

for the electron-phonon scattering is given by the density of states in the σ band. For a two-dimensional (nearly) parabolic band, this density of states is well approximated by a step function. Hence, we can write the Eliashberg function as

$$\alpha^2 F^E(\epsilon_i, \omega) = \frac{\omega_E}{2} \lambda \delta(\omega - \omega_E) \Theta(\epsilon_i - \omega_E), \quad (3)$$

where λ is the electron-phonon coupling constant and Θ the Heaviside function. This corresponds to the standard model Eliashberg function for coupling to an Einstein mode but the mechanism is only permitted for $\epsilon_i > \omega_E$.

We test this model by using it to calculate the spectral function and compare it to the experimental data. This is illustrated in Fig. 3 for MLG on SiC at low temperature ($T = 100$ K). The phonon energy for an accurate description of the data can be directly read from the position of the kink to be $\hbar\omega_E \approx 190$ meV. Since the phonon for the intraband scattering needs to have a small wave vector,

this can be identified unambiguously as the E_{2g} optical mode also relevant for the scattering within the π band [8,21]. The only free parameters in the model are then λ , Σ_0'' , and those describing the parabolic bare band dispersion. From Σ'' , we obtain Σ' by a Kramers-Kronig transformation. The bare dispersion of the σ band is approximated by two parabolas (one parabola describing each branch).

For the comparison with the calculated spectral function, the measured data undergo a background subtraction and an intensity normalization (such that the measured geometry-induced difference in matrix elements between the $+k_{\parallel}$ and $-k_{\parallel}$ directions is averaged). The region $[-0.08 \leq k_{\parallel} \leq 0.08] \text{ \AA}^{-1}$ is excluded since the matrix elements are so small that the ARPES intensity approaches zero [18]. The simulated spectral function is convolved by experimental energy and momentum resolutions and normalized to the same intensity as the measurement. The agreement between measured and calculated spectral functions shown in Figs. 3(a) and 3(b) is quantified by the sum of the root-mean-square (rms) differences between the pixel values in the data and model. The parameters in the simulation (λ , Σ_0'' , and those describing the bare dispersion) are optimized until the lowest sum of rms differences is reached. Figure 3(c) shows that the difference between model and data is very small, at most a few percent. Figure 3(d) shows the sum of rms differences as a function of λ with all the other parameters optimized for each λ value. For the present case of MLG graphene on SiC, we find $\lambda = 0.96 \pm 0.04$.

The excellent agreement between the spectral function derived from our simple model and the data has several important implications: The observation of kinks is only possible if the density of states cutoff replaces the usual cutoff of the Fermi-Dirac function. This, in turn, implies that holes in the σ band are not filled by electrons from the (degenerate) π band, by electrons from the substrate (SiC, Ir), or from nearby atoms (O, Rb). This is not unexpected: In unperturbed graphene, there is no π - σ interaction and this should not change strongly in the presence of small lattice displacements. Scattering between the σ band and the substrate, or nearby atoms, is not expected to be strong either because the bonding to these is primarily mediated through the π electrons with little involvement of the σ band. The little importance of the substrate is supported further by the fact that the σ band kink is ubiquitous and of similar strength in several other graphene systems investigated here, as illustrated in Table I and already seen in Fig. 2. Indeed, the effect appears to be present independently of the substrate, decoupling by intercalation or electron doping. The coupling strength λ is only slightly smaller for BLG/SiC, indicating that interlayer interactions play a small role.

The values of λ reported in Table I are not only similar, they are also high on an absolute scale, in the same order of

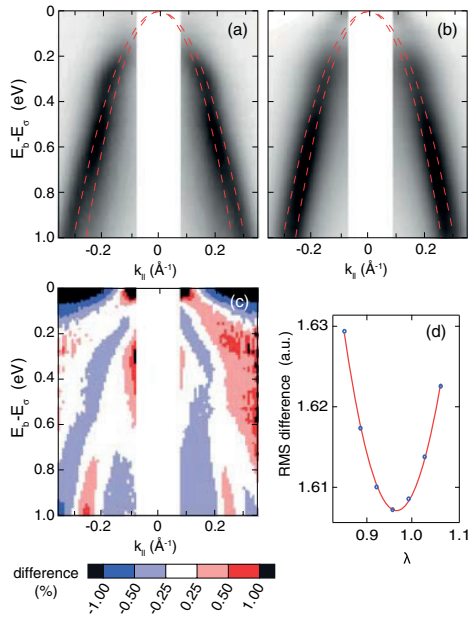


FIG. 3 (color online). (a) ARPES data for the σ band of MLG graphene on SiC along the \bar{K} - Γ - \bar{K} direction and (b) model spectral function derived from Eqs. (2) and (3). The binding energy is shown relative to the σ band maximum ($E_0 \approx 3.5$ eV). The red parabolas depict the expected dispersion in a noninteracting model. (c) Difference between (a) and (b). (d) Sum of the root-mean-square difference of the pixels in (a) and (b) as a function of λ , optimizing all the other parameters in the model for each λ value. The photon energy of data acquisition was $h\nu = 36$ eV and the temperature 100 K.

TABLE I. Results of the analysis carried out for different graphene systems. The electron-phonon coupling parameter λ and its uncertainty are quoted, together with the sample temperature (T) during acquisition of ARPES data.

System	$\lambda \pm \Delta\lambda$	T (K)
MLG/SiC	0.96 ± 0.04	100
MLG/SiC	0.97 ± 0.04	300
BLG/SiC	0.75 ± 0.05	100
Graphite	0.97 ± 0.04	100
MLG/Ir	0.97 ± 0.05	70
QFMLG/Ir	0.96 ± 0.04	70
QFMLG/Rb/Ir	0.96 ± 0.04	70

magnitude as for a strong coupling BCS superconductor [20]. This is in contrast to the π band where very small λ values have been found near E_F for the weakly p -doped case [22,23] and somewhat stronger coupling upon electron doping [8,16,17]. Note, however, that even though the density of states is zero both at the Dirac point and at the top of the σ band, its energy dependence is very different. It linearly increases for the π band but is a step function for the σ band. This step function is ultimately responsible for the observation of the kink because it instantaneously changes the coupling strength from zero to the high λ observed here. Energy-dependent changes of λ have been observed before [24], but in most (three-dimensional) systems, the changes in the density of states causing them are more gradual than here.

In conclusion, we have observed an electron-phonon coupling-induced kink near the top of the σ band of graphene. The kink is placed far away from the Fermi level and cannot be explained by the cutoff in the Fermi-Dirac function. Instead, its observation is ascribed to the quasi-instantaneous change in the density of states of the σ band. The electron-phonon coupling is found to be strong ($\lambda \approx 1$), and the kink is ubiquitous for graphene systems. Its presence suggests that the σ band is decoupled not only from the π states but also from the electronic states of the substrate. This is not unexpected but it also suggests that the strength of the observed kink can provide information of the interaction between graphene and its surroundings. The mechanism for the observed kink is neither limited to graphene nor to high binding energies. In fact, the only required ingredients are a pronounced change in the density of states combined with electron-boson coupling. The former is typically associated with band edges in (quasi-) two-dimensional systems. Therefore, similar band renormalizations could play a role in a variety of solids. They could even have an effect on transport properties and electronic instabilities when the band edges (almost) coincide with the Fermi energy. This is the case in several classes of materials, such as in iron pnictide superconductors [25,26], transition metal silicides [27], or transition metal dichalcogenites [28].

We gratefully acknowledge financial support from the Lundbeck Foundation, the VILLUM Foundation, and the Danish Council for Independent Research/Technology and Production Sciences. The work carried out at the MAX IV Laboratory was made possible through support from the Swedish Research Council and the Knut and Alice Wallenberg Foundations. T.B. acknowledges L. Walldén for his encouragement and discussions.

*quantum.wells@gmail.com

- [1] M. Hengsberger, R. Frésard, D. Purdie, P. Segovia, and Y. Baer, *Phys. Rev. B* **60**, 10 796 (1999).
- [2] S. LaShell, E. Jensen, and T. Balasubramanian, *Phys. Rev. B* **61**, 2371 (2000).
- [3] J.E. Gayone, C. Kirkegaard, J.W. Wells, S.V. Hoffmann, Z. Li, and P. Hofmann, *Appl. Phys. A* **80**, 943 (2005).
- [4] J. Schäfer, D. Schrupp, E. Rotenberg, K. Rossnagel, H. Koh, P. Blaha, and R. Claessen, *Phys. Rev. Lett.* **92**, 097205 (2004).
- [5] P. Johnson, T. Valla, A. Fedorov, Z. Yusof, B. Wells, Q. Li, A. Moodenbaugh, G. Gu, N. Koshinzuka, C. Kendziora *et al.*, *Phys. Rev. Lett.* **87**, 177007 (2001).
- [6] A. Lanzara, P.V. Bogdanov, X.J. Zhou, S.A. Kellar, D.L. Feng, E.D. Lu, T. Yoshida, H. Eisaki, A. Fujimori, K. Kishio *et al.*, *Nature (London)* **412**, 510 (2001).
- [7] P.W. Anderson, *Science* **316**, 1705 (2007).
- [8] M. Bianchi, E.D.L. Rienks, S. Lizzit, A. Baraldi, R. Balog, L. Hornekær, and P. Hofmann, *Phys. Rev. B* **81**, 041403 (2010).
- [9] K. Byczuk, M. Kollar, K. Held, Y.F. Yang, I.A. Nekrasov, T. Pruschke, and D. Vollhardt, *Nat. Phys.* **3**, 168 (2007).
- [10] P. Hofmann, I.Y. Sklyadneva, E.D.L. Rienks, and E.V. Chulkov, *New J. Phys.* **11**, 125005 (2009).
- [11] C. Virojanadara, M. Syvajarvi, R. Yakimova, L.I. Johansson, A.A. Zakharov, and T. Balasubramanian, *Phys. Rev. B* **78**, 245403 (2008).
- [12] T. Balasubramanian, B.N. Jensen, S. Urpelainen, B. Sommarin, U. Johansson, M. Huttula, A. Sankari, E. Nömmiste, S. Aksela, H. Aksela *et al.*, *AIP Conf. Proc.* **1234**, 661 (2010).
- [13] B. Jensen, S. Butorin, T. Kaurila, R. Nyholm, and L. Johansson, *Nucl. Instrum. Methods Phys. Res., Sect. A* **394**, 243 (1997).
- [14] S.V. Hoffmann, C. Søndergaard, C. Schultz, Z. Li, and P. Hofmann, *Nucl. Instrum. Methods Phys. Res., Sect. A* **523**, 441 (2004).
- [15] S. Reich, J. Maultzsch, C. Thomsen, and P. Ordejón, *Phys. Rev. B* **66**, 035412 (2002).
- [16] A. Bostwick, T. Ohta, T. Seyller, K. Horn, and E. Rotenberg, *Nat. Phys.* **3**, 36 (2007).
- [17] A. Bostwick, T. Ohta, J.L. McChesney, T. Seyller, K. Horn, and E. Rotenberg, *Solid State Commun.* **143**, 63 (2007).
- [18] E.L. Shirley, L.J. Terminello, A. Santoni, and F.J. Himpsel, *Phys. Rev. B* **51**, 13 614 (1995).
- [19] L. Perfetti, H. Berger, A. Regnelli, L. Degiorgi, H. Höchst, J. Voit, G. Margaritondo, and M. Grioni, *Phys. Rev. Lett.* **87**, 216404 (2001).

- [20] G. Grimvall, *The Electron-Phonon Interaction in Metals* (North-Holland, Amsterdam, 1981).
- [21] S. Y. Zhou, D. A. Siegel, A. V. Fedorov, and A. Lanzara, *Phys. Rev. B* **78**, 193404 (2008).
- [22] J. C. Johannsen, S. U. Ulstrup, M. Bianchi, R. Hatch, D. Guan, F. Mazzola, L. Hornekær, F. Fromm, C. Raidel, T. Seyller *et al.*, *J. Phys. Condens. Matter* **25**, 094001 (2013).
- [23] S. Ulstrup, M. Bianchi, R. Hatch, D. Guan, A. Baraldi, D. Alfè, L. Hornekær, and P. Hofmann, *Phys. Rev. B* **86**, 161402 (2012).
- [24] J. E. Gayone, S. V. Hoffmann, Z. Li, and P. Hofmann, *Phys. Rev. Lett.* **91**, 127601 (2003).
- [25] M. Yi, D. H. Lu, J. G. Analytis, J.-H. Chu, S.-K. Mo, R.-H. He, M. Hashimoto, R. G. Moore, I. I. Mazin, D. J. Singh *et al.*, *Phys. Rev. B* **80**, 174510 (2009).
- [26] J. Knolle, V. B. Zabolotnyy, I. Eremin, S. V. Borisenko, N. Qureshi, M. Braden, D. V. Evtushinsky, T. K. Kim, A. A. Kordyuk, S. Sykora *et al.*, *Phys. Rev. B* **86**, 174519 (2012).
- [27] A. F. Santander-Syro, M. Klein, F. L. Boariu, A. Nuber, P. Lejay, and F. Reinert, *Nat. Phys.* **5**, 637 (2009).
- [28] T. Rohwer, S. Hellmann, M. Wiesenmayer, C. Sohrt, A. Stange, B. Slomski, A. Carr, Y. Liu, L. M. Avila, M. Kallane *et al.*, *Nature (London)* **471**, 490 (2011).

Paper 9

“Strong electron-phonon coupling in the σ -band of graphene”

Work in progress

Is not included due to copyright

“Evidence of inter-band scattering between π - and σ -band of graphene”

Work in progress

Paper 10

Is not included due to copyright

“Resonant photoemission spectroscopy for intermediate band materials”

Appl. Phys. Lett. 107, 192104 (2015)



Resonant photoemission spectroscopy for intermediate band materials

F. Mazzola,¹ M. Nematollahi,¹ Z. S. Li,² S. Cooil,¹ X. Yang,¹ T. W. Reenaas,¹ and J. W. Wells^{1,a)}

¹Department of Physics, Norwegian University of Science and Technology (NTNU), NO-7491 Trondheim, Norway

²Department of Physics and Astronomy, Institute for Storage Ring Facilities, Aarhus (ISA), Ny Munkegade 120, Aarhus, DK-8000, Denmark

(Received 26 June 2015; accepted 29 October 2015; published online 11 November 2015)

Resonant photoemission spectroscopy is used to study the intermediate-band material Cr doped ZnS. Using resonant photoemission, we show that the intermediate-band can be characterized, revealing the filling and specific orbital character of the states contributing to the resonant photoemission signal. We demonstrate that resonant photoemission spectroscopy is a powerful approach for understanding the origin of intermediate bands in doped ZnS. The methodology can be widely extended to a large variety of materials, providing useful information towards engineering of high efficiency intermediate band solar cells and of other optoelectronic devices. © 2015 AIP Publishing LLC.
[<http://dx.doi.org/10.1063/1.4935536>]

Intermediate-band (IB) solar cells are devices consisting of a semiconductor with an electronic band within the material band-gap.^{1,2} Such a band can be created, for example, by means of doping or by creating quantum dots in the host material.³ IB-solar cells have attracted attention because of their high limiting-efficiency combined with a rather simple cell design.⁴ Indeed, an efficiency limit⁵ of 63% is predicted, cf. 41% for single gap solar cells, operating under the same conditions.¹ The increase in the efficiency arises because of the possibility of exciting electrons into the conduction band (CB) using multiple absorption processes.

In particular, in single gap solar cells, photons can excite electrons in the valence band (VB) and promote them into the CB; this mechanism can occur only if the energy of the excited electrons is at least the energy of the gap (E_g). In IB-solar cells not only the same mechanism can take place but also an additional 2-step process can occur. Indeed, since the IB forms within the band-gap, electrons of energy smaller than E_g can be first promoted into the IB, then from the IB can be excited into the CB. In other words, if the energy of the photons is not sufficient to promote an electron from the VB directly into the CB, the IB can be used as an additional stepping stone to generate electron-hole pairs.⁶

The combination of a high efficiency limit and a simple device design has resulted in an increasing interest in IB materials and IB-solar cells recently. A wide range of IB materials have been proposed and investigated, and characterization techniques for the device performance have been developed.⁴ For detection of IB states within the bandgap, optical techniques such as photo- and electroluminescence,⁷ photo-reflectance,⁸ and spectroscopic ellipsometry⁹ have been utilized, as well as electronic techniques such as deep level transient spectroscopy.¹⁰ In general, a full characterization of the IB is crucial in order to control and eventually tune material properties to develop materials which are suitable for real devices.

In this work, we introduce an additional powerful approach based on resonant photoemission spectroscopy (RPES)¹¹ to access the nature of an IB. Even though this technique has been proven to be an efficient method to investigate several exotic phenomena in solid state materials,^{12–17} it has not been used to characterize IB materials for photovoltaics. Specifically, we demonstrate that RPES is able to discriminate active and inactive orbital contribution of dopants, and directly probe the nature of the IB state, allowing for a quantification of the partial density of states (DOS) of such a band and the orbital character of the dopant species which give rise to it.

In this study, we use $\approx 4\%$ Cr-doped ZnS as a model material,^{18,19} but the same approach could be extended to a wide range of IB materials. The choice of ZnS as a test-material is related to the fact that its direct gap is quite large (3.6–3.9 eV), simplifying the detection of the Cr3d states responsible for the IB, forming within E_g . Moreover, ZnS is environmentally friendly, abundant, and is known to be a promising candidate for high-efficiency and non-toxic solar cells.^{18–20}

The principle on which RPES is based is a quantum-mechanical interference between a direct photoemission process and a recombination of an excited state.¹¹ In Cr-doped ZnS, the direct photoemission process occurs from Cr valence electrons: photons excite an electron from the 3d energy level and bring it into the vacuum with kinetic energy E_K as in Fig. 1(a), $1s^2 2s^2 2p^6 3s^2 3p^6 3d^n 4s^1 + h\nu \rightarrow 1s^2 2s^2 2p^6 3s^2 3p^6 3d^{(n-1)} 4s^1 + e^-$, where n depends on the oxidation state of the Cr atom.

In such a material, the partially occupied 3d electronic DOS (e-DOS) of Cr is responsible for creating an IB within the energy gap of ZnS. To probe the existence of such a band we vary the photon energy ($h\nu$) across the Cr2p absorption edge; specifically we vary $h\nu$ from 570 eV to 590 eV. When the photon energy matches the transition Cr2p \rightarrow Cr3d, electron transitions from the Cr2p into the Cr3d levels are possible. These electronic promotions can only occur for photon energies close to the Cr2p absorption edge¹¹ and are dictated

^{a)}quantum.wells@gmail.com

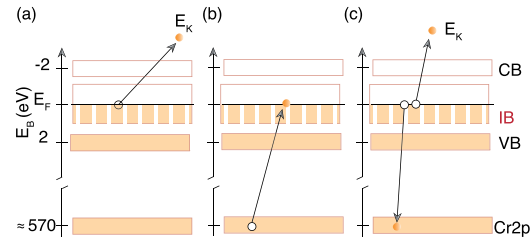


FIG. 1. Direct emission and resonant photoemission from the IB material; Cr doped ZnS. (a) Representation of the standard photoemission process: an electron is emitted from the IB (Cr3d in this illustration). (b) and (c) A secondary, 2-step, process: (b) the electron can be first excited from Cr2p into the Cr3d/IB state. (c) The Cr3d electron may then decay back to the Cr2p band by emission of another Cr3d electron. Both process ultimately lead to emission of a Cr3d electron and have the same initial and final states.

by the availability of unfilled (or partially filled) 3d orbitals and selection rules. In this recombination process, photons first promote a 2p electron into the 3d energy level, as illustrated in Fig. 1(b), then the extra electron in the 3d level decays back into the 2p level emitting a second electron with E_K , as in Fig. 1(c), $1s^2 2s^2 2p^6 3s^2 3p^6 3d^n 4s^1 + h\nu \rightarrow 1s^2 2s^2 2p^5 3s^2 3p^6 3d^{(n+1)} 4s^1 \rightarrow 1s^2 2s^2 2p^6 3s^2 3p^6 3d^{(n-1)} 4s^1 + e^-$.

The final state of the direct photoemission and the recombination process is the same, or alternatively E_K of the emitted electron is the same. This results in a resonant enhancement of the intensity of the 3d states visible in the RPES spectra within the ZnS gap.

Since the resonant photoemission process involves modifying the occupancy of the 3d level by $\pm 1e^-$, it is a requirement that the 3d level is partially filled; otherwise, a resonant enhancement cannot occur. In the case of Cr doped ZnS, it is reasonable to assume a tetrahedral crystal field, which separates the 3d level into t_{2g} and e_g bands derived from (d_{xy} , d_{yz} , d_{zx}) and ($d_{x^2-y^2}$, d_{z^2}) orbitals, respectively.¹⁸ t_{2g} and e_g may be partially filled and may show resonant behaviour. Since the energy of the Cr2p \rightarrow Cr3d transition is dissimilar for Cr2p $\rightarrow t_{2g}$ and Cr2p $\rightarrow e_g$, the photon energy required for resonance will be slightly different (as will the binding energy of the Cr3d t_{2g} and e_g states).

We performed the RPES experiment at MAT-line of the synchrotron radiation ASTRID2 and at D1011 beamline of MAX-II²¹ under ultrahigh vacuum conditions ($P < 10^{-9}$ mbar) and at room temperature. ZnS samples with a nominal 4% Cr doping grown by both MBE and PLD were measured (see Ref. 9 for details of the sample growth). Both samples undergo cycles of sputtering in order to remove the native oxides at the surface, unavoidably formed after exposure of the samples to air. The core levels were monitored to ensure the absence of external contaminants in both samples. Oxygen was not completely removed for the MBE sample even after several sputtering cycles. We believe that this is due to the presence of oxygen at ZnS grain boundaries in this particular sample.

The RPES spectra from the MBE-sample are shown in Fig. 2(b) as a 2-dimensional (2D) image in false color scale (from white to blue, indicating from weak to strong intensity, respectively). Each column of the 2D image contains the intensity of the RPES spectra collected for a certain value of

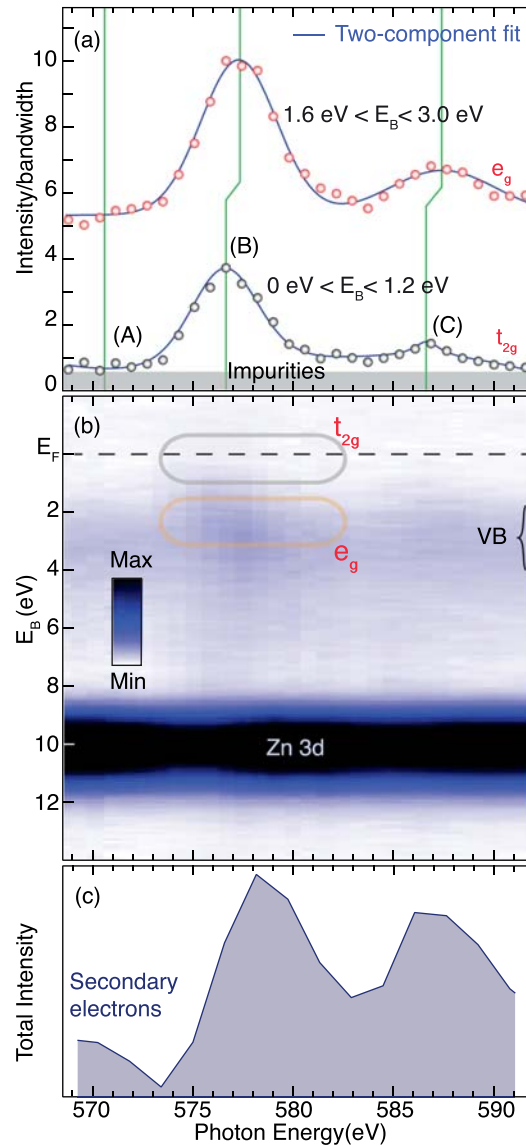


FIG. 2. RPES and XAS results. (a) Integrated RPES intensity in the range $E_B = 1.2-0$ eV (black markers) and $E_B = 3.0-1.6$ eV (red markers) normalized to the Zn3d core level and bandwidth. The markers are the experimental data and the blue lines are fit obtained by including only two components. The gray area is an approximate estimate of the impurity level in the sample. (b) 2D image plot in false color scale. Each column corresponds to one RPES spectrum and it is shown vs. photon energy. The resonant enhancements of the intensity close to the Fermi level and within the VB region and have been attributed to the orbital character Cr3d t_{2g} and e_g , respectively. (c) XAS measurements using partial electron yield. This measurement corresponds to the secondary electron emission from all processes.

photon energy. A typical RPES spectra, such as in Fig. 2(b), takes approximately 24 h of acquisition time. The same data are shown as an array of spectra in the supplementary material.²² In Fig. 2(b), the most visible contributions within the E_B -range acquired are the Zn3d core level and the VB

maximum, falling at $E_B \approx 10$ eV and $E_B \approx 2$ eV, respectively. Both Zn3d and VB are indicated in Fig. 2(b). When the photon energy matches the onset $\text{Cr2p} \rightarrow \text{Cr3d}$, the resonant condition discussed above can occur and the 3d state will be visible within the ZnS gap because of the resonant enhancement of the Cr3d direct emission process. This means that when the resonant condition is fulfilled, there will be an increase in the intensity occurring within the ZnS gap, and this is directly observable in the 2D image plot. In other words, we can directly see the IB-DOS in the bandgap of ZnS. However, the Cr dopants constitute only 4% of the ZnS amount; thus, the IB intensity within the ZnS gap is weak.

In Fig. 2(b), resonances are visible and appear as broad intensity enhancements centered at photon energies around 577 and 587 eV. In order to make the resonant behaviour more clear, the photoemission intensity is extracted from Fig. 2(b) by integrating over two binding energy ranges, $E_B = 3.0\text{--}1.6$ eV and $E_B = 1.2\text{--}0$ eV, depicted as the upper and lower traces of Fig. 2(a), respectively. Both of these regions show a resonant enhancement, but the photon energy of the resonant peak is shifted to higher photon energy for the larger binding energy resonance.

The two binding energy ranges chosen ($E_B = 3.0\text{--}1.6$ eV and $E_B = 1.2\text{--}0$ eV) correspond to the e_g and t_{2g} binding energies, respectively, from which the photoemission signal is enhanced in RPES in the $\text{Cr2p} \rightarrow e_g$ and $\text{Cr2p} \rightarrow t_{2g}$ transitions (assuming a tetrahedral crystal field¹⁸). In both transitions, the Cr2p initial state is the same, but the *final* states (e_g and t_{2g}) differ in binding energy by ≈ 1.6 eV.

In both of the traces plotted in Fig. 2(a), two broad peaks (indicated by “B” and “C” in the figure) are visible. Such peaks originate from a similar excitation processes except that their *initial* states are different, i.e., $\text{Cr2p}_{1/2}$ and $\text{Cr2p}_{3/2}$. A two component fit of the data integrated over the energy range $E_B = 1.2$ and 0 eV yields a splitting of 9.7 ± 0.2 eV, in good agreement with the expected spin-orbit splitting for $\text{Cr2p}_{1/2}$ and $\text{Cr2p}_{3/2}$.²³ The intensity of these two peaks could be expected to occur with a 1 : 2 ratio, reflecting the occupancy of the two initial states. However, the experimentally determined relative intensity is closer to 1:3. Such a difference can be attributed to the selection rules governing the transitions.^{24,25} Whilst the relevant initial states are known, the momentum and spin of the available final states in a partially filled transition metal 3d band are less clear; however, unequal filling with respect to spin is expected for magnetic elements such as Cr. Hence, the possible transitions between the spin-orbit coupled $p_{1/2}$ and $p_{3/2}$ initial states, and the spin-orbit coupled and spin non-degenerate 3d final states will require that spin and orbital angular momentum conservation restrictions are satisfied. In short, the partial filling of the Cr3d t_{2g} derived IB imposes restrictions on the orbital character of the initial states from which excitations can occur, when examining this specific excitation channel. Such restrictions are indicative of a high-spin configuration and will have implications for the photo-excitations, which can occur in a photovoltaic, ultimately influencing device efficiency.

A quantitative estimate of the occupation of differing orbital character of the Cr e-DOS can be achieved by integrating the energy range within the ZnS gap and normalizing it to the

Zn3d core level intensity to obtain the Cr3d t_{2g} contribution to the IB. From this and an estimate of the Cr3d e_g orbital character contribution to the VB, the identification of the Cr oxidation states can be made. If we integrate the intensity of the peaks in Fig. 2(a), we find that the intensity per unit bandwidth is very close to $e_g:t_{2g} = 2:1$. We therefore infer that e_g is half-filled (i.e., $2e^-$) and t_{2g} contains $1e^-$. This would be consistent with the Cr dopant being in the $2+$ oxidation state with an electronic configuration $1s^2 2s^2 2p^6 3s^2 3p^6 3d^3 4s^1$. This also finds agreement with the observed 1:3 intensity ratio of transitions involving the $p_{1/2}$ and $p_{3/2}$ initial states, which implied a high-spin configuration of the IB and VB states, i.e., half-filled e_g and partially filled t_{2g} orbitals.

It is also interesting to observe that the total intensity of photoemission from the IB state is close to 3% of the Zn3d band, i.e., close to the nominal doping of the Cr doped ZnS sample. This indicates that $\approx 100\%$ of the Cr dopants are contributing to the IB intensity. Since Cr is added in order to create the IB-DOS, any Cr present in the sample which is not contributing to it, corresponds to “wasted” Cr. One important aspect of photovoltaic material synthesis and characterisation is to understand and minimize such waste.

So far, we have focused on the dopant species contributing to the IB; however, the RPES analysis in Fig. 2(a) can also offer a quantitative estimate of the impurity concentration. Indeed, the constant offset in Fig. 2(a) is indicative of contributions to the DOS within the ZnS bandgap due to any element other than Cr. These contributions cannot be due to ZnS, since they are within the bulk bandgap, and they cannot be due to Cr because they do not resonate with the photon energy of the Cr edge. A precise quantification of this non-resonant DOS is challenging and we estimate it to be $\ll 1\%$ with respect to the Zn amount.

We have conducted highly complementary X-ray absorption spectroscopy (XAS) measurements on the same sample and with the same experimental setup used for RPES, but in this case, it is the low kinetic energy secondary electrons which are collected. The XAS results have been carefully calibrated and are summarized in Fig. 2(c). Whilst the RPES intensity at the Fermi level contains information on the Cr orbitals which are actively contributing to the IB-DOS, XAS contains information on the total amount of the Cr present. The XAS peaks appear at higher photon energy than the RPES peaks, indicating that there is a higher energy Cr transition contributing to the XAS signal. This could be due, for example, to a small quantity of Cr_2O_3 , which we believe to be present at grain boundaries, but which does not contribute to the IB-DOS. For high Cr concentrations, it is possible that metallic Cr clusters form, although not observable in our experimental data.

XAS measurements with partial yield are also important to rule out the possibility of a contribution to the RPES intensities from the second order light generated by the beamline. Indeed, in synchrotron experiments, for each excitation energy used $h\nu$, a small amount of second order light (with energy $2h\nu$) can be generated too (for MAT-line, this contribution is expected to be very small in this energy range). In principle, the second order light could give rise to additional core-level transitions, which would obfuscate the RPES data (but not the XAS data). The similarity of the

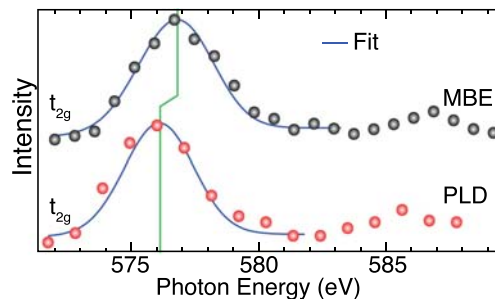


FIG. 3. Comparison of nominally identical samples grown by using MBE and PLD. The partial DOS is obtained by integrating the intensities in the range $E_B = 1.2$ – 0 eV. The blue line is the fitted peak position. The vertical green line indicates the maxima of the fit for the two samples.

XAS and RPES data confirms the detected features derive from the first order light. This is not surprising, given the low flux of $2h\nu$ expected at these energies. The second order photoemission would also give rise to linearly dispersing features in the RPES image in Fig. 2(b), and no such artefacts are observed.

To further illustrate the potential of the RPES method, we have investigated a nominally identical Cr doped ZnS sample grown by an alternative growth method, PLD. The results have been summarized in Fig. 3. The data have been both carefully calibrated for the photon energies used. Moreover, the nominal doping of the two samples is the same, which is also confirmed by the integrated RPES intensity, but subtle differences are also revealed. For the PLD sample, the intensity per unit bandwidth (integrated over the same limits as for the MBE sample) is $e_g:t_{2g} \approx 2:1.5$, indicating a slightly increased filling of the t_{2g} orbital (compared to the MBE sample). We infer that, whilst the MBE sample mainly contains Cr^{2+} with electronic configuration $1s^2 2s^2 2p^6 3s^2 3p^6 3d^3 4s^1$, the PLD sample contains relatively more Cr^{3+} with an increased occupancy of the $3d t_{2g}$ orbital. In any case, RPES allows subtle differences in the IB band to be seen for nominally identical samples.

In conclusion, we have demonstrated the applicability of RPES in studying IB materials relevant to photovoltaics. RPES is not only able to reveal quantitative information on the partial DOS within the material bandgap but also able to reveal the origin of these states and their orbital character. In the present case, we demonstrate the contribution of Cr orbitals in Cr doped ZnS, and are able to compare two similar samples prepared using different growth methods. In addition, we have performed XAS measurements, which facilitates an understanding of the total amount of each species present in the sample. Thus, the powerful combination of RPES and XAS allows us to understand the orbitals which actively contribute to the intermediate band. Such characterization of IB materials is important in the development of materials for high efficiency photovoltaics. Whilst we have concentrated on Cr doped ZnS, it is important to point out that this approach of combining XAS and RPES is of much broader relevance and can be applied to a large variety of IB materials such as complex oxides and quantum dots solar

cells, which have much potential as next generation photovoltaic devices.

Dr. A. Preobrajenski of beamline D1011 at the MAX IV Laboratory is gratefully acknowledged for his assistance and insightful discussions. This work was supported in part by The Norwegian Center for Solar Cell Technology, a Center for Environment-Friendly Energy Research co-sponsored by the Norwegian Research Council and Research and Industry in Norway (Project No. 193829). The authors also acknowledge the Research Council of Norway for financial support via the Nano2021 program (Project No. 203503).

¹A. Luque and A. Martí, *Phys. Rev. Lett.* **78**, 5014 (1997).

²Y. Okada *et al.*, "Intermediate band solar cells: Recent progress and future directions," *Appl. Phys. Rev.* **2**, 021302 (2015).

³T. Sogabe, Y. Shoji, M. Ohba, K. Yoshida, R. Tamaki, H.-F. Hong, C.-H. Wu, C.-T. Kuo, S. Tomić, and Y. Okada, *Sci. Rep.* **4**, 4792 (2014).

⁴I. Ramiro, A. Martí, E. Antolín, and A. Luque, *IEEE J. Photovoltaics* **4**, 736 (2014).

⁵W. Shockley and H. J. Queisser, *J. Appl. Phys.* **32**, 510 (1961).

⁶A. Luque, A. Martí, and C. Stanley, *Nat. Photonics* **6**, 146 (2012).

⁷A. Luque, A. Martí, N. López, E. Antolín, E. Cánovas, C. Stanley, C. Farmer, L. J. Caballero, L. Cuadra, and J. L. Balenzategui, *Appl. Phys. Lett.* **87**, 083505 (2005).

⁸K. M. Yu, W. Walukiewicz, J. Wu, W. Shan, M. A. Scarpulla, O. D. Dubon, J. W. Beeman, and P. Becla, *Phys. Status Solidi B* **241**, 660 (2004).

⁹M. Nematollahi, X. Yang, L. M. S. Ass, Z. Ghadyani, M. Kildemo, U. Gibson, and T. W. Reenaas, "Molecular beam and pulsed laser deposition of ZnS:Cr for intermediate band solar cells," *Sol. Energy Mater. Sol. Cells* **141**, 322–330 (2015).

¹⁰M. Ichimura, H. Sakakibara, K. Wada, and M. Kato, *J. Appl. Phys.* **114**, 114505 (2013).

¹¹C. Guillot, Y. Ballu, J. Pagné, J. Lecante, K. P. Jain, P. Thiry, R. Pinchaux, Y. Pétroff, and L. M. Falicov, *Phys. Rev. Lett.* **39**, 1632 (1977).

¹²H. Sato, M. Koyama, K. Takada, H. Okada, K. Shimada, Y. Ueda, J. Ghijsen, and M. Taniguchi, *J. Electron Spectrosc. Relat. Phenom.* **88**, 333–337 (1998).

¹³M. Weinelt, A. Nilsson, M. Magnuson, T. Wiell, N. Wassdahl, O. Karis, A. Föhlisch, N. Mårtensson, J. Störh, and M. Samant, *Phys. Rev. Lett.* **78**, 967 (1997).

¹⁴F. Mazzola, M. T. Edmonds, K. Høydalsvik, D. J. Carter, N. A. Marks, B. C. C. Cowie, L. Thomsen, J. Miwa, M. Y. Simmons, and J. W. Wells, *ACS Nano* **8**, 10223 (2014).

¹⁵P. Hofmann, C. Søndergaard, S. Agergaard, S. V. Hoffmann, J. E. Gayone, G. Zampieri, S. Lizzit, and A. Baraldi, *Phys. Rev. B* **66**, 245422 (2002).

¹⁶L. C. Davis, *Phys. Rev. B* **25**, 2912 (1982).

¹⁷L. Bawden, J. M. Riley, C. H. Kim, R. Sankar, E. J. Monkman, D. E. Shai, H. I. Wei, E. Lochock, J. W. Wells, W. Meevasana, T. K. Kim, M. Hoesch, Y. Ohtsubo, P. Le Fèvre, C. J. Fennie, K. M. Shen, F. C. Chou, and P. D. C. King, *Sci. Adv.* **1**(8), e1500495 (2015).

¹⁸C. Tablero, *Phys. Rev. B* **74**, 195203 (2006).

¹⁹C. Tablero, *J. Chem. Phys.* **123**, 114709 (2005).

²⁰J. Schrier, D. O. Demchenko, Lin-Wang, and A. P., Alivisatos, "Optical properties of ZnO/ZnS and ZnO/ZnTe heterostructures for photovoltaic applications," *Nano Lett.* **7**(8), 2377–2382 (2007).

²¹R. Nyholm, S. Svensson, J. Nordgren, and A. Flodström, *Nucl. Instrum. Methods Phys. Res., Sect. A* **246**, 267 (1986).

²²See supplementary material at <http://dx.doi.org/10.1063/1.4935536> for an alternative presentation of the raw data.

²³J. C. Fuggle and N. Mårtensson, *J. Electron Spectrosc. Relat. Phenom.* **21**, 275 (1980).

²⁴A. S. Vinogradov, S. I. Fedoseenko, S. A. Krasnikov, A. B. Preobrajenski, V. N. Sivkov, D. V. Vyalikh, S. L. Molodtsov, V. K. Adamchuk, C. Laubschat, and G. Kaindl, *Phys. Rev. B* **71**, 045127 (2005).

²⁵P. Olalde-Velasco, J. Jiménez-Mier, J. D. Denlinger, Z. Hussain, and W. L. Yang, *Phys. Rev. B* **83**, 241102 (2011).

“Graphene coatings for chemotherapy: avoiding silver-mediated degradation”

2D Mater. 2, 025004 (2015)

2D Materials



CrossMark

PAPER

Graphene coatings for chemotherapy: avoiding silver-mediated degradation

RECEIVED
22 February 2015REVISED
23 March 2015ACCEPTED FOR PUBLICATION
26 March 2015PUBLISHED
6 May 2015

Federico Mazzola¹, Thuat Trinh², Simon Cooil^{1,3}, Elise Ramleth Østli⁴, Kristin Høydalsvik^{4,5}, Eirik Torbjørn Bakken Skjønsvell¹, Signe Kjelstrup², Alexei Preobrajenski⁶, Attilio A Cafolla⁷, D Andrew Evans³, Dag W Breiby¹ and Justin W Wells¹

¹ Department of Physics, Norwegian University of Science and Technology (NTNU), NO-7491 Trondheim, Norway

² Department of Chemistry, Norwegian University of Science and Technology (NTNU), NO-7491 Trondheim, Norway

³ Department of Physics, Aberystwyth University, Aberystwyth SY23 3BZ, UK

⁴ Department of Material Science and Technology, Norwegian University of Science and Technology (NTNU), NO-7491 Trondheim, Norway

⁵ Department of Chemistry and Molecular Biology, University of Gothenburg, SE-412 96 Gothenburg, Sweden

⁶ MAX IV, Lund University, Box 118, SE-22100 Lund, Sweden

⁷ School of Physical Sciences, Dublin City University, Dublin 9, Ireland

E-mail: quantum.wells@gmail.com

Keywords: graphene, chemotherapy, fluorouracil, surface chemistry, photoemission

Supplementary material for this article is available [online](#)

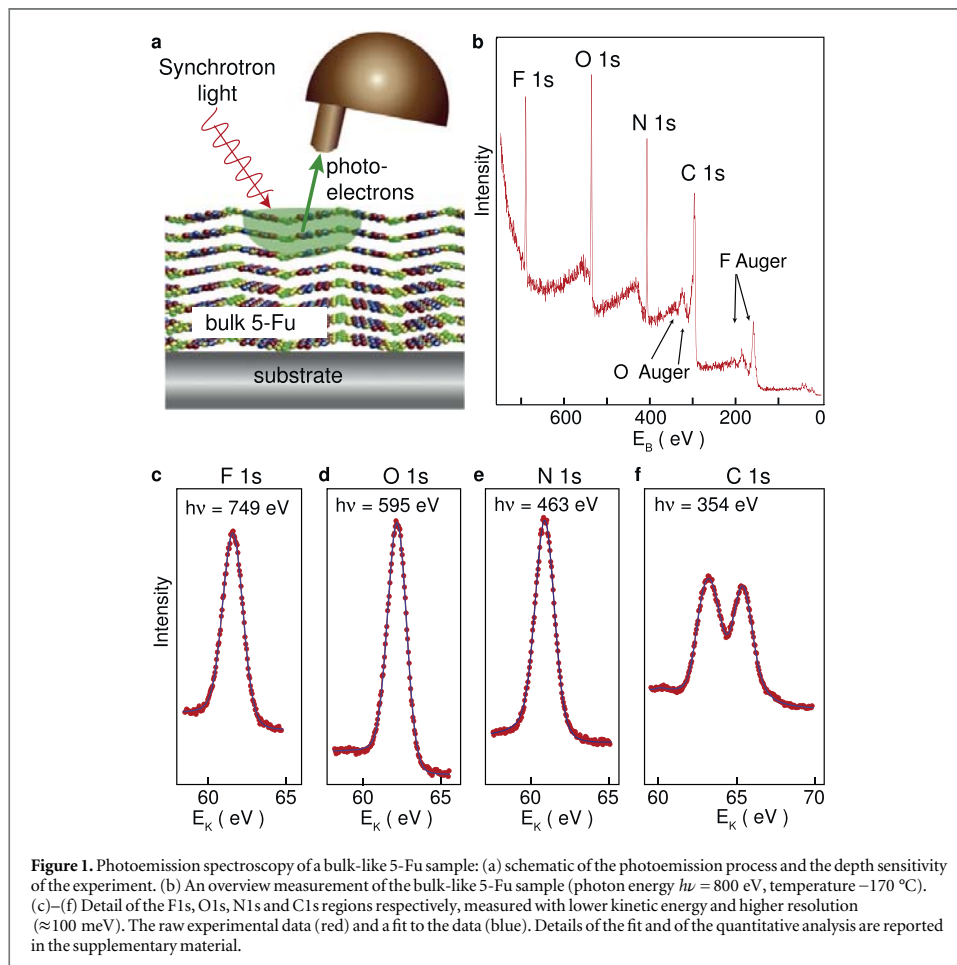
Abstract

Chemotherapy treatment usually involves the delivery of fluorouracil (5-Fu) together with other drugs through central venous catheters. Catheters and their connectors are increasingly treated with silver or argentic alloys/compounds. Complications arising from broken catheters are common, leading to additional suffering for patients and increased medical costs. Here, we uncover a likely cause of such failure through a study of the surface chemistry relevant to chemotherapy drug delivery, i.e. between 5-Fu and silver. We show that silver catalytically decomposes 5-Fu, compromising the efficacy of the chemotherapy treatment. Furthermore, HF is released as a product, which will be damaging to both patient and catheter. We demonstrate that graphene surfaces inhibit this undesirable reaction and would offer superior performance as nanoscale coatings in cancer treatment applications.

5-fluorouracil (5-Fu) is one of the most commonly used drugs in chemotherapy treatments [1–4]. 5-Fu works by inhibiting thymidine, a nucleoside required for DNA replication and necessary for cancer cells to reproduce [3]. The administration of 5-Fu into the human body is generally accomplished via a central venous catheter. Catheters are made of polymeric materials such as polyurethane and silicone [5] and they are prone to degradation when in contact with bodily fluids or aggressive drugs such as 5-Fu [6, 7]. Degradation can be reduced by applying protective coatings onto the internal and/or external surfaces of the catheters [8, 9]. Among the materials used for coating purposes, noble metals (silver and argentic alloys [10–13]) are particularly common because of their low reactivity and antimicrobial properties [14–17]. Despite the efforts made to improve the quality of the treatments of cancer and the life expectancy of the

patients, investigation of a possible chemical reaction between coating materials and the chemotherapeutic drug itself is lacking (although some studies of the electronic interaction exist, see for example [18]). In this work, we study the degradation of 5-Fu by silver surfaces, we report that HF is formed as a product, and we demonstrate graphene coatings to be an inert alternative.

Although x-ray photoemission spectroscopy (XPS) is a powerful technique for studying organic molecules (including uracil [19]), to the best of our knowledge no XPS studies of 5-Fu exist. Therefore, we first present our study of a ‘bulk-like’ 5-Fu layer. Since the depth sensitivity in an XPS experiment is limited by the mean-free-path of the photoemitted electrons (typically ≈ 1 nm), a 4 nm thick film of 5-Fu is sufficiently thick to be considered bulk-like. Indeed, our XPS study reveals that only the molecules, and not the

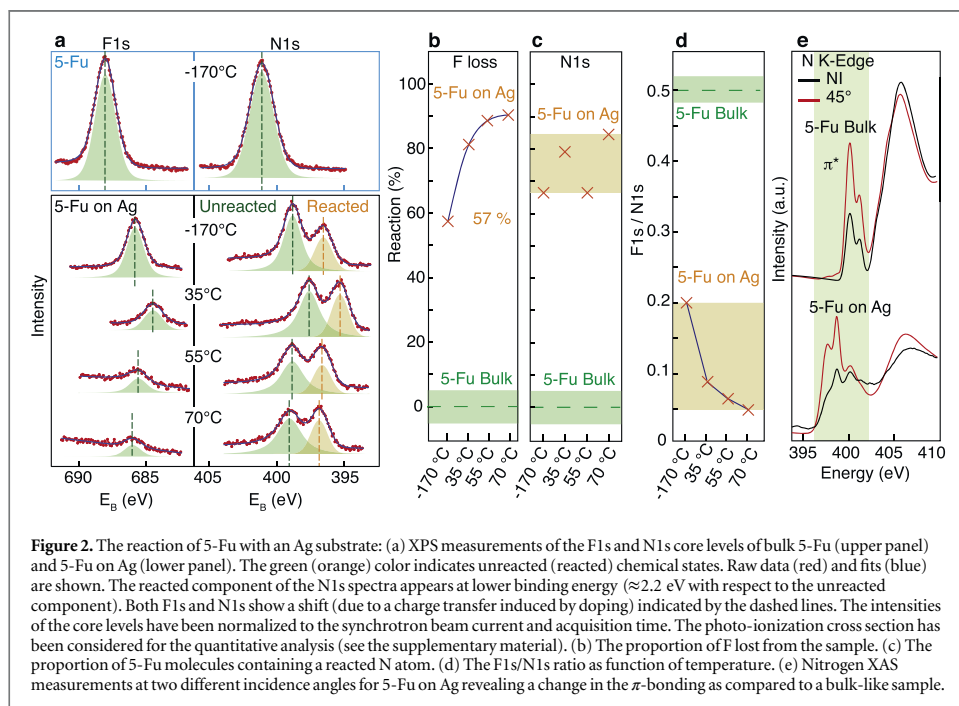


underlying substrate, contribute to the signal (the XPS technique and depth sensitivity are represented schematically in figure 1(a), and an overview XPS measurement in figure 1(b)). In our investigation of bulk-like films, we also measured the 1s core level spectra for nitrogen, fluorine, oxygen and carbon at low kinetic energy, and these results are summarized in figures 1(c)–(f).

Quantitative analysis of the XPS data allows us to confirm the stoichiometry of the molecular film. 5-Fu is composed of C, F, N and O in a ratio 4:1:2:2, and this is in good agreement with the experimentally determined abundance 4.6:1:2.2:1.8 (measured relative to F, which is defined as unity). The multiple contributions to the C1s core level signal indicate that carbon is present in multiple bonding configurations with dissimilar binding energies. Furthermore, we carried out a similar XPS study on a bulk-like film prepared from powder (i.e. not thermally evaporated in vacuum) to show that 5-Fu is not damaged by evaporation (see supplementary material).

A thin film (≈ 0.7 nm) film of 5-Fu was also prepared on an Ag substrate. XPS measurements (figure 2(a)) reveal that a reaction takes place at body temperature (≈ 35 °C). Measurements were also performed at lower temperatures in order to reduce the thermal energy available (i.e. to facilitate observation of the intermediate steps of the reaction and their approximate energy budget).

Our study reveals that already at -170 °C the N1s core level undergoes a significant change from its bulk form, indicating a change in the N bonding configuration. A new ‘reacted’ N1s core level component is observed at larger binding energy, shifted 2.2 eV from the unreacted component. We propose that the reaction involves breaking one of the N–H bonds with a subsequent H loss from the molecule. Assuming that only one N-atom per molecule is able to react, quantitative analysis of the N1s components indicates that $\approx 80\%$ of the molecules are in the reacted form (figure 2(c)). The reaction is already favourable at the lowest temperature studied (-170 °C), and thus



increasing the temperature is not seen to play a significant role.

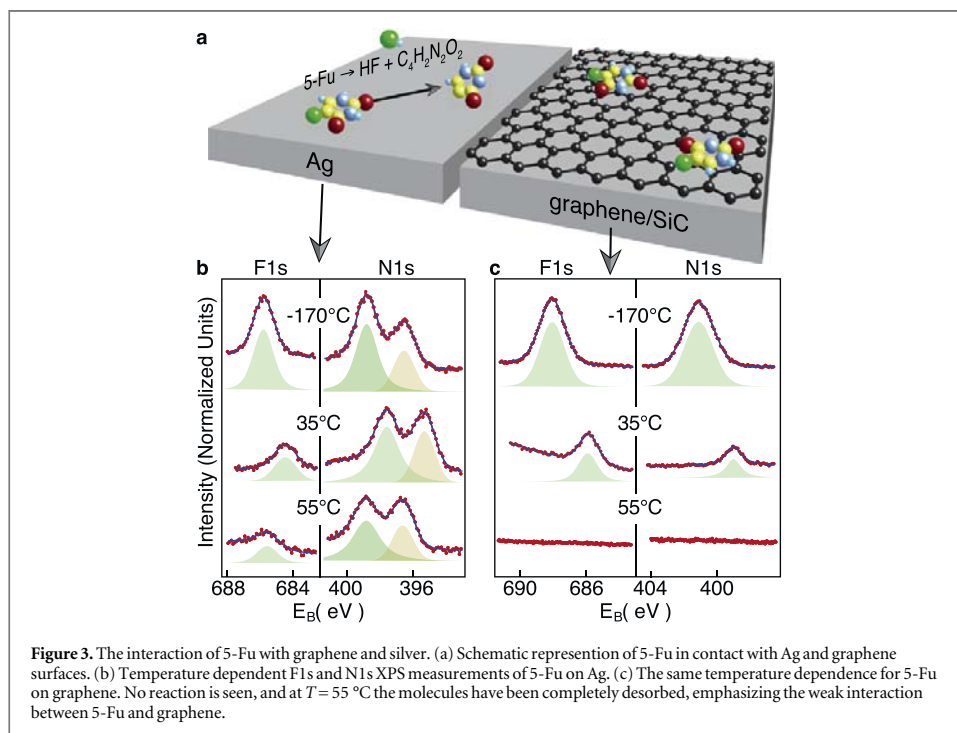
Analysis of the F1s peak also reveals that a reaction is taking place—seen as a relative reduction of the F1s intensity, indicating that fluorine is lost from the surface. The fluorine reduction shows a strong temperature dependence (figure 2(b)); at low temperature, the loss is $\approx 57\%$ (relative to the bulk-like film), and as the temperature is increased to body temperature and above, the loss is almost complete ($\approx 90\%$). The same behavior can also be observed by extracting the F1s/N1s intensity ratio ($=0.5$ for bulk 5-Fu) which is reduced to ≈ 0 as the temperature is increased (figure 2(d)).

Although the N1s and F1s peaks show signs of a reaction, the only modification to the O1s and C1s peaks (see the supplementary material for details) is an energy shift which is similarly affects all of the thin film's core levels. We therefore conclude that the O and C-atoms are not involved in the reaction. The ubiquitous core level shift to lower binding energy (relative to the bulk film) is exhibited by all of the core levels, due to the *p*-type doping nature of the 5-Fu molecules and reaction fragments. The detail of the charge transfer between substrate and molecules is the subject of further study, however, the general principle that strongly *p*-type halogenated species cause a electronic re-alignment of the interface is not unusual [20]

Summarizing the XPS measurements, we observe that 5-Fu in contact with Ag gives rise to reactions which modify the bonding of one of the N-atoms in

the 5-Fu molecule, and involves a massive F loss under vacuum conditions. We present a plausible reaction which is consistent with these observations $5\text{-Fu} \rightarrow \text{HF} + \text{C}_4\text{H}_2\text{N}_2\text{O}_2$. Where the a modification of an N-atom occurs, and is already favourable with minimal thermal energy (i.e. at low temperature), the loss of F requires a moderate energy budget—indicative of a reaction where the mobility of the atomic species on the silver surface plays a role. At body temperature both of these reactions are favourable and the vast majority of the molecules are seen to have reacted.

X-ray absorption spectroscopy (XAS) measurements of 5-Fu on Ag also support the notion of a change in the molecular π -bonding configuration of the molecule (figure 2(e)). Compared to the bulk-like sample, 5-Fu on Ag shows additional features at lower photon energies, in the energy range corresponding to a transition from the N1s core level to an unoccupied π^* orbital (indicated by the green area in figure 2(e)). This result suggests that the π -bonding of an N-atom has been significantly modified, but that a delocalized π state still remains. This view is consistent with the XPS inference of a silver-mediated reaction involving the breaking of an N–H bond. For both the bulk film and 5-Fu on Ag, the π^* absorption features are reduced at normal incidence relative to the measurement at 45° incidence, indicating that the molecules have a preference to lie flat on the substrate. For the bulk film, the molecular orientation can be rationalized using the bulk crystal structure. For the thin film 5-Fu on Ag, the molecular orientation is consistent with the



orientation expected for the reacted species, and with STM observations (see the supplementary material for the bulk crystal structure and STM measurements).

The reaction observed on the Ag surface is not seen on graphene. Graphene is chosen because we expect it to be chemically inert, and because it already attracts attention as the ultimately thin protective coating [21–23]. However, its potential as a nanoscale coating material in chemotherapeutic drug delivery systems appears to have been entirely overlooked [24]. Graphene is a bio-compatible material [25, 26] with low toxicity. The accidental release of small quantities of a graphene coating into a patient is less concerning than a similar release of alternative coating materials.

A thin film (≈ 0.7 nm) of 5-Fu on graphene was prepared by thermal evaporation, following the same procedure as above. i.e., the only difference with the experiment of 5-Fu on Ag is that a graphene substrate is used in place of Ag. Temperature dependent XPS data have also been acquired (figure 3(c)) and compared with that from 5-Fu on Ag (figure 3(b)). Contrary to 5-Fu on Ag, the chemotherapy molecules on graphene do not react at any temperature; instead they are simply desorbed at moderate temperatures. This observation supports the idea of a weak interaction between graphene and 5-Fu since already at $\approx 55^\circ\text{C}$ the intact 5-Fu molecules have left the surface and no N or F can be detected by XPS.

DFT structural optimization calculations have also been performed with results which support our

experimental findings. Figure 4 shows four of the steps of the suggested 5-Fu+Ag reaction pathway. The first step (i) involves the absorption of the molecule onto the Ag(111) surface; it is seen to be weakly physisorbed, and the total energy is lowered by ≈ 1 eV. In step (ii), the C–F bond and a C–H bond are broken, resulting in a small increase in the total energy which is feasible even at low temperature. H and F are liberated from the molecule and stay bound to the Ag surface. In steps (iii) and (iv), reaction product is stabilised by a redistribution of both chemical bonding and charge transfer and the remaining H-atoms of molecule fragment rearrange, with negligible change in the energy. Finally, in step (v) (not shown), H and F recombine and an HF molecule is desorbed from the surface. This last step requires a moderate input of energy, which is consistent with the measured temperature dependence.

To summarize the DFT calculation reaction pathway, the molecules react at low temperature and the bonding in the vicinity of one N-atom is modified with the macrocycle remaining intact. Although H and F are already ‘lost’ from the 5-Fu molecule, the HF recombination and liberation from the surface cannot occur without a moderate amount of thermal energy. In agreement with the observation of HF in our residual gas analysis, these calculations support that HF, rather than F_2 , is the favoured product (see the supplementary material for details of the residual gas analysis and the calculated energetics of the F_2 formation).

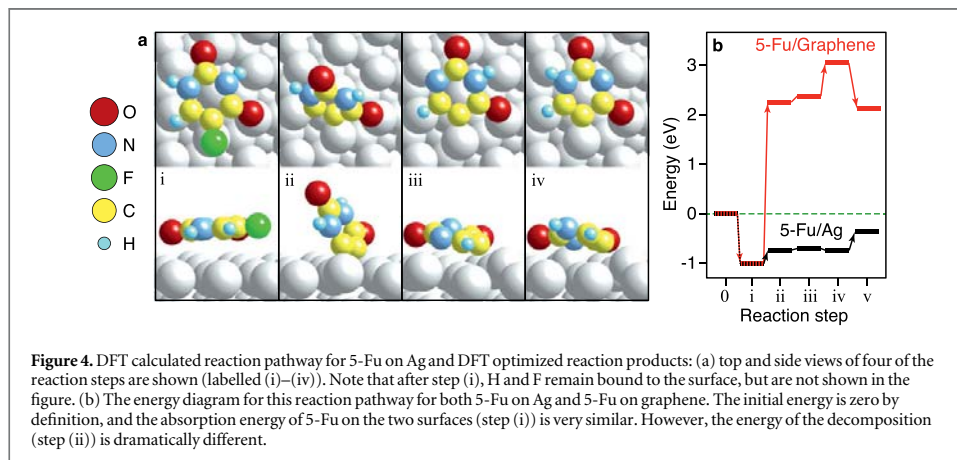


Figure 4. DFT calculated reaction pathway for 5-Fu on Ag and DFT optimized reaction products: (a) top and side views of four of the reaction steps are shown (labelled (i)–(iv)). Note that after step (i), H and F remain bound to the surface, but are not shown in the figure. (b) The energy diagram for this reaction pathway for both 5-Fu on Ag and 5-Fu on graphene. The initial energy is zero by definition, and the absorption energy of 5-Fu on the two surfaces (step (i)) is very similar. However, the energy of the decomposition (step (ii)) is dramatically different.

An identical reaction pathway has been calculated for 5-Fu on graphene (see figure 4(b)). Contrary to the situation for Ag, step (ii) requires a large energy input (≈ 3 eV), which is prohibitive. In fact, the required energy is much larger than the absorption energy (step (i)), hence as the thermal energy is increased, the intact molecule would desorb well before it has the possibility to decompose. Unlike Ag, graphene is not able to stabilise the reaction by a redistribution of chemical bonds and charge transfer (i.e. compare the energy of steps (ii)–(iv) for the two surfaces).

The DFT calculations also support that the molecules have a tendency to lie flat on both the Ag and graphene substrate (which is unsurprising since molecules with conjugated π -systems typically show this tendency [27, 28]). The calculated orientation is consistent with the orientation observed with XAS and STM. Finally, the DFT calculation gives access to the binding energy of the reaction species; the two inequivalent N-atoms in the reacted molecular fragments have N1s components separated by 1.7 eV (compared to a calculated N1s separation of 0.4 eV for unreacted 5-Fu), this is in good agreement with the experimentally determined value of 2.2 eV.

At temperatures in excess of 70 °C, the molecule fragments are observed to desorb from the Ag surface. Since the Ag surface plays a role in stabilizing the reaction product, it is unclear whether further reaction steps occur after desorption. The low energy barrier for redistributing the molecular fragment's remaining H-atoms indicates that such a redistribution is possible.

Using surface chemistry techniques in combination with DFT calculations, we observed that a reaction takes place for 5-Fu on silver which does not occur for 5-Fu on graphene. Our experiments have been performed on model surfaces in a well controlled ultrahigh vacuum environment ($P \leq 10^{-9}$ mbar). Although the experimental conditions necessarily differ from *in operando* drug delivery (most notably, the lack of ionic solution), it is of concern that an

energetically favourable reaction exists in which 5-Fu is decomposed by Ag with HF as a product—especially when this reaction is readily avoided by choosing a more suitable coating material.

We conclude that silver and argentic alloys are not a good choice for catheters delivering 5-Fu. Catheter degradation is a common problem, and our measurements indicate a likely cause; the catalytic degradation of 5-Fu by silver with HF as a product. We speculate that the presence of HF in the drug solution accounts, at least partially, for the prevalent degradation of catheters and their coatings. Such a reaction occurring in a real catheter would not only compromise the efficacy of the treatment, but also create concerns that Ag and HF are assimilated into the bloodstream of a patient [29, 30].

Since the potential effects of 5-Fu degradation are so significant, it is surprising that studies of the relevant catheter surface chemistry do not appear to have been carried out, and we believe that our study represents an important first step in exploiting established surface science methods in this field. Our study demonstrates that surface chemistry approaches are well suited to study the interaction of chemotherapeutic drugs on relevant surfaces.

Graphene has already been suggested as an external coating for bio-medical applications, and based on our findings, we propose to use graphene also for the internal surfaces. The fabrication of thin carbon-based coatings is technologically realistic [31–33]; graphene can even be grown directly on top of silver [34, 35], if desired, to maintain compliance with existing fabrication methods. We believe that graphene coatings will offer a vastly superior alternative to silver-based coatings, and can return a societal benefit within a short timescale.

Methods

The 'powder' sample was prepared by dissolving 5-Fu powder (>99%, Sigma-Aldrich, F6627-5G) in de-

ionized water, followed by dripping the solution onto a tantalum sample plate and allowing it to dry under atmospheric conditions. After drying, a thick white powder layer was observed.

All other 5-Fu films were made by thermal evaporation under ultra-high vacuum (UHV) conditions. The same 5-Fu powder was placed in a tantalum crucible and heated in-vacuum until it evaporated. The substrate was held in front of the crucible and exposed to the molecular flux.

Prototype graphene samples were fabricated using standard CVD instrumentation in NTNU NanoLab. The high quality graphene sample was thermally grown on SiC with standard methods described in our previous work [36]. The Ag sample was a (111) single crystal which had been prepared in vacuum by cycles of sputtering and annealing.

Photoemission measurements were carried out at beamline D1011 at the MAX IV laboratory (Lund, Sweden). The thermally evaporated films were grown at the beamline and measured without exposure to air.

Samples were prepared for STM analysis by similar thermal evaporation in UHV.

Calculations were performed using quantum espresso [37]. We employed the generalized gradient approximation method PBE functional [38] with Van der Waals correction [39] using an ultra soft pseudo-potential [40]. Satisfactory convergences were obtained with cutoffs of 70 Ry on the plane waves and 700 Ry on the electronic density. These conditions were checked to get a convergence of properties and lattice parameter of Ag bulk of 4.15 Å (experimental value 4.09 Å) [41]. We used the Γ point for the k -point sampling of the Brillouin zone.

Acknowledgments

The synchrotron access was partially funded under the 'CALIPSO' scheme. FM and ETBS acknowledge travel support from the Norwegian PhD Network on Nanotechnology for Microsystems, sponsored by the Research Council of Norway (contract no. 221860/F40). The calculation power is granted by The Norwegian Metacenter for Computational Science (NOTUR), project numbers: nn9229k and nn4504k.

References

- [1] Lu Z, Zhang R and Diasio R B 1993 *Cancer Res.* **53** 5433
- [2] Sistigu A et al 2014 *Nat. Med.* **20** 1301
- [3] Longley D, Harkin D and Johnston P 2003 *Nat. Rev. Cancer* **3** 338
- [4] Levine M N et al 1998 *J. Clin. Oncol.* **16** 2651
- [5] O'Leary R and Bodenham A 2011 *Eur. J. Anaesthesiol.* **28** 327
- [6] Fackler Schwalbe I, Schwalbe B, Eppe M, Becker A, Prügl L, Gassel W, Stoffels D and Südhoff T 2004 *Wiener Medizinische Wochenschrift* **154** 182–85
- [7] Ardalán B and Flores M 1995 *Cancer* **75** 2165
- [8] O'Grady N P et al 2011 *Clin. Infectious Diseases* **52** e162
- [9] Masci G, Magagnoli M, Zucali P, Castagna L, Carnaghi C, Sarina B, Pedicini V, Fallini M and Santoro A 2003 *J. Clin. Oncol.* **21** 736
- [10] Timsit J-F, Dubois Y, Minet C, Bonadona A, Lugosi M, Ara-Somohano C, Hamidfar-Roy R and Schwebel C 2011 *Ann. Intensive Care* **1** 34
- [11] Armentano I, Arciola C R, Fortunati E, Ferrari D, Mattioli S, Amoroso C F, Rizzo J, Kenny J M, Imbriani M and Visai L 2014 *Sci. World J.* **2014** 18
- [12] Suska F, Svensson S, Johansson A, Emanuelsson L, Karlholm H, Ohrlander M and Thomsen P 2010 *J. Biomed. Mater. Res. B: Appl. Biomater.* **92B** 86
- [13] Harter C, Salwender H, Bach A, Egere G, Goldschmidt H and Ho A 2002 *Cancer* **94** 245
- [14] Maki D, Stolz S, Wheeler S and Mermel L A 1997 *Ann. Intern. Med.* **127** 257
- [15] Singh R, Kumar D, Kumar P and Chacharkar M 2008 *J. Burn Care Res.* **29** 64
- [16] Guggenbichler J, Boswald M, Lugauer S and Krall T 1999 *Infection* **27** S16
- [17] Feng Q L, Wu J, Chen G Q, Cui F Z, Kim T N and Kim T O 2000 *J. Biomed. Mater. Res. A* **52** 662–8
- [18] Feng Q L, Wu J, Chen G Q, Cui F Z, Kim T N and Kim T O 2000 *J. Biomed. Mater. Res. A* **52** 662
- [19] Pavel I, Cota S, Kiefer W and Cintă-Pințaru S 2006 *Particulate Sci. Technol.* **24** 301
- [20] Papageorgiou A C, Fischer S, Reichert J, Diller K, Blobner F, Klappenberger F, Allegretti F, Seitsonen A P and Barth J V 2012 *ACS Nano* **6** 2477
- [21] Vinogradov N A, Simonov K A, AZakharov A, Wells J W, Generalov A V, Vinogradov A S, Mårtensson N and Preobrajenski A B 2013 *Appl. Phys. Lett.* **102** 061601
- [22] Prasad I, Tuberquia J C, Harl R R, Jennings G K and Bolotin K I 2012 *ACS Nano* **6** 1102
- [23] Nilsson L, Andersen M, Balog R, Laegsgaard E, Hofmann P, Besenbacher F, Hammer B, Stensgaard I and Hornekaer L 2012 *ACS Nano* **6** 10258
- [24] Kirkland N T, Schiller T, Medhekar N and Birbilis N 2012 *Corros. Sci.* **56** 1
- [25] Dolgin E 2010 What the physics Nobel means to biomedicine *Nat. Med.* Odds and Ends
- [26] Gurunathan S, Han J W, Eppakayala V, Dayem A A, Kwon N D and Kim J H 2013 *Nanoscale Res. Lett.* **8** 393
- [27] Fan H, Wang L, Zhao K, Li N, Shi Z, Ge Z and Jin Z 2010 *Biomacromolecules* **11** 2345
- [28] Song F et al 2009 *Nat. Nanotechnol.* **4** 373
- [29] Yamane H, Yoshimura D, Kawabe E, Sumii R, Kanai K, Ouchi Y, Ueno N and Seki K 2007 *Phys. Rev. B* **76** 165436
- [30] Yamashita M, Suzuki M, Hirai H and Kajigaya H 2001 *Crit. Care Med.* **29** 1575
- [31] Fung M and Bowen D 1996 *J. Toxicol. Clin. Toxicol.* **34** 119
- [32] Podila R, Moore T, Alexis F and Rao A M 2013 *R. Soc. Chem. Adv.* **3** 1660
- [33] Bunch J S, Verbridge S S, Alden J S, van der Zande A M, Parpia J M, Craighead H G and McEuen P L 2008 *Nano Lett.* **8** 2458
- [34] Zhang W et al 2014 *Sci. Rep.* **4** 4097
- [35] Cai J et al 2010 *Nature* **466** 470
- [36] Kiraly B, Iski E V, Mannix A J, Fisher B L, Hersam M C and Guisinger N P 2013 *Nat. Commun.* **4** 2804
- [37] Mazzola F et al 2013 *Phys. Rev. Lett.* **111** 216806
- [38] Giannozzi P et al 2009 *J. Phys.: Condens. Matter.* **21** 395502
- [39] Perdew J P, Burke K and Ernzerhof M 1996 *Phys. Rev. Lett.* **77** 3865
- [40] Grimme S 2006 *J. Comput. Chem.* **27** 1787
- [41] Rappe A M, Rabe K M, Kaxiras E and Joannopoulos J D 1990 *Phys. Rev. B* **41** 1227
- [42] Linstrom P and Mallard W (ed) 2001 *NIST Chemistry WebBook, NIST Standard Reference Database Number 69 vol 20899* (Gaithersburg MD: National Institute of Standards and Technology)

“Valley Splitting in a Silicon Quantum Device Platform”

Nano Lett., 14 (3), pp 1515{1519} (2014)

Valley Splitting in a Silicon Quantum Device Platform

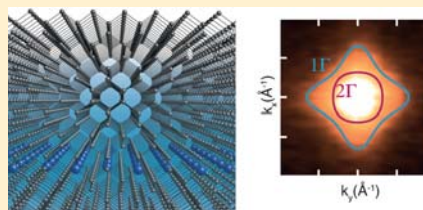
Jill A. Miwa,[†] Oliver Warschkow,[‡] Damien J. Carter,[§] Nigel A. Marks,[§] Federico Mazzola,^{||} Michelle Y. Simmons,[⊥] and Justin W. Wells^{*,||}[†]Department of Physics and Astronomy, Interdisciplinary Nanoscience Center (iNANO), University of Aarhus, 8000 Aarhus C, Denmark[‡]Centre for Quantum Computation and Communication Technology, School of Physics, The University of Sydney, Sydney, NSW 2006, Australia[§]Nanochemistry Research Institute, Curtin University, P.O. Box U1987, Perth WA 6845^{||}Department of Physics, Norwegian University of Science and Technology (NTNU), N-7491 Trondheim, Norway[⊥]Centre of Excellence for Quantum Computation and Communication Technology, School of Physics, University of New South Wales, Sydney, NSW 2052, Australia

Supporting Information

ABSTRACT: By suppressing an undesirable surface Umklapp process, it is possible to resolve the two most occupied states (1Γ and 2Γ) in a buried two-dimensional electron gas (2DEG) in silicon. The 2DEG exists because of an atomically sharp profile of phosphorus dopants which have been formed beneath the Si(001) surface (a δ -layer). The energy separation, or valley splitting, of the two most occupied bands has critical implications for the properties of δ -layer derived devices, yet until now, has not been directly measurable. Density functional theory (DFT) allows the 2DEG band structure to be calculated, but without experimental verification the size of the valley splitting has been unclear.

Using a combination of direct spectroscopic measurements and DFT we show that the measured band structure is in good qualitative agreement with calculations and reveal a valley splitting of 132 ± 5 meV. We also report the effective mass and occupation of the 2DEG states and compare the dispersions and Fermi surface with DFT.

KEYWORDS: δ -layer, quantum computer, valley-splitting, ARPES, Umklapp, silicon



Quantum devices, such as gated quantum dots, have been fabricated successfully by numerous means, and have advanced to the ultimate limit where individual atoms dictate device behavior.^{1–3} A method that has shown steady progress in recent years utilizes phosphorus δ -doped Si(001) as the foundation from which devices are derived.^{3–6} A common prediction for such δ -doped layers is the formation of confined states derived from the bulk conduction band minima.⁷ The lowest lying states, called 1Γ and 2Γ are nondegenerate and their separation energy, that is, valley splitting, facilitates an alternative approach to performing operations in quantum electronic devices^{8–10} and hence attracts much interest.^{4,11,12} The magnitude of the valley splitting has implications for critical device properties, such as decoherence and transport. Because a direct measure has hitherto not been possible, a reliance on various calculations, offering values from 6 to 270 meV,^{13–19} has been necessary. Here we demonstrate an experimental approach involving removal of a surface Umklapp processes that otherwise obfuscate these states, such that a valley splitting of 132 ± 5 meV is directly measured.

When an electron is photoemitted from a solid, the surface Umklapp process is one of the few mechanisms that allows the exchange of parallel momentum, and hence parallel momentum is otherwise conserved.²⁰ The surface Umklapp process allows

integer multiples of the surface reciprocal lattice momentum to be exchanged between a surface and a photoemitted electron, thus, regardless whether an electron originates from a bulk, surface or δ -layer state, periodicities corresponding to the surface reciprocal lattice are not only to be expected but have already been observed.²¹ Here, we present measurements on two samples, identical except for their surface reconstructions, thus allowing the surface momentum exchange to be disentangled, and the valley splitting and band dispersions to be accessible for the first time.

We have recently demonstrated that despite the assumed short mean free path of low kinetic energy photoelectrons, it is nonetheless possible to probe the bandstructure of buried two-dimensional layers using angle-resolved photoemission spectroscopy (ARPES).²¹ The photoemission intensity from the buried states is resonantly enhanced such that the small fraction of its wave function, which exists near the surface, is strong enough to be directly measured.²² This enhancement occurs at photon energies corresponding to electron emission at bulk

Received: December 20, 2013

Revised: February 21, 2014

Published: February 26, 2014

high symmetry points.^{20,23} However, since the surface is known to be (2×1) reconstructed with an equivalent (1×2) rotational domain giving the appearance of (2×2) , it was previously not possible to conclude whether the observed $2 \times$ periodicity (see Figure 1a) originates in the buried layer, or is

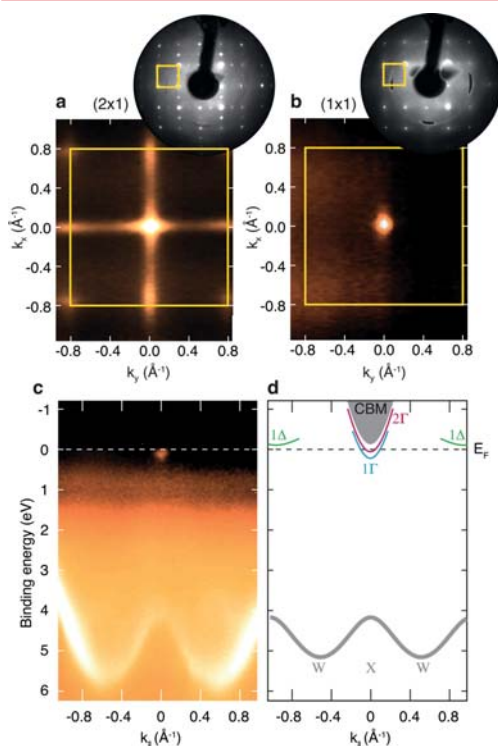


Figure 1. Direct comparison of the δ -doped Si(001)- (2×1) and δ -doped Si(001)- (1×1) samples. Overview ARPES measurements, taken at $h\nu = 113$ eV, showing the constant energy surface at the Fermi level for an extended region of $k_{||}$, and corresponding LEED patterns collected at $E_k = 250$ eV (insets) for exemplary (a) δ -doped Si(001)- (2×1) and (b) δ -doped Si(001)- (1×1) samples. The yellow squares overlaid indicate the surface (1×1) unit cell, and serve as a reference. (c) ARPES measurement made in the bulk $\langle 100 \rangle$ direction with a photon energy of $h\nu = 113$ eV is shown for the (1×1) case. The δ -layer states appear as a small bright feature located near the Fermi level. (d) Schematic illustration indicating the position of the δ -layer states with respect to the bulk Si bands based on DFT (combining details of Supporting Information Figures S1b and S2b²⁴).

rather a result of the surface Umklapp process. Furthermore, step edges are inclined toward either the $\langle 1\bar{1}0 \rangle$ or $\langle 110 \rangle$ axes thus giving rise to the observed one-dimensional streaking that further obfuscates the measurement and frustrates the direct measurement of the valley splitting and band dispersions.

δ -doped Si(001) samples are made in situ with a typical (2×1) reconstructed surface and the following measurements are treated to alter the surface termination²² to (1×1) , as confirmed by the low energy electron diffraction (LEED) images in the insets of Figure 1a,b. Because the two alternate preparations change only the surface periodicity, the appear-

ance of the bulk and δ -layer bandstructures are essentially unchanged, except for the manifestations of the surface Umklapp process.²⁴ The electronic states at the Fermi level (E_F), due to the buried δ -layer, are seen to be affected by the surface Umklapp process; for the (1×1) surface, the constant energy map collected at the E_F shows a feature around $k_x = k_y = 0$ only (Figure 1b), whereas the (2×1) surface (Figure 1a), shows additional repetitions of the state at $k_x = \pm 0.8 \text{ \AA}^{-1}$ and $k_y = \pm 0.8 \text{ \AA}^{-1}$, corresponding to the $2 \times$ surface reciprocal lattice vector. Thus there is no evidence of long-range ordering in the δ -layer itself, because the periodic features are associated with the surface Umklapp process and not the δ -layer.

Once the additional Umklapp features have been removed, the electronic structure of the δ -layer state can be seen more clearly. ARPES measurements acquired in the bulk $\langle 100 \rangle$ direction with a photon energy of $h\nu = 113$ eV are shown in Figure 1c and provide an overview of the position of the δ -layer state, which appears as a small bright feature near the Fermi level, with respect to the Si bulk bands. A corresponding schematic (based on density functional theory (DFT) calculations) is given in Figure 1d with both the δ -layer states, (i.e., 1Γ , 2Γ , and 1Δ) and Si bulk bands marked. Detailed ARPES measurements in the same direction, but performed at a temperature of 90 K and photon energy $h\nu = 36$ eV, reveal that the δ -layer spectral feature has the appearance of a filled parabola (Figure 2a). In fact, this feature can be fully described by the presence of two parabolic states, separated in binding energy. This is exemplified in Figure 2b,c for a vertical (i.e.,

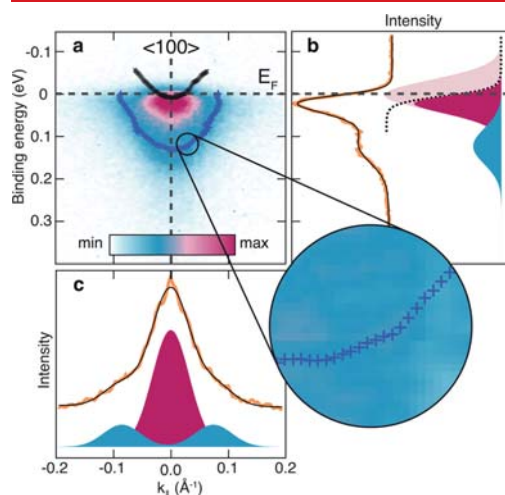


Figure 2. Detail of the δ -layer state of the δ -doped Si(001)- (1×1) sample. (a) Low-temperature (90 K) false-color ARPES measurements, taken at $h\nu = 36$ eV, of the δ -layer states with the fitted positions of the components overlaid (black \times and blue $+$). Detail of the individual fitted points relative to the parabolic trend is shown as an inset. Note that the small modulations in the positions of fitted peak positions arise from intensity variations in the detector. (b) A constant momentum slice (orange), extracted at $k_y = 0$ fitted with two Gaussian components modified by a Fermi function (black dashed line). (c) A constant energy slice (orange) extracted at the Fermi level together with three Gaussian components. Overall fits are represented by the black lines.

constant momentum) and horizontal (constant energy) slice through the ARPES data, respectively. Fitting the photoemission intensity of these slices confirms that two states (colored magenta and blue) are contributing to the total intensity. A similar component analysis was conducted for every possible horizontal and vertical slice of the ARPES data,²² and the fitted peak positions are plotted atop the measurement in Figure 2a. Although the intensity is seen to drop dramatically at the Fermi level, a small thermal occupancy gives sufficient intensity for constant momentum slices up to ~ 50 meV above E_F to be useful. Because of the large number of slices analyzed, the individual peak positions rather appear as thick lines in the figure, but the enlargement of a small region of the deeper binding energy state (Figure 2, inset) clarifies that these “thick lines” in fact consist of many discrete peak positions.

The presence of two states is not surprising because strong confinement perpendicular to the δ -layer state is predicted to give rise to two valley-split states, 1Γ and 2Γ around the Brillouin zone center.^{7,13–19} The peak positions describing the two measured states are well approximated by parabolas (as shown in Figure 3a) with effective masses of $0.21 m_e$. This is

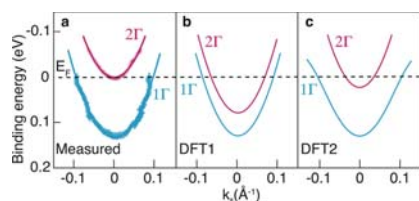


Figure 3. Identifying 1Γ and 2Γ . (a) The fitted peak positions (magenta \times and blue $+$) from Figure 2a with parabolic fits for the two measured states (magenta and blue fine curves). (b,c) The DFT calculated 1Γ and 2Γ band minima for the same energy and momentum range probed in the experiment for two different dopant arrangements.²² The calculated band structures are aligned in energy such that the 1Γ band minima match that of the experiment. The dashed horizontal line in all three panels corresponds to the experimental Fermi level.

close to the transverse effective mass of the bulk conduction band minimum ($0.19 m_e$) from which the 1Γ and 2Γ states are derived.^{4,7,15} Alongside the experimental data, DFT calculations²² are shown (Figure 3b,c), which illustrate the similarities between the two measured states and those predicted by theory. Therefore the measured state at larger binding energy and the measured state nearer to E_F can be confidently assigned to the 1Γ and 2Γ states of the δ -layer, respectively. We note that the measured 2Γ state barely grazes the Fermi level, which suggests that this state plays a role in Fermi level pinning.

The energy separation of the 1Γ and 2Γ minima, that is, the valley splitting, is measured to be 132 ± 5 meV whereas the DFT calculations in Figure 3b,c reveal valley splittings of 51 and 106 meV, respectively, depending on the dopant arrangement. The experimentally determined value is centrally placed within the range of reported calculated values; 6 to 270 meV.^{13–19} This wide range of values arises because the calculated valley splitting is sensitive to the arrangement of dopants in the δ -layer,^{14,17} as well as to other physical parameters such as dopant density, the confinement potential (related to dopant segregation), and to the particular

calculational approach used. The preparation recipe used here is known to reliably produce a dense ($2.4 \times 10^{14} \text{ cm}^{-2}$) and narrow (<1 nm wide) dopant profile^{25,26} that can be well represented in the calculations. The lack of periodicity in the δ -layer states, after removing the surface Umklapp process (Figure 1b), supports the notion of a dopant layer that lacks long-range order, but does not exclude the likely possibility of local ordering.^{14,17} We therefore primarily attribute the discrepancy between the measured and calculated valley splitting values to an ill-defined dopant arrangement in the δ -layer.

Even though DFT calculations do not reproduce the magnitude of the measured valley splitting, all other aspects of the data are well matched by DFT. The measured Fermi surface (Figure 4a) together with the DFT Fermi contours

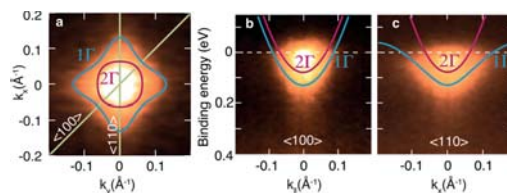


Figure 4. Direct comparison of measurement and calculation. (a) The measured Fermi surface with the calculated “DFT1” Fermi contours overlaid. Corresponding ARPES measurements collected with $h\nu = 36$ eV for (b) the $\langle 100 \rangle$ and (c) the $\langle 110 \rangle$ high symmetry directions with the same calculations overlaid. Note that the calculations have been shifted in energy such that the 1Γ band minimum matches the experimental data.

reveal that the rotated-square appearance of the Fermi surface is well replicated by the calculated 1Γ contour. The rotated square shape arises from the inequivalent dispersions in the $\langle 100 \rangle$ and $\langle 110 \rangle$ directions, as illustrated respectively in Figure 4b,c. The dispersion of the calculated 1Γ state is in good agreement with the experimental data.

Finally, there are other practical differences which cannot be readily incorporated into the calculations; the shallowness of the δ -layer necessary for this study means that an interaction with the surface is possible. Indeed, conductivity measurements indicate that the surface proximity plays a role.²⁷ The intrinsic bulk assumed in the calculations is idealistic and, together with the surface interaction, could act to modify the band bending in the vicinity of the δ -layer. Because the sharpness of the confining potential determines the valley splitting, such shortcomings in the calculations can be important, and highlight the need for experimental verification of the valley splitting. Introducing dopant segregation acts to broaden the confining potential, thus producing smaller valley splitting values. The large valley splitting measured here indicates that the fabricated δ -layer is in fact highly confined and that dopant segregation is minimal.

To conclude, through the combination of resonantly enhanced ARPES and disentanglement of the surface Umklapp process we have been able to reveal the band structure of a δ -layer with unprecedented clarity. This reveals the Fermi level position, and hence the occupancy, effective masses, and valley splitting of the 1Γ and 2Γ bands that are essential properties for understanding δ -layers and their use in atomic-scale devices.

Methods. *δ -Doped Si(001) Sample Preparation.* δ -doped Si(001) samples are made in situ by first preparing a clean

Si(001) sample, followed by deposition of one-fourth of a monolayer of phosphorus dopants (from phosphine gas). Samples are then annealed to nominally 350 °C to incorporate the dopants and ~2 nm of epitaxial silicon is subsequently overgrown by thermally evaporating silicon. The samples undergo a final anneal to 500 ± 25 °C to remove crystalline imperfections in the silicon overlayer yielding a clean (2×1) reconstructed surface. The silicon (1×1) surface is prepared by exposure to atomic hydrogen with the substrate held at room temperature, followed by *in vacuo* annealing to 500 ± 25 °C to desorb the hydrogen but without reconstruction of the surface²⁸ or considerable dopant segregation. Core level spectroscopy measurements confirmed minimal phosphorus dopant segregation for all anneal steps during sample preparation. Numerous samples were prepared and measured multiple times; the 1Γ minimum was always observed to be ~100–140 meV below the Fermi level, and the 2Γ minimum, if observable, within a few meV of the Fermi level or above it.

Probing δ -Doped Si(001) by ARPES. ARPES measurements of the δ -layer state are only possible because of a strongly enhanced photoemission intensity that occurs when the momentum of an electron from a 2D initial-state is well matched to that of a bulk-like final state into which it can be photoexcited.^{20,23} We have previously measured that the strongest enhancements occur for photon energies of 36 and 113 eV²¹ thus only ARPES measurements acquired at these photon energies are presented in this letter.

Fitting the Constant Energy and Constant Momentum Slices through the δ -Layer State. The constant momentum slice at $k_{\parallel} = 0$ (Figure 2b), and the constant energy slice at E_F (Figure 2c) are composed of multiple components (blue and magenta), and hence fits made up of multiple Voigt functions (black lines) are required in order to satisfactorily replicate the raw data (orange). Constant momentum slices are attenuated above the E_F by a Fermi function (black dotted line). We note that the Lorentzian component is negligible and therefore the Voigt function is well approximated by just the Gaussian component.

Details of the DFT Calculations for the δ -Layers. The two occupied δ -layer states (Figure 3) can be identified by DFT using the SIESTA code²⁹ and methods described in ref 17. The δ -layer is represented using an elongated three-dimensional unit cell, a double-numerical-plus-polarization (DNP) atom-centered basis set, and the generalized-gradient approximation (GGA).³⁰ In the direction normal to the dopant plane, the δ -layer is separated from its periodic images by 40 atomic layers, which affords an adequate degree of electronic separation. In the in-plane direction a (4×4) unit cell of 16 atoms (with 4 P and 12 Si in the δ -layer representing the measured 2.4×10^{14} cm⁻² dopant density²⁵) is used. The use of a (4×4) unit cell necessitates a subsequent unfolding of the calculated band minima to their position in the (1×1) Brillouin zone that is probed in experiment. Two illustrative dopant arrangements are considered: “DFT1”, in which the four P dopants are clustered together in a square, and “DFT2”, in which they are placed in an ordered 2×2 pattern. The two calculated bandstructures are shown in Figure 3b and c, respectively.

■ ASSOCIATED CONTENT

■ Supporting Information

This contains a further description of the relevant Umklapp processes, and the implication for photoemission from bulk states. Further details of the DFT calculation including the

“unfolding” and the implications of dopant ordering on the calculated Fermi surface and valley splitting. A discussion of the absence of the bulk CBM and its position relative to the δ -layer states is also presented. This material is available free of charge via the Internet at <http://pubs.acs.org>.

■ AUTHOR INFORMATION

Corresponding Author

*E-mail: quantum.wells@gmail.com.

Notes

The authors declare no competing financial interest.

■ ACKNOWLEDGMENTS

We thank C. Polley, T. Balasubramanian, and Ph. Hofmann for valuable discussions and J. Adell for technical support. J.A.M acknowledges the Lundbeck Foundation via Liv Hornekær for providing financial support. O.W. and M.Y.S. are supported by the Australian Research Council (ARC) Centre of Excellence for Quantum Computation and Communication Technology (project number CE110001027) and M.Y.S. is also supported by the U.S. National Security Agency and the U.S. Army Research Office under contract number W911NF-08-1-0527. M.Y.S. and N.A.M. acknowledge the ARC for providing fellowships. J.W.W. acknowledges NTNU's TSO *materialer* program for supporting the collaboration.

■ REFERENCES

- (1) Koenraad, P. M.; Flatté, M. E. *Nat. Mater.* **2011**, *10* (2), 91–100.
- (2) Zwanenburg, F. A.; Dzurak, A. S.; Morello, A.; Simmons, M. Y.; Hollenberg, L. C. L.; Klimeck, G.; Rogge, S.; Coppersmith, S. N.; Eriksson, M. A. *Rev. Mod. Phys.* **2013**, *85*, 961–1019.
- (3) Fuechsle, M.; Miwa, J. A.; Mahapatra, S.; Ryu, H.; Lee, S.; Warschkow, O.; Hollenberg, L. C. L.; Klimeck, G.; Simmons, M. Y. *Nat. Nanotechnol.* **2012**, *7*, 242–246.
- (4) Fuechsle, M.; Mahapatra, S.; Zwanenburg, F.; Friesen, M.; Eriksson, M.; Simmons, M. *Nat. Nanotechnol.* **2010**, *5* (7), 502–505.
- (5) Weber, B.; Mahapatra, S.; Watson, T. F.; Simmons, M. Y. *Nano Lett.* **2012**, *12* (8), 4001–4006.
- (6) Büch, H.; Mahapatra, S.; Rahman, R.; Morello, A.; Simmons, M. Y. *Nat. Commun.* **2013**, *4*, 2017.
- (7) Qian, G.; Chang, Y.-C.; Tucker, J. R. *Phys. Rev. B* **2005**, *71*, 045309.
- (8) Goswami, S.; Slinker, K. A.; Friesen, M.; McGuire, L. M.; Truitt, J. L.; Tahan, C.; Klein, L. J.; Chu, J. O.; Mooney, P. M.; van der Weide, D. W.; Joynt, R.; Coppersmith, S. N.; Eriksson, M. A. *Nat. Phys.* **2007**, *3* (1), 41–45.
- (9) Roche, B.; Dupont-Ferrier, E.; Voisin, B.; Cobian, M.; Jehl, X.; Wacquez, R.; Vinet, M.; Niquet, Y.-M.; Sanquer, M. *Phys. Rev. Lett.* **2012**, *108*, 206812.
- (10) Rahman, R.; Verduijn, J.; Kharche, N.; Lansbergen, G. P.; Klimeck, G.; Hollenberg, L. C. L.; Rogge, S. *Phys. Rev. B* **2011**, *83*, 239904.
- (11) Isberg, J.; Gabrysch, M.; Hammersberg, J.; Majdi, S.; Kovi, K. K.; Twitchen, D. J. *Nat. Mater.* **2013**, *12* (8), 760–764.
- (12) Sakamoto, K.; Kim, T.-H.; Kuzumaki, T.; Müller, B.; Yamamoto, Y.; Ohtaka, M.; Osiecki, J. R.; Miyamoto, K.; Takeichi, Y.; Harasawa, A.; Stolwijk, S. D.; Schmidt, A. B.; Fujii, J.; Uhrberg, R. I. G.; Donath, M.; Yeom, H. W.; Oda, T. *Nat. Commun.* **2013**, *4*, 2073.
- (13) Carter, D. J.; Warschkow, O.; Marks, N. A.; McKenzie, D. R. *Phys. Rev. B* **2009**, *79*, 033204 (2009) and **80**, 049901.
- (14) Carter, D. J.; Marks, N. A.; Warschkow, O.; McKenzie, D. R. *Nanotechnology* **2011**, *22* (6), 065701.
- (15) Lee, S.; Ryu, H.; Campbell, H.; Hollenberg, L. C. L.; Simmons, M. Y.; Klimeck, G. *Phys. Rev. B* **2011**, *84*, 205309.
- (16) Drumm, D. W.; Hollenberg, L. C. L.; Simmons, M. Y.; Friesen, M. *Phys. Rev. B* **2012**, *85* (15), 155419.

- (17) Carter, D. J.; Warschkow, O.; Marks, N. A.; McKenzie, D. R. *Phys. Rev. B* **2013**, *87*, 045204.
- (18) Drumm, D. W.; Budi, A.; Per, M. C.; Russo, S. P.; Hollenberg, L. C. L. *Nanoscale Res. Lett.* **2013**, *8* (1), 1–11.
- (19) Smith, J. S.; Cole, J. H.; Russo, S. P. *Phys. Rev. B* **2014**, *89*, 035306.
- (20) Himpfel, F. J. *Appl. Opt.* **1980**, *19* (23), 3964–3970.
- (21) Miwa, J. A.; Hofmann, P.; Simmons, M. Y.; Wells, J. W. *Phys. Rev. Lett.* **2013**, *110*, 136801.
- (22) See Methods for a more detailed description.
- (23) Hofmann, P.; Søndergaard, C.; Agergaard, S.; Hoffmann, S. V.; Gayone, J. E.; Zampieri, G.; Lizzit, S.; Baraldi, A. *Phys. Rev. B* **2002**, *66*, 245422.
- (24) See Supporting Information for a more detailed description.
- (25) McKibbin, S. R.; Clarke, W. R.; Fuhrer, A.; Simmons, M. Y. *J. Cryst. Growth* **2010**, *312* (21), 3247–3250.
- (26) Polley, C. M.; Clarke, W. R.; Miwa, J. A.; Scappucci, G.; Wells, J. W.; Jaeger, D. L.; Bischof, M. R.; Reidy, R. F.; Gorman, B. P.; Simmons, M. *ACS Nano* **2013**, *7*, 5499–5505.
- (27) Polley, C. M.; Clarke, W. R.; Miwa, J. A.; Simmons, M. Y.; Wells, J. W. *Appl. Phys. Lett.* **2012**, *101* (26), 262105.
- (28) Boland, J. J. *Surf. Sci.* **1992**, *261* (1–3), 17–28.
- (29) Soler, J. M.; Artacho, E.; Gale, J. D.; García, A.; Junquera, J.; Ordejón, P.; Sánchez-Portal, D. *J. Phys.: Condens. Matter* **2002**, *14* (11), 2745.
- (30) Perdew, J. P.; Burke, K.; Ernzerhof, M. *Phys. Rev. Lett.* **1996**, *77*, 3865–3868.

“Spin-valley locking in the normal state of a transition-metal
dichalcogenide superconductor”

-- *Under review*--

Spin-valley locking in the normal state of a transition-metal dichalcogenide superconductor

L. Bowden,¹ S. P. Cooil,² F. Mazzola,² J. M. Riley,^{1,3} L. J. Collins-McIntyre,¹ V. Sunko,^{1,4}
K. Hunvik,² M. Leandersson,⁵ C. M. Polley,⁵ T. Balasubramanian,⁵ T. K. Kim,³
M. Hoesch,³ J. W. Wells,² G. Balakrishnan,⁶ M. S. Bahramy,^{7,8} and P. D. C. King^{1,*}

¹*SUPA, School of Physics and Astronomy, University of St. Andrews, St. Andrews, Fife KY16 9SS, United Kingdom*

²*Department of Physics, Norwegian University of Science and Technology (NTNU), N-7491 Trondheim, Norway*

³*Diamond Light Source, Harwell Campus, Didcot, OX11 0DE, United Kingdom*

⁴*Max Planck Institute for Chemical Physics of Solids, Nöthnitzer Straße 40, 01217 Dresden, Germany*

⁵*MAX IV Laboratory, Lund University, P. O. Box 118, 221 00 Lund, Sweden*

⁶*Department of Physics, University of Warwick, Coventry CV4 7AL, United Kingdom*

⁷*Quantum-Phase Electronics Center and Department of Applied Physics,*

The University of Tokyo, Tokyo 113-8656, Japan

⁸*RIKEN center for Emergent Matter Science (CEMS), Wako 351-0198, Japan*

(Dated: March 17, 2016)

The metallic transition-metal dichalcogenides (TMDCs) are benchmark systems for studying and controlling intertwined electronic orders in solids, with superconductivity developing upon cooling from a charge density wave state. The interplay between such phases is thought to play a critical role in the unconventional superconductivity of cuprates, Fe-based, and heavy-fermion systems, yet even for the more moderately-correlated TMDCs, their nature and origins have proved highly controversial. Here, we study a prototypical example, $2H\text{-NbSe}_2$, by spin- and angle-resolved photoemission and first-principles theory. We find that the normal state, from which its hallmark collective phases emerge, is characterised by quasiparticles whose spin is locked to their valley pseudospin. This results from a combination of strong spin-orbit interactions and local inversion symmetry breaking. Non-negligible interlayer coupling further drives a rich three-dimensional momentum-dependence of the underlying Fermi surface spin texture. Together, these findings necessitate a fundamental re-investigation of the nature of charge order and superconducting pairing in NbSe_2 and related TMDCs.

In combination with broken structural inversion symmetry, spin-orbit coupling (SOC) provides a powerful route to stabilise spin-polarised electronic states without magnetism. This can give rise to electrically-tuneable spin splittings via the Rashba effect, promising new technological developments in spintronics,¹ and underpins the formation of spin-helical Dirac cones at the surfaces of topological insulators.² It is strongly desired to realise similar effects in systems where more pronounced electronic interactions drive the emergence of collective phases. In non-centrosymmetric superconductors, for example, spin-splitting driven by strong SOC is expected to induce a mixing of spin-triplet and singlet superconducting order parameters,³ and offers potential for stabilising topological superconductors.⁴ Yet, identifying suitable candidate materials has proved a major challenge to date. Partly this is driven by a relative dearth of non-centrosymmetric metals, while for non-magnetic systems in which the centre of inversion is maintained, robust spin-degeneracies of their electronic states would typically be expected due to the dual constraints of time-reversal and inversion symmetry.

In contrast, we show here from spin- and angle-resolved photoemission (ARPES) measurements that the normal state of the centrosymmetric TMDC superconductor $2H\text{-NbSe}_2$ (hereafter denoted NbSe_2) hosts a strong layer-resolved and momentum-dependent spin-polarisation of

its electronic states at and in the vicinity of the Fermi level. We attribute this as a consequence of a recently-realised form of spin polarisation that can emerge in globally centrosymmetric materials in which constituent structural units nonetheless break inversion symmetry.^{5–7} Together with first-principles calculations, we show how this drives a critical and complex interplay of interlayer interactions and spin-orbit coupling in NbSe_2 . This yields a rich underlying spin-polarised electronic landscape from which charge order and superconductivity emerge upon cooling.

Results

Bulk electronic properties of NbSe_2 . We consider here exclusively the layered $2H$ polymorph (Fig. 1(a)). Each layer forms a graphene-like honeycomb structure with Nb occupying the “A” sublattice and two Se atoms situated on the “B” sublattice. These lie out of the basal plane, equidistant above and below the transition metal. The unit cell contains two such layers, stacked along the c -axis with 180° in-plane rotation. Our resistivity measurements (Fig. 1(b)) from single-crystal NbSe_2 samples show a metallic temperature-dependence. They additionally exhibit a pronounced hump at a temperature of $T_{\text{CDW}} \approx 33$ K indicative of charge-density wave (CDW) formation,⁸ as well as a sharp superconducting transition at $T_c \approx 7$ K. The corresponding normal-state Fermi sur-

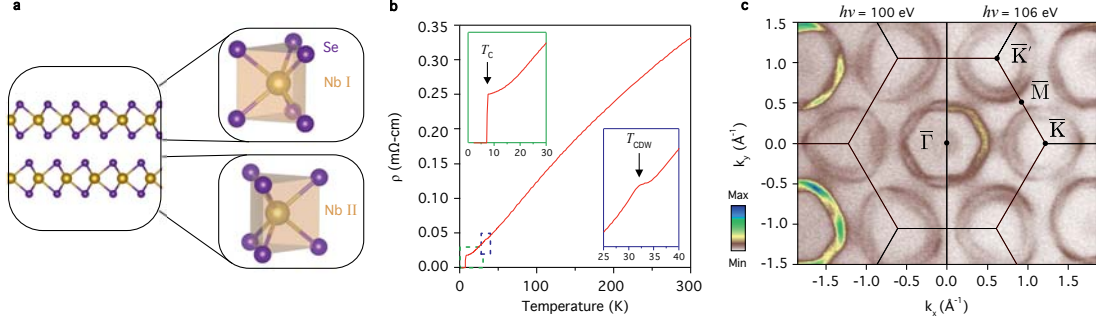


FIG. 1: **Superconductivity and charge density wave order in 2H-NbSe₂.** (a) Centrosymmetric bulk crystal structure (side view) of 2H-NbSe₂. This is formed by stacking non-centrosymmetric layers of D_{3h} symmetry with 180° relative rotations, restoring the bulk inversion centre. (b) Resistivity measurements show clear signatures of charge-density wave formation at $T_{CDW} \approx 33$ K and superconductivity at $T_c \approx 7$ K (magnified in the insets). (c) Normal-state Fermi surface measured by ARPES with $h\nu = 100$ eV (left-hand-side) and $h\nu = 106$ eV (right-hand-side); $E_F \pm 20$ meV. This consists of two Nb-derived barrels centred around the zone-corner \bar{K} (\bar{K}') points, two Nb-derived barrels at the Brillouin zone centre, and an additional central diffuse pocket (most visible at $h\nu = 106$ eV) predominantly derived from Se p_z orbitals.

face is shown in Fig. 1(c), as measured by ARPES. There are two barrels centred around each zone-corner \bar{K} (\bar{K}') point which are strongly trigonally-warped. Two further barrels are centred at the $\bar{\Gamma}$ point, the inner of which is hexagonal while the outer exhibits additional warping. From our first-principles density-functional theory calculations, and consistent with previous studies,^{9–11} we assign all four of these Fermi surface sheets as being predominantly derived from Nb $4d$ orbitals. Additional spectral weight at the zone centre is evident in our ARPES measurements for selected photon energies, which we attribute as a fifth, highly three-dimensional, Fermi surface sheet of predominantly Se p_z orbital character.

This sheet also contributes diffuse filled-in intensity, due to the finite out-of-plane momentum (k_z) resolution of ARPES, close to the zone centre in measurements of the electronic dispersions along in-plane high-symmetry directions (Fig. 2(a)). The Nb-dominated states, on the other hand, yield clear spectral features close to their Fermi crossings. Kinks in their measured dispersion and a decrease in linewidth near the Fermi level point to relatively-strong electron-phonon coupling in this system.^{11–13} It is these Nb-derived states that are known to host the largest energy gaps at the Fermi level arising from the CDW and superconducting instabilities in this system,^{13–16} although the origins of these have proved highly controversial.^{8,10,11,13–22} To the best of our knowledge, all prior theoretical treatments assume these orders emerge from an electronic liquid of trivially spin-degenerate character. Indeed, standard expectations of group theory would say this must be the case for the centrosymmetric space group ($P6_3/mmc$) of 2H-NbSe₂.

In contrast, we directly observe pronounced spin po-

larisations of the underlying electronic states in spin-resolved energy distribution curves (spin-EDCs, see Methods) measured along the $\bar{\Gamma} - \bar{K}$ direction, shown in Fig. 2(c-f). This is particularly apparent close to the saddle point of these bands (Fig. 2(d)), where two clearly-separated peaks can be observed in spin-EDCs. The measured spin polarisation is almost entirely out-of-plane (Fig. 2(d) and Supplemental Fig. S1), with a sign that reverses between the two bands. We attribute this as arising from local inversion symmetry breaking within the individual layers that make up the bulk crystal structure.^{5,6,23} For sufficiently weak interlayer interactions (a point we return to below), pronounced spin-orbit coupling characteristic of the $4d$ transition metal can lift the spin-degeneracy of the states localised within each layer, that thus strongly “feel” the local inversion asymmetry. A layer-dependent sign change of this spin polarisation, mediated by the rotated layer stacking of the bulk crystal structure, would act to restore overall spin degeneracy as required by global inversion and time-reversal symmetries. Nonetheless, the electronic states retain strong layer-resolved spin polarisations. Depth-averaging probes would largely be insensitive to these, but photoemission is a surface sensitive technique. Incoherent superposition of photoelectrons emitted from neighbouring layers of the unit cell would lead to some suppression of the measured spin polarisation, while interference effects can further complicate this picture⁵. Nonetheless, the extreme surface sensitivity at the photon energies used here, with an inelastic mean free path on the order of the inter-layer separation, renders us predominantly sensitive to the spin texture of the top-most layer of the unit cell.

Spin-valley locking. Our measurements show that

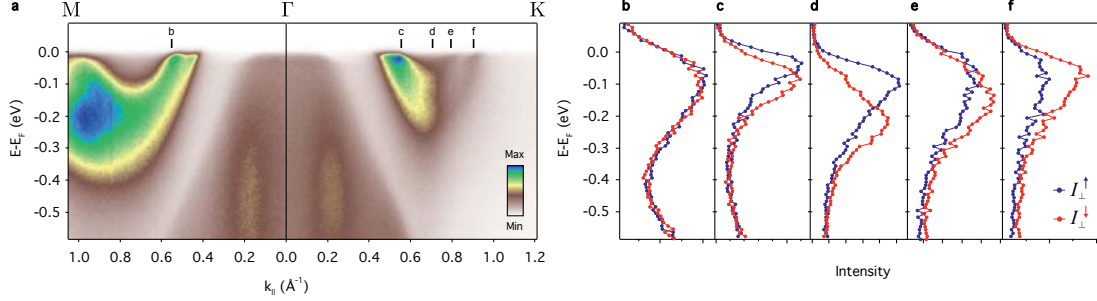


FIG. 2: **Spin-polarised bulk electronic structure.** (a) Dispersion measured by ARPES ($h\nu = 22$ eV) along the $\bar{M}-\bar{\Gamma}-\bar{K}$ direction. (b)-(f) Spin-resolved EDCs at the momenta marked in (a), revealing a strong spin polarisation of these electronic states along $\bar{\Gamma}-\bar{K}$.

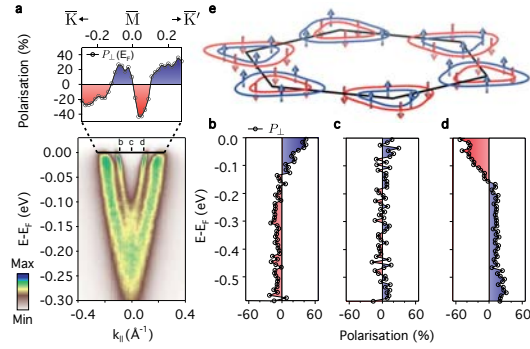


FIG. 3: **Spin-valley locked Fermi surfaces.** (a) Dispersion measured ($h\nu = 22$ eV) along the $\bar{K}-\bar{M}-\bar{K}'$ direction, together with the corresponding spin-polarisation of an MDC at the Fermi level and (b-d) EDCs at the momenta marked in (a). These reveal how the sign of the spin polarisation for each zone-corner Fermi surface sheet becomes locked to the valley degree of freedom, as shown schematically in (e).

such non-trivial spin textures in NbSe₂ persist up to the Fermi level. This is evident in spin-resolved EDCs along the $\bar{\Gamma}-\bar{K}$ direction (Fig. 2(c-f)) as well as the spin polarisation of EDCs and a Fermi-level momentum distribution curve (MDC) along the $\bar{K}-\bar{M}-\bar{K}'$ direction (Fig. 3). The latter clearly reveals how the spin polarisation reverses sign for each pair of Fermi surface sheets centred on neighbouring \bar{K} and \bar{K}' points. This is a natural consequence of time-reversal symmetry. Here, this results in a coupling of the spin to the so-called valley index, the quantum number which distinguishes \bar{K} - and \bar{K}' -centred Fermi surfaces in NbSe₂ (Fig. 3(e)). Such spin-valley coupling has recently been extensively investigated for the band extrema in mono-

layers of semiconducting TMDCs,²⁴⁻²⁶ where it has not only been shown to lead to new physics, such as a valley Hall effect,²⁷ but also to offer potential for devices exploiting the valley pseudospin.^{28,29} Our observations here point to a pronounced role of spin-valley coupling also for the low-energy quasiparticle excitations of the metallic 2H-structured TMDCs.

Critically, it is from this spin-polarised Fermi sea that electron-hole and electron-electron pairing interactions drive the formation of CDW order and superconductivity. The largest CDW gaps in NbSe₂ are located on the zone-corner spin-valley locked Fermi surfaces.¹³ The CDW wave vector is entirely in-plane,³⁰ making such hidden layer-dependent spin polarisations relevant: we thus conclude that these cannot be viewed as purely *charge* density wave states with no role of the spin degree of freedom. The underlying spin textures can also be expected to have important implications for superconductivity. Recent measurements on electrically-gated MoS₂, which is known to host a strong spin-valley locking in its band structure,^{25,26} have found evidence for unconventional so-called Ising superconductivity.^{31,32} In this, the pronounced spin-orbit field that induces the underlying spin texture of the electronic states pins the spin of Cooper pair electrons in the out-of-plane direction. This leads to upper critical fields dramatically exceeding the Pauli paramagnetic limit for a magnetic field applied within the *ab*-plane. Similar phenomenology has recently been reported for mono- and few-layer NbSe₂,³³ entirely consistent with our direct observation of spin-valley locking in this compound.

In bulk NbSe₂, the spin-layer locking, and also multi-band nature as compared to gated MoS₂, raises further prospects for stabilising a delicate balance between different pairing states. In the normal state, we find that the $\bar{\Gamma}$ -centred Fermi surface barrels, which are known to support a modulated superconducting gap in the bulk,^{13,34} are also strongly spin-polarised along the $\bar{\Gamma}-\bar{K}$ direction

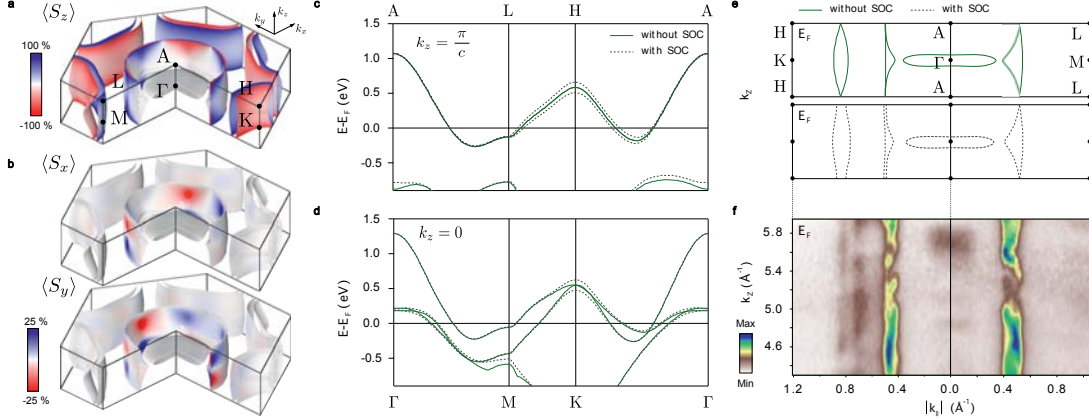


FIG. 4: **Interplay of interlayer interactions and intralayer inversion symmetry breaking.** (a,b) Density-functional theory calculations of the (a) out-of-plane and (b) in-plane spin polarisation of the three-dimensional Fermi surface of NbSe₂ projected onto the first layer of the unit cell. (c,d) Calculated electronic structure along (c) $A-L-H-A$ ($k_z = \pi/c$) and (d) $\Gamma-M-K-\Gamma$ ($k_z = 0$) with and without SOC. (e) Corresponding influence of SOC on the Fermi surface contours in the $\Gamma-K-H-A$ and $\Gamma-M-L-A$ planes (shown throughout the full three-dimensional Brillouin zone in Supplemental Fig. S2). (f) Our experimental ARPES measurements of such k_z -dependent Fermi surfaces ($\hbar\nu = 60$ to 130 eV) are in good general agreement with the theoretical calculations including SOC, supporting a SOC-mediated suppression of interlayer hopping in the $\Gamma-K-H-A$ plane.

(Fig. 2(c)). Their spin polarisation, however, is completely suppressed along $\bar{\Gamma}-\bar{M}$ (Fig. 2(b)). Intriguingly, the largest superconducting gaps of this Fermi surface determined in Ref.¹³ are located at the regions of strongest spin polarisation evident here. Pronounced superconducting gaps are also known to occur on the zone-corner Fermi surfaces,^{13,15,34} which, as demonstrated above, host strong spin-valley locking even in the bulk. Given the significant influence of SOC, a mixing of spin-triplet and spin-singlet order parameters could potentially be expected.³ Forming even pseudospin-singlet Cooper pairs from the strongly spin-polarised Fermi surfaces could necessitate a phase locking between the order parameter of neighbouring Fermi surface sheets. Moreover, the c -axis coherence length in NbSe₂ is much greater than the interlayer separation.^{35,36} This raises the tantalising prospect that the inherent coupling between the spin and layer pseudospins reported here could be tuned to drive an instability to an odd-parity pair density wave state, where the sign of the superconducting gap becomes tied to the layer index.^{7,37} The proximity of bulk NbSe₂ and similar compounds to such phases requires further theoretical exploration, and will depend sensitively on the relative importance of inter- and intra-band as well as interlayer pairing interactions.

Three-dimensional spin structure. Our density-functional theory calculations (Fig. 4) already reveal a key role of interlayer interactions in mediating and controlling the underlying spin texture of the normal-state

bulk Fermi surface. The calculated spin-polarisation projected onto the first layer of the unit cell is shown throughout the full three-dimensional Brillouin zone in Fig. 4(a,b). The momentum-dependent spin polarisations are determined by the effective spin-orbit field, $B_{so} = \beta(\nabla V \times \mathbf{k})$, where β is a momentum-dependent scaling factor, ∇V is the net electrostatic potential gradient, and \mathbf{k} is the crystal momentum. The horizontal mirror symmetry of each NbSe₂ structural unit about the transition-metal plane (σ_h of the D_{3h} point group; Fig. 1(a)) ensures that ∇V is entirely within the xy plane. Due to the 180° relative rotation of neighbouring NbSe₂ monolayers in the bulk crystal structure, ∇V , and thus B_{so} , has opposite sign for successive layers in the unit cell. This causes the sign of the spin polarisation to reverse at each momentum-space point when projected onto layer 2 vs. layer 1 of the unit cell (Supplemental Fig. S3). This confirms that local inversion asymmetry within each NbSe₂ layer drives the formation of the spin-polarised states observed here.

For electronic states whose wavefunctions are completely delocalised over both layers of the unit cell, the spin-orbit field from each layer cancels. Such states are consequently unpolarised, restoring the conventional expectations for a centrosymmetric space group. This can be observed for the highly three-dimensional “pancake” Fermi surface at the Brillouin zone centre here. In contrast, for electronic states predominantly localised within individual layers of the unit cell, strong layer-dependent spin-orbit fields mediate large layer-resolved spin polari-

sations. This is ideally realised at the three-dimensional Brillouin zone boundary along k_z ($k_z = \pi/c$). In a tight-binding picture, for this k_z , interlayer hoppings within a unit cell and between neighbouring unit cells are out of phase with each other and thus cancel.¹⁰ This can be directly visualised by comparing the dispersion of the electronic states along the Γ - M - K - Γ and A - L - H - A directions: neglecting SOC, a single four-fold degenerate band crosses the Fermi level in the $k_z = \pi/c$ plane (Fig. 4(c)), whereas this is split into a pair of two-fold degenerate bands by interlayer interactions for $|k_z| < \pi/c$, as evident in Fig. 4(d).

With its forbidden interlayer coupling, the electronic structure for the $k_z = \pi/c$ plane is thus formally equivalent to that of an isolated monolayer. The spin-orbit field is consequently maximised, driving the largest ($> 90\%$) layer-dependent spin-polarisations. These are purely out-of-plane (Fig. 4(a,b)), as $(\nabla V \times \mathbf{k})$ must lie entirely along z at the Brillouin zone boundary along k_z . Along the A - L direction, however, a vertical mirror plane in the crystal structure forbids any out-of-plane component of $(\nabla V \times \mathbf{k})$. The spin-orbit field must therefore be strictly zero along A - L . This enforces a touching, and hence spin-degeneracy, of the zone-centre Fermi surface barrels along this direction, which are otherwise strongly spin-polarised throughout the $k_z = \pi/c$ plane.

For other k_z through the Brillouin zone, the spin-orbit field strength can be partially suppressed by finite interlayer coupling. Moreover, the z -component of the momentum induces a non-zero component of $(\nabla V \times \mathbf{k})$ in the xy plane. Together, this causes not only the magnitude of the Fermi surface spin polarisation, but also its vectorial spin texture, to develop a strong dependence on both the in- and out-of-plane momentum (Fig. 4(a,b)). Within the Γ - M - L - A plane, the calculated Fermi surface crossings are relatively strongly dispersive in k_z (Fig. 4(e)). This is consistent with our experimental measurements of the k_z -dependent Fermi surface (Fig. 4(f)) and points to significant interlayer coupling. Even away from $k_z = \pi/c$, the Fermi surface spin polarisations therefore become strongly suppressed in the entire vicinity of the Γ - M - L - A plane.

For the Γ - K - H - A plane, however, we find that the k_z dispersion of the Fermi surface crossings are significantly reduced by the inclusion of spin-orbit coupling in the calculations (Fig. 4(e)), in keeping with our experimental measurements of more two-dimensional Fermi contours for this plane (Fig. 4(f)). This reduction in k_z dispersion is achieved by a lifting, via SOC, of the four-fold degeneracy that would otherwise be present along the A - H line, and is accompanied by the emergence of strong spin-polarisation of the Fermi surface crossings for $k_z = \pi/c$. This is in contrast to the A - L line, where the energetic degeneracy of the Fermi crossings is protected by their symmetry-enforced spin degeneracy. The reduction of k_z -dispersion within the Γ - K - H - A plane is equivalent to

a spin-orbit-mediated suppression of interlayer hopping here.²⁸ This allows relatively strong spin polarisations to be maintained in the vicinity of this plane, with only a moderate suppression of the spin-orbit field strength away from $k_z = \pi/c$.

For momenta close to the K - H line, the in-plane momentum is always much larger than the out-of-plane component. This causes $(\nabla V \times \mathbf{k})$ to remain predominantly aligned along z . The spin polarisations of the zone-corner Fermi surfaces are thus largely out-of-plane throughout the full Brillouin zone (Fig. 4(a)). For the Nb-derived zone-centre Fermi surface barrels, however, much stronger (up to $\sim 25\%$) in-plane components develop (Fig. 4(b)). The in-plane spin texture is largely radial to the Fermi surface (Supplemental Fig. S4), and switches sign about the $k_z = 0$ plane. This indicates a non-zero component of $(\nabla V \times \mathbf{k})$ within the plane, with a direction that is tied to the sign of k_z . It thus confirms that an in-plane component of the spin texture arises due to finite out-of-plane momentum, where no symmetry constraint exists to cancel the in-plane component of the spin-orbit field for low-symmetry momenta with $0 < |k_z| < \pi/c$. The existence of such hidden in-plane spin textures is a unique property of the bulk compound. Indeed, the in-plane spin component goes strictly to zero at the Brillouin zone boundary along k_z , enforced by symmetry, and recovering a monolayer-like purely out-of-plane spin texture for $k_z = \pm\pi/c$. The bulk system thus hosts a rich intertwining of spin, orbital, and layer degrees of freedom, mediating a three-dimensional nature of its spin texture that can be expected to further modulate its pairing interactions.³¹

Discussion

Taken together, our results show how the combination of interlayer hopping and intra-layer inversion symmetry breaking can lead to particularly rich momentum-dependent spin textures of metallic TMDCs. Suppression of Fermi surface spin polarisation away from the Brillouin zone boundary along k_z will be reduced with decreased interlayer interactions. Indeed, upper critical fields, already known to exceed the Pauli limit for bulk NbSe₂,³⁸ are dramatically enhanced in other 2H-TMDC superconductors as a function of increasing interlayer separation.³⁹ This points to a susceptibility of the bulk systems to Ising superconductivity similar to that recently observed in isolated monolayers.³³ The delicate balance between interlayer hopping and spin-orbit coupling strength in NbSe₂ makes this an ideal material for understanding and ultimately controlling the role of layer-dependent spin polarisations on the collective states and phases of transition-metal dichalcogenides.

Methods

ARPES: Spin-resolved ARPES measurements were performed at the I3 beamline of MAX-IV Laboratory, Sweden,

and ARPES measurements were performed using the I05 beamline of Diamond Light Source, UK. Measurements were performed at temperatures of 50–80 K using p -polarised synchrotron light. Scienta R4000 hemispherical electron analysers were utilised for all measurements. This was additionally fitted with a mini-Mott detector scheme for the spin-ARPES measurements, configured to simultaneously probe the out-of-plane and in-plane (along the analyser slit direction) component of the photoelectron spin.⁴⁰ The finite spin-detection efficiency was corrected using a Sherman function of $S = 0.17$,⁴⁰ and the spin-resolved EDCs determined according to

$$I_i^{\uparrow,\downarrow} = I_i^{tot}(1 \pm P_i)/2$$

with $i = \{\perp, \parallel\}$, $I_i^{tot} = (I_i^+ + I_i^-)$, I_i^\pm the measured intensity on the individual detectors in the Mott scattering chamber, corrected by a relative detector efficiency calibration, and the total spin polarisation,

$$P_i = \frac{(I_i^+ - I_i^-)}{S(I_i^+ + I_i^-)}.$$

Calculations: Density-functional theory (DFT) calculations including spin-orbit coupling were performed using the modified Becke-Johnson exchange potential and Perdew-Burke-Ernzerhof correlation functional implemented in the WIEN2K program.⁴¹ A $20 \times 20 \times 10$ k -mesh was employed. The DFT results were downfolded using maximally localised Wannier functions,^{42–44} employing Nb $4d$ orbitals and Se $5p$ orbitals as basis functions. The resulting tight-binding Hamiltonian allows a direct extraction of the spin and layer projections of the electronic structure.

Acknowledgements We thank M.R. Lees for assistance with the transport measurements and C. Hooley, P. Wahl, A.P. Mackenzie, S. Lee, and B. Braunecker for useful discussions. We gratefully acknowledge support from the Engineering and Physical Sciences Research Council, UK (work at St Andrews under Grant Nos. EP/I031014/1 and EP/M023427/1 and work at Warwick under Grant No. EP/M028771/1) and the International Max Planck partnership. PDCK acknowledges support from the Royal Society through a University Research Fellowship. MSB was supported by the Grant-in-Aid for Scientific Research (S) (No. 24224009) from the Ministry of Education, Culture, Sports, Science and Technology (MEXT) of Japan. LB, JR, and VS acknowledge studentship funding from EPSRC through grant nos. EP/G03673X/1, EP/L505079/1, and EP/L015110/1, respectively. The experiments at MAX IV Laboratory were made possible through funding from the Swedish Research Council and the Knut and Alice Wallenberg Foundation. We also thank Diamond Light Source for access to beamline I05 (proposal no. SI11383) that contributed to the results presented here.

* To whom correspondence should be addressed: philip.king@st-andrews.ac.uk

- [1] Manchon, A. Koo, H. C., Nitta, J., Frolov, S. M. and Duine, R. A., New perspectives for Rashba spin-orbit coupling, *Nature Mater.* **14**, 871-882 (2015).
- [2] Hasan, M. Z. and Kane, C. L., Colloquium: Topological insulators, *Rev. Mod. Phys.* **85**, 3045 (2010).
- [3] Gor'kov, L. P. and Rashba, E. I., Superconducting 2D system with lifted spin degeneracy: Mixed singlet-triplet state, *Phys. Rev. Lett.* **87**, 037004 (2001).
- [4] Sato, M. and Fujimoto, S., Topological phases of noncentrosymmetric superconductors: Edge states, Majorana fermions, and non-Abelian statistics, *Phys. Rev. B* **79**, 094504 (2009).
- [5] Riley, J. M. *et al.*, Direct observation of spin-polarized bulk bands in an inversion-symmetric semiconductor, *Nature Phys.* **10**, 835-839 (2014).
- [6] Zhang, X., Liu, Q., Luo, J.-W., Freeman, A. J., and Zunger, A., Hidden spin polarization in inversion-symmetric bulk crystals, *Nature Phys.* **10**, 387-393 (2014).
- [7] Sigrist, M. *et al.*, Superconductors with staggered non-centrosymmetry, *J. Phys. Soc. Jpn.* **83**, 061014 (2014).
- [8] Wilson, J. A., Di Salvo, F. J., and Mahajan, S., Charge-density waves in metallic, layered, transition-metal dichalcogenides, *Phys. Rev. Lett.* **32**, 882 (1974).
- [9] Rossnagel, K. *et al.*, Fermi surface of $2H$ -NbSe₂ and its implications on the charge-density-wave mechanism, *Phys. Rev. B* **64**, 235119 (2001).
- [10] Johannes, M. D, Mazin, I. I, and Howells, C. A., Fermi-surface nesting and the origin of the charge-density wave in $2H$ -NbSe₂, *Phys. Rev. B* **73**, 205102 (2006).
- [11] Flicker, F. and van Wezel, J., Charge order from orbital-dependent coupling evidenced by NbSe₂, *Nature Commun.* **6**, 7034 (2015).
- [12] Weber, F. *et al.*, Electron-phonon coupling and the soft phonon mode in TiSe₂, *Phys. Rev. Lett.* **107**, 107403 (2011).
- [13] Rahn, D. J. *et al.*, Gaps and kinks in the electronic structure of the superconductor $2H$ -NbSe₂ from angle-resolved photoemission at 1 K *Phys. Rev. B* **85**, 224532 (2012).
- [14] Kiss, T. *et al.*, Charge-order-maximized momentum-dependent superconductivity, *Nature Phys.* **3**, 720-725 (2007).
- [15] Yokoya, T., Kiss, T., Chainani, A., Shin, S., Nohara, M. and Takagi, H., Fermi surface sheet-dependent superconductivity in $2H$ -NbSe₂, *Science* **294**, 2518-2520 (2001).
- [16] Borisenko, S. V. *et al.*, Two energy gaps and Fermi-surface “arcs” in NbSe₂, *Phys. Rev. Lett.* **102**, 166402 (2009).
- [17] Xi, X. *et al.*, Strongly enhanced charge-density-wave order in monolayer NbSe₂, *Nature Nano.* **10**, 765-769 (2015).
- [18] Rice, T. M. and Scott, G. K., New mechanism for a charge-density-wave instability, *Phys. Rev. Lett.* **35**, 120 (1975).
- [19] Shen, D. W. *et al.*, Primary role of the barely occupied states in the charge density wave formation of NbSe₂, *Phys. Rev. Lett.* **101**, 226406 (2008).
- [20] Rossnagel, K., On the origin of charge-density waves in select layered transition-metal dichalcogenides, *J. Phys. Cond. Mat.* **23**, 21 (2011).
- [21] Soumyanarayanan, A. *et al.*, Quantum phase transition from triangular to stripe charge order in NbSe₂ *P. Nat.*

- Acad. Sci. USA* **110**, 1623-1627 (2013).
- [22] Laverock, J. *et al.*, k -resolved susceptibility function of 2H-TaSe₂ from angle-resolved photoemission, *Phys. Rev. B* **88**, 035108 (2013).
- [23] Riley, J. M. *et al.*, Negative electronic compressibility and tunable spin splitting in WSe₂, *Nature Nano.* **10**, 1043-1047 (2015).
- [24] Xiao, D., Liu, G.-B., Feng, W., Xu, X. and Yao, W., Coupled spin and valley physics in monolayers of MoS₂ and other group-VI dichalcogenides, *Phys. Rev. Lett.* **108**, 196802 (2012).
- [25] Mak, K. F., He, K., Shan, J. and Heinz, T. F., Control of valley polarization in monolayer MoS₂ by optical helicity *Nature Nano.* **7**, 494-498 (2012).
- [26] Zeng, H., Dai, J., Yao, W., Xiao, D. and Cui, X., Valley polarization in MoS₂ monolayers by optical pumping, *Nature Nano.* **7**, 490-493 (2012).
- [27] Mak, K. F., McGill, K. L., Park, J., and McEuen, P. L., The valley Hall effect in MoS₂ transistors, *Science* **344**, 1489-1492 (2014).
- [28] Gong, Z. *et al.*, Magnetoelectric effects and valley-controlled spin quantum gates in transition metal dichalcogenide bilayers, *Nature Comm.* **4**, 2053 (2013).
- [29] Xu, X., Yao, W., Xiao, D. and Heinz, T. F., Spin and pseudospins in layered transition metal dichalcogenides, *Nature Phys.* **10**, 343-350 (2014).
- [30] Moncton, D. E. *et al.*, Neutron scattering study of the charge-density wave transitions in 2H-TaSe₂ and 2H-NbSe₂, *Phys. Rev. B* **16**, 801 (1977).
- [31] Saito, Y. *et al.*, Superconductivity protected by spin-valley locking in gate-tuned MoS₂, *Nature Phys.* **12**, 144-149 (2016).
- [32] Lu, J. M. *et al.*, Evidence for two-dimensional Ising superconductivity in gated MoS₂, *Science* **350**, 1353-1357 (2015).
- [33] Xi, X. *et al.*, Ising pairing in superconducting NbSe₂ atomic layers, *Nature Phys.* **12**, 139-143 (2016).
- [34] Huang, C. L. *et al.*, Experimental evidence for a two-gap structure of superconducting NbSe₂: A specific-heat study in external magnetic fields, *Phys. Rev. B* **76**, 212504 (2007).
- [35] Sanchez, D., Junod, A., Muller, J., Berger, H. and Lévy, F., Specific heat of 2H-NbSe₂ in high magnetic fields, *Physica B* **204**, 167-175 (1995).
- [36] Nader, A. and Monceau, P., Critical field of 2H-NbSe₂ down to 50 mK, *SpringerPlus* **3**, 16 (2014).
- [37] Yoshida, T., Sigrist, M. and Yanase, Y., Pair-density wave states through spin-orbit coupling in multilayer superconductors, *Phys. Rev. B* **86**, 134514 (2012).
- [38] Foner, S. and McNiff Jr, E. J., Upper critical fields of layered superconducting NbSe₂ at low temperature, *Phys. Lett. A* **45**, 429-430 (1973).
- [39] Klemm, R. A., Pristine and intercalated transition metal dichalcogenide superconductors, *Physica C* **514**, 86-94 (2015).
- [40] Berntsen, M. H. *et al.*, A spin- and angle-resolving photoelectron spectrometer, *Rev. Sci. Instrum.* **81**, 035104 (2010).
- [41] Blaha, P. *et al.*, WIEN2K package, Version 10.1 (2010); available at <http://www.wien2k.at>.
- [42] Souza, I. *et al.*, Maximally localized Wannier functions for entangled energy bands, *Phys. Rev. B* **65**, 035109 (2001).
- [43] Mostofi, A. A. *et al.*, Wannier90: A Tool for obtaining maximally localised Wannier functions, *Comp. Phys. Commun.* **178**, 685699 (2008).
- [44] Kuneš, J. *et al.*, WIEN2WANNIER: From linearized augmented plane waves to maximally localized Wannier functions, *Comp. Phys. Commun.* **181**, 1888-1895 (2010).

“Surface Dimensionality Transition on a Curved Bi(111) Sample:
Surface States Evolution from Topologically Trivial to Topologically
protected”

Work in progress, “first draft”

Is not included due to copyright

“In-situ growth and characterization of patterned δ -layer structures in Silicon”

Work in progress

Is not included due to copyright

“Degradation of the chemotherapy drug 5-Fluorouracil on medical silver surfaces”

Work in progress

Is not included due to copyright

Chapter 8

Conclusions

Over the last decades, silicon has been the workhorse of the semiconductor industry for its use in electronics. It is nowadays the industry standard, which gives birth every year to a vast array of novel applications, including mobile telephones, solar cells and computers. In order to meet higher performances and faster responses to external stimuli, technology requires more and smaller components per silicon chip every day. This relentless miniaturization process is well described by Moore's law, according to which the number of components per silicon chip doubles every 2 years (alternatively, the size of components halves with the same rate). Nowadays, the Moore's law is at its real end: the sizes of transistors shrank so much, that the true quantum-mechanical regime is approached. New ideas, new concepts and new materials are indispensable to lead to new technologies.

One way to overcome such a continuous size-scaling is to enhance the capabilities of standard semiconductors with functional materials hosting properties beyond traditional semiconductors possibilities. Reaching control over single dopants is desired for quantum-computation, as well as the possibility of patterning quantum architectures with atomic precision. This offers indeed potential for gaining an unprecedented control over the carrier lifetimes for devices working at the quantum-regime. A perfect candidate for this purpose is Si:P δ -layer. This hybrid system plays a key-role as a platform for spin and quantum computation because of its long electron and nuclear coherence times [68, 69]. More efficient devices and information storage/processing technology will strongly benefit from the integration of Si:P δ -layers into current electronics: this material is particularly suitable to be

patterned with atomic precision, and transistors with desired architectures can be built with sizes down to the atomic-scale. Controlling and tuning the metallic properties of Si:P δ -layers is a premier goal for its possible use in electronics and particular attention is given to the separation and energy position of the electronic states of this system at Fermi level, hence responsible for its metallicity. Such states are indeed related to coherence times and transport and manipulating them opens the viability towards manufacturing material properties in quantum-architectures.

To this end, we used ARPES to gain valuable feedback about the effect of the quantum-confinement to the electronic structure of Si:P δ -layers: we show how introducing an asymmetry in the P profile is a robust method to generate additional metallic states other than the ones predicted for a symmetric line profile (Paper 4). This results in a significant increase in the carrier density. We also show how the peculiar artificial design of the quantum confinement (Paper 2) in these structures leads to the quantization of the valence band whilst keeping the conduction band the same (Paper 3), thus, even if the valence band is not involved directly in transport properties, we can speculate about possible channels for exploiting electrostatic gating to put the valence and the conduction bands at similar energies to induce electrons tunneling between them. If such a tunneling can be realized, the valence band could be used as an electrons-reservoir for the conduction band, influencing the electron-hole recombination process and ultimately the lifetime of carriers. All these studies are done in the perspective of real device fabrication, thus it is also important to understand the factors which limit the lifetime of carriers. Therefore, classifying, studying and understanding many-body effects in Si:P δ -layer becomes precious information, and ARPES becomes an ideal probe for the collective behavior of the electrons in this system (Paper 1). Ultimately, we used a photoemission electron microscope to pattern this material at the micrometer scale, creating proper quantum artificial architectures, whilst investigating *in situ* and with the same instrument their electronic properties (Paper 16). A future goal would be to probe the effect of lateral confinement by using this instrument or possibly nano-ARPES, understanding how the electronic structure of Si:P δ -layer is affected by confining these system in all the 3D coordinates x , y and z . This would open important conceptual pathways for understanding the electronic properties of real electronic components made of this material, ultimately allowing for the creation of artificial digital quantum structures for quantum-computations.

Atomic scale patterning Si:P δ -layers is certainly an important achievement, but unfortunately very time-consuming. Ideally, it would be desired to produce in large IT production scale quantum-confined architectures. In this respect, self-assembly molecules offer a unique solution to this problem: if on top of a metallic substrate, these organic molecules self-assemble to form a periodic array of quantum dots, then atomic-scale control over a large area is easily achieved. On-surface molecular networks offer great potential as building blocks for electronic components: as inorganic semiconductors, they can be indeed exploited for tailoring quantum-computer architectures at the nanometer-scale but they have the extraordinary advantage to arrange themselves in a periodic fashion without the need of any further fine engineering manipulation. A goal of my PhD work has been to study the electronic properties of these incredible systems via photoemission, getting valuable insight into the nature and properties of these materials. To this end, we used a self-assembling porphyrins network (paper 5). Generally, studying organic molecules with photoemission is a challenging task, and particularly challenging is getting information about their electronic dispersion using ARPES. This is mainly due to the fact that molecules can get easily damaged upon radiation and that organic molecules generally have a big unit cell, resulting in a small Brillouin zone. The clever photoemission ‘trick’ we used to acquire the electronic dispersion of a porphyrin network is to use relatively low photon energies and detune the undulator of the beam-line, such that the flux is kept at a lower value than the one which would be otherwise used for standard materials. Additionally, for the same reasons the measurement time for each spectrum must be also kept short and the light spot size big, in order to reduce the amount of irradiation per unit area. A big spot-size would normally destroy the momentum resolution of ARPES spectra, however, the low energies used in the experiment allow to compensate for this effect.

Whilst organic compounds are suitable to be integrated into technology because of their property of self-assembling, their biggest limitation is a severe degradation in certain hostile environments, such as in radioactive areas. If the environment is a nuclear-area, this problem has to be extended to semiconductors as well because they can also get damaged upon a strong radiation dose. In these cases, nanometer-scale architectures for electronics must be robust and their desired lifetime long. Nanometer-scale boron-doped

diamond is suitable for this aim. Nevertheless, its electronic properties have been poorly understood, especially it would be desired to understand why transport measurements carried out on thin layers (≈ 2 nm) have never shown a real putative 2D behavior. By ARPES we directly accessed the electronic properties of these samples, shedding light onto this unexpected mechanism and demonstrating that the Debye lengths in these systems are still comparable to a 3D system (paper 6). This hints at the intriguing possibility to make nanometer-scale devices preserving the properties of bulk boron-doped diamond. Whilst the general bulk-properties are overall preserved by thin film material, we also found a significant change in the effective mass and band-width between these systems. In particular, thin film diamond shows an enhancement of the effective mass value and a non-negligible narrowing of the band-width compared to the bulk counterpart. The metallic bulk on the other hand shows unconventional superconductivity upon cooling from a Mott-insulator transition. For metallic superconductors, as iron pnictides for example, which also show a Mott-insulator transition, the ‘symptoms’ of an effective mass enhancement and band-width narrowing can be generally associated to electron-correlations, often mediating the formation of Cooper pairs and orbital mixing. Whether in our case, the origin of the detected differences might rely on the different boundary conditions imposed by a smaller doping layer, it would not be totally surprising if electron correlations would play a significant role. This, which needs further investigation, might hint at the intriguing scenario that the microscopic origin of the poorly understood superconductivity in boron-doped diamond might be strongly connected to such interactions.

If it is surprising to think that such thin systems behave as bulk, I find even more surprising that certain materials which are bulk behave as two-dimensional. This is the case of transition-metal-dichalcogenides (TMDCs). The unit cell of these materials is centrosymmetric: inversion symmetry is fully preserved. Nevertheless, the electrons wavefunctions which give rise to the electronic structure of TMDCs are so localized within each layer (and the interlayer scattering is very small), that the electronic properties of these systems are nearly-2D. This has important consequences: each layer composing the unit cell has a local breaking of the inversion symmetry which gives rise to spin-polarized bands. Given also the fact that the wavefunctions in each layer behave as 2D, these materials can exhibit a net layer- and valley-dependent spin-polarization. Spin-ARPES measurements carried

out on WSe₂ confirm this picture, showing even an experimental polarization close to 100%. TMDCs are therefore interesting systems because their huge spin-orbit coupling could be potentially tuned to allow all-electrical control of charges and spin degrees of freedom. These findings could be exploited to realize the concept of spin-based electronics (spintronics).

Recently, we carried out similar measurements in the TMDC NbSe₂ shedding new light on one of the most attractive aspects of this system: its superconductivity. NbSe₂ shows a superconducting behavior at 7.2 K upon cooling from a charge density wave transition, but in the description of this effect its electronic bands have always been treated as unpolarized, without the necessity of involving electron spins. By using spin-ARPES we demonstrated that the spin-texture of NbSe₂ shows a similar valley- and layer-dependent texture to that one of WSe₂ for the bands which have been shown to be responsible for its superconductivity. This has important implications: not only a classical BCS description breaks down since electron pairs carrying the same spin can couple, but because the origin of the coupling is a Zeeman field, applying in-plane magnetic fields even higher than the Pauli and paramagnetic limits would not break such electron pairs which instead would result protected against a magnetic perturbation. Moreover, the fashion by which the polarization manifests (valley and layer dependent) is similar to model systems for Ising superconductivity, such as gated MoS₂. An interesting future prospect would be studying and understanding the effect of magnetic impurities in this system and how/if its superconducting properties would be preserved and/or altered.

In the search for devices with low-energy consumption and low resistance, a big role is played by graphene. Indeed, the famous 2D sheet of carbon atoms hosts the giant carrier mobility of 10⁶ cm²/Vs [55] exceeding by more than two orders of magnitude that of Si [56]. Even though this a brilliant finding, my attention has anyway been attracted by a band which with transport properties is loosely connected: the σ -band (paper 8, paper 9, paper 10). Here, electron-phonon coupling (EPC) is strong and manifests with a ‘kink’ in the electronic dispersion comparable in strength to ‘kinks’ observed in high temperature superconductors. Further theoretical investigations, allowed us to understand the subtle mechanisms behind the observed EPC, which is found to be connected to the possibility of interband-transitions, breaking the accepted paradox of orthogonality between π and σ bands of graphene and at

the same time offering new ideas which might be used to turn graphene into a 70 K superconductor. That's a walkover: we only need to dope it by 3.5 eV!

Maybe, reaching the stage of superconductivity in graphene mediated by the strong EPC of its σ -band is a little bit too ambitious, thus meanwhile we can contribute to reduce the energy consumption by improving the efficiency of solar cells. Intermediate band materials are practically realizable and can constitute a real energy resource: they consist of semiconductors with a mid-gap Fermi level where due to the introduction of impurities within the bulk system a partially occupied state is formed within the bandgap. If a light source illuminates these materials, not only electron transitions from the valence to the conduction band are allowed, but also from the valence band to the intermediate state and from such an intermediate band to the conduction band. This increases the number of absorbed wavelengths resulting in an increased photo-hole current, thus a higher efficiency in a solar-cell. To test this principle we used resonant photoemission spectroscopy (RPES) on Cr-doped ZnS, accessing directly the intermediate state and going beyond this, understanding the orbital nature from which such a state originates. With this work we show the viability of RPES to study intermediate band materials, offering an approach towards engineering of high efficiency intermediate band solar cells and of other optoelectronic devices. A current activity which is going on in our group at the moment, is to extend this technique to different materials such as MoO_3 , whilst finding new routes for creating precise material patterning either by N-implantation or O-removal for tailoring and controlling material properties.

Working together with Prof. Justin Wells has certainly convinced me that in the long-term at least one technological achievement among – Si:P-base qubit, spintronics, valletronics, spin-based storage and processing technology, organic quantum-dot arrays for information storage, diamond-based electronic components robust against hostile radiation environments, high-temperature superconducting graphene, dissipationless electronics, more efficient solar-cells and optoelectronic devices – will be realized. What I was not really expecting at the beginning of my PhD is that he would have been able to convince me that in 3 years time we would have suggested a way to improve the treatment of cancer. Contrary to my expectations, we used photoemission to study the interactions between one of the most used drugs in the treatment of cancer (5-Fu) and silver, a material which often is

used as a coating for the catheters used in the delivery of such a drug. We demonstrated that the most plausible reaction product originated from the interaction between silver and 5-Fu is HF, thus constituting a serious problem for many people's lives. Furthermore, we found that graphene constitutes a good alternative to silver as coating material, and our analysis (carried out by XPS) confirmed this picture showing no sign of any reaction when 5-Fu is in contact with the 2D carbon layer (paper 12 and 17). This project, whether it was the first, it is certainly not the last one of this topic: the next step is to use graphene as an inert platform for studying the dynamics of skin-cancer formation upon UV dose and see if other molecules can actually 'cure' such a disease breaking the skin-cancer molecule into its single constituents.

Summarizing; unconventional materials such as phosphorous δ -layers, transition metal dichalcogenides (TMDs), intermediate band materials, diamond, graphene and organic semiconductors were investigated. Each of these systems hosts a unique and *sui generis* behavior.

For example, δ -doping is a way to increase abruptly the carrier mobilities in semiconductors, modifying dramatically the original properties of the host material. In addition it is particularly suitable to be patterned with atomic-scale precision. TMDs offer an excellent platform for spintronics (spin-based electronics) suggesting interesting pathways for tailoring its properties for low-dissipation devices. Intermediate band materials and graphene can be both find applications in photovoltaics, contributing to substitute part of the current market of the oil-based energy. Graphene and diamond can even be tailored such that they can show unconventional superconductivity, ideal for dissipationless electronic components. Organic semiconductors have been recently suggested for solar cells, but they can also lead to the investigation of different scientific field for different purposes, such as studying the chemistry behind a cancer treatment.

The study of materials with properties beyond the current textbook limits is important for developing new concepts and applications and the way I wanted to achieve this was through a vast array of photoemission spectroscopies, including XPS, ARPES, spin-ARPES, RPES and PEEM. Even though these works are not going to revolutionize the world, I truly believe that this study can be considered as a little brick which can contribute to develop more friendly and safe devices.

8.1 Summary of the main results

In order to advance the existing state of the art in technology and lead to new real improvements in our standard of life, research has to contribute with new ideas, new concepts and new methodologies for studying existing problems and finding possible solutions. My PhD research has been driven by this idea: if there is an interesting scientific problem to which we can contribute with photoemission and if we are truly driven by the science behind such a problem, then we can attempt to study it and suggest possible scientific solutions. This is the reason for which this Thesis contains a wide spectrum of materials with distinct properties.

In particular, we can summarize the scientific findings of my work as it follows:

1. *Studying, tuning and ultimately controlling the electronic properties of quantum materials for quantum device applications.* In particular, we demonstrated how controlling the shape of doping potentials in 2DEGs buried in semiconductors is a viable approach to modify and get control over the lifetimes of carriers. We demonstrated how such lifetimes can be affected by many-body effects, thus a systematic understanding of these interactions is of fundamental interest for devices, whilst it offers a deep insight into the microscopic origin of the physics which dominates these systems.

We found that the spin of the electrons in a solid plays an important role in shaping the properties of the solid itself, in particular for materials which exhibit a strong spin-orbit coupling. Thus, understanding the spin-texture of systems is important not only from a fundamental physics perspective but also because it is the first, necessary step towards engineering spin-textures for electronics: if the spins of the electrons could be controlled, this would allow the development of novel spin-based devices, which, as mentioned, would also fall into the framework of dissipationless electronics. Specifically, we demonstrated that fully spin-polarized bands are possible even in centrosymmetric systems, thus we do not necessarily need a breaking of the global inversion symmetry in order to create spin-polarization.

2. *Expanding the fundamental knowledge.* An important aspect which has been covered by my PhD Thesis is that one of expanding the existing

textbook knowledge in solid state physics, whilst offering new concepts which might lead to new technological advances. Specifically, we demonstrated, using graphene as a test material, that electron-phonon coupling can manifest far away from the Fermi level. This observation constitutes a breakdown of what has been thought so far, i.e. that collective excitations cannot manifest so far from E_F . Furthermore, this observation leads to the conceptual idea of how even low energy bands in materials could be potentially tailored such that the material studied could be turned into a superconductor.

3. *Contributing to medical applications and other fields of research.* Another important thing I learned during my PhD is that keeping all disciplines connected together is probably the most efficient way of advancing the existing technologies. In particular, we demonstrated, by using photoemission, that organic compounds such as drugs used in the treatment of cancer can be successfully studied and understood. We showed that it is possible to monitor the reaction between drugs and other materials; in particular, we tested the reaction between 5-Fu and silver, demonstrating that HF is released. Whilst, the complications of releasing HF into the body of a patient are clear, we also studied a possible solution to this problem which involves graphene. Graphene is inert and does not react with the chemotherapy drugs, thus it will be interesting in the future, to figure out a possible route for integrating graphene in medical technologies.

4. *Expanding the photoemission toolbox to study materials with unconventional properties.* For all the works presented in this Thesis, I made a non-standard use of photoemission to study materials with unconventional properties. For example, 2DEGs are buried a few nanometers beneath the surface of a semiconductor, thus ARPES, which is a very surface sensitive technique, would not be able to detect useful information from these systems if used in a ‘traditional way’. However, by an appropriate choice of the photon energy, we can probe even sub-surface features, thus the electronic structure of the buried 2DEGs can be revealed. We used Spin-ARPES, which allows to resolve the spin texture of systems. We studied the orbital contributions to a certain electronic state in intermediate band materials by using RPES. In general, we use photoemission spectroscopies to study materials whose properties could not have been otherwise studied with standard techniques, demonstrating how powerful the combination material-instrument is in uncovering the properties of solid state physics systems.

8.2 Final considerations

In my life, I have been always deeply attracted by physics phenomena which form the world as we see it and as we know it today. I have been even more attracted by physics when I had to face a new problem for which an evident solution did not exist. I see my PhD study as an important forming experience which gave me powerful tools and critical thinking skills to contribute to broaden the existing understanding of physics. Working with people much more experienced than me has been essential in order to expand my knowledge and acquire important skills.

Bibliography

- [1] A. Einstein *Annus Mirabilis Papers*, Annalen der Physik, 1905
- [2] K. Novoselov, Z. Jiang, Y. Zhang, S. V. Morozov, H. L. Stormer, U. Zeitler, J. C. Maan, G. S. Boebinger, P. Kim, A. K. Geim *Science*, *315*, 1379, 2007
- [3] D. C. Elias, R. V. Gorbachev, A. S. Mayorov, S. V. Morozov, A. A. Zhukov, P. Blake, L. A. Ponomarenko, I. V. Grigorieva, K. S. Novoselov, F. Guinea and A. K. Geim *Nature Physics*, *7*, 701, 2011
- [4] A. K. Geim and K. S. Novoselov *Nature Materials* *6*, 183 - 191 (2007)
- [5] A. Lanzara, P. V. Bogdanov, X. J. Zhou, S. A. Kellar, D. L. Feng, E. D. Lu, T. Yoshida, H. Eisaki, A. Fujimori, K. Kishio, J. I. Shimoyama, T. Noda, S. Uchida, Z. Hussain and Z.-X. Shen *Nature* *412*, 510-514, 2001
- [6] E. F. Schubert *Delta-doping of Semiconductors*, 1996
- [7] J. J. Harris *Journal of Materials Science: Materials in Electronics* *4*, 93 1993
- [8] J. M. Riley, F. Mazzola, M. Dendzik, M. Michiardi, T. Takayama, L. Bawden, C. Granerød, M. Leandersson, T. Balasubramanian, M. Hoesch, T. K. Kim, H. Takagi, W. Meevasana, Ph. Hofmann, M. S. Bahramy, J. W. Wells and P. D. C. King *Nature Physics* *10*, 835–839 2014
- [9] Pfeiffer rotary pumps manual. *electronic link: <https://www.pfeiffer-vacuum.com>*
- [10] Kramer C., Mühlbauer A. *DIN 28400-1990, Part 1, Vacuum technology (2002)*

- [11] M. Bianchi, R. C. Hatch, J. Mi, B. B. Iversen and P. Hofmann *Phys. Rev. Lett.* **107**, 086802, (2011)
- [12] H.E. Farnsworth, R.E. Schlier, T.H. George and R.M. Burger *J. Appl. Phys.*, **26**, 252 (1955)
- [13] H.E. Farnsworth *J. Vac. Sci. Technol.* **20**, 271 (1982)
- [14] O.C. Yonts and D.E. Harrison *J. Appl. Phys.* **31**, 1583 (1960)
- [15] G.K. Wehner and D.J. Hajicek *J. Appl. Phys.* **42**, 1145 (1971)
- [16] King-Ning Tu, James W. Mayer, and Leonard C. Feldman *Electronic Thin Film Science for Electrical Engineers and Materials Scientists*, Macmillan, New York, 1992, pp. 101–102.
- [17] Rosanna Larciprete, Søren Ulstrup, Paolo Lacovig, Matteo Dalmiglio, Marco Bianchi, Federico Mazzola, Liv Hornekær, Fabrizio Orlando, Alessandro Baraldi, Philip Hofmann, and Silvano Lizzit *ACS Nano*, **2012**, *6* (11), pp 9551–9558
- [18] B. Bransden and C. Joachain *Physics of atoms and molecules*, Pearson Education (Longman, 1983), ISBN 9780582444010
- [19] C. Kittel *Solid state physics* (Wiley, 1995)
- [20] N. E. Ashcroft and N. D. Mermin *Solid state physics* (Saunders College, Philadelphia, 1976), International Ed.
- [21] Slater, J. C. *Physical Review* **51** (10): 846–851, (1937)
- [22] Van Vleck, J. *Physical Review* **41**: 208 (1932)
- [23] Schrödinger, E. *Physical Review* **28** (6): 1049–1070 (1926)
- [24] F. Bloch *Z. Physik* **52**: 555–600 (1928)
- [25] Gurevich V. L., Thellung A. *Physical Review B* **42** (12): 7345–7349 (1990)
- [26] Fermi, Enrico *Sulla quantizzazione del gas perfetto monoatomico. Rendiconti Lincei*, 1926

- [27] Dirac, Paul A. M. *Proceedings of the Royal Society, Series A* 112 (762): 661–77 (1926)
- [28] Damascelli, A. *Physica Scripta. Vol. T109*, 61–74, 2004
- [29] Dirac, P. A. M. *Proceedings of the Royal Society A* 114 (767): 243–265 (1927)
- [30] Alan Hastings *The Art of Analog Layout*, 2nd ed (2005)
- [31] Goldstein, H., Poole, C. P., Jr., Safko, J. L. *Classical Mechanics* (3rd ed.) (2002)
- [32] Mattuck Richard D. *A Guide to Feynman Diagrams in the Many-Body Problem* (1992)
- [33] Negele, J. W. and Orland, H. *Quantum Many-Particle Systems* (1988)
- [34] J. Bardeen and D. Pines *Phys. Rev.* 99, 1140 (1955)
- [35] F. Mazzola, J. W. Wells, R. Yakimova, S. Ulstrup, J. A. Miwa, R. Balog, M. Bianchi, M. Leandersson, J. Adell, P. Hofmann, and T. Balasubramanian *Phys. Rev. Lett.* 111, 216806 (2013)
- [36] F. Mazzola, C. M. Polley, J. A. Miwa, M. Y. Simmons and J. W. Wells *Appl. Phys. Lett.* 104, 173108 (2014)
- [37] J. M. Ziman *Principles of the Theory of Solids, Second Edition*, Cambridge University Press (1972)
- [38] Hüfner , S. *Very High Resolution Photoelectron Spectroscopy* (2007), Springer
- [39] I. Fischer *Int. J. Mass. Spec.* 216, 131–153 (2002)
- [40] J. M. Luttinger and J. C. Ward *Phys. Rev.* 118(5), 1417–1427 (1960)
- [41] D. Pines and P. Nozieres *The Theory of Quantum Liquids – Normal Fermi Liquids, volume 1*. Addison-Weseley, New York Amsterdam–Tokyo (1966)
- [42] W. L. McMillan and J. M. Rowell *Phys. Rev. Lett.* 14(4), 108–112 (1965)

- [43] J. Bardeen *Science*, Vol. 181 no. 4106 pp. 1209-1214 (1973)
- [44] H. Jahn and E. Teller *Proceedings of the Royal Society of London. Series A, Mathematical and Physical Sciences (1934-1990)* 161 (905): 220-235 (1937)
- [45] Wolf S. A., Chtchelkanova A. Y., Treger D. M. *Spintronics—A retrospective and perspective. IBM Journal of Research and Development* 50: 101 (2006)
- [46] Johnson M. Silsbee R. H. *Physical Review Letters* 55 (17): 1790–1793 (1985)
- [47] M. H. Berntsen, P. Palmgren, M. Leandersson, A. Hahlin, J. Åhlund, B. Wannberg, M. Månsson, and O. Tjernberg *Review of Scientific Instruments* 81, 035104 (2010)
- [48] N. F. Mott and H. S. W. Massey *The Theory of Atomic Collisions, Third Edition (Oxford: Oxford University Press) (1965)*
- [49] Bransden B.H. Joachain C.J. *Physics of Atoms and Molecules, Longman Scientific and Technical, Wiley (1990)*
- [50] F. Mazzola, T. Trinh, S. Cooil, E Ramleth Østli, K. Høydalvik, E. Torbjørn Bakken Skjønfsjell, S. Kjelstrup, A. Preobrajenski, A. A Cafolla, D. A. Evans, D. W. Breiby and J. W. Wells *2D Materials, Volume 2, Number 2 (2015)*
- [51] F. Mazzola, M. Nematollahi, Z. S. Li, S. Cooil, X. Yang, T. W. Reenaas and J. W. Wells *Appl. Phys. Lett.* 107, 192104 (2015)
- [52] F. Mazzola, M. T. Edmonds, K. Høydalvik, D. J. Carter, N. A. Marks, B. C. C. Cowie, L. Thomsen, J. Miwa, M. Y. Simmons, and J. W. Wells *ACS Nano*, 2014, 8 (10), pp 10223–10228
- [53] Geim A. K., Novoselov K. S. *Nature Materials* 6 (3): 183–91 (2007)
- [54] K. S. Novoselov, Z. Jiang, Y. Zhang, S. V. Morozov, H. L. Stormer, U. Zeitler, J. C. Maan, G. S. Boebinger, P. Kim2, A. K. Geim *Science*, 315, 1379, (2007)

- [55] D. C. Elias, R. V. Gorbachev, A. S. Mayorov, S. V. Morozov, A. A. Zhukov, P. Blake, L. A. Ponomarenko, I. V. Grigorieva, K. S. Novoselov, F. Guinea and A. K. Geim *Nature Physics*, **7**, 701, (2011)
- [56] K. S. Novoselov, V. I. Falko, L. Colombo, P. R. Gellert, M. G. Schwab and K. Kim *Nature* **490**, 192–200 (2012)
- [57] F. Mazzola, A. Pakpour Tabrizi, J. A. Miwa, R. Jackman and J. W. Wells *In preparation*
- [58] M. M. Ugeda, A. J. Bradley, Y. Zhang, S. Onishi, Y. Chen, W. Ruan, C. Ojeda-Aristizabal, H. Ryu, M. T. Edmonds, H. Tsai, A. Riss, S. K. Mo, D. Lee, A. Zettl, Z. Hussain, Z. X. Shen and M. F. Crommie *Nature Physics* (2015) doi:10.1038/nphys3527
- [59] W. L. McMillan *Phys. Rev. B* **12**, 1187
- [60] L. Bawden, S. Cooil, F. Mazzola, J. M. Riley, L. Collins-McIntyre, V. Sunko, M. Leandersson, C. Polley, T. Balasubramanian, T. K. Kim, M. Hoesch, J. W. Wells, G. Balakrishnan, M. S. Bahramy and P. D. C. King *Spin-valley locking in the normal state of a transition-metal dichalcogenide superconductor, in progress*
- [61] M. Nematollahi, X. Yang, L. M. S. Ass, Z. Ghadyani, M. Kildemo, U. Gibson, and T. W. Reenaas *Sol. Energy Mater. Sol. Cells* **141**, 322–330 (2015)
- [62] K. M. Kadish *The Porphyrin Handbook. Elsevier* (1999)
- [63] S. Nowakowska, F. Mazzola, M. Almperti, F. Song, T. Voigt, J. Nowakowski, A. Wäckerlin, C. Wäckerlin⁵, J. Wiss, C. Polley, M. Leandersson, S. Fatayer, T. Ivas, S. F. Mousavi, A. Ahsan, T. Nijs, O. Popova, J. Zhang, M. Muntwiler, C. Thilgen, M. Stöhr, F. Diederich, J. Wells, T. Jung *Adsorbate induced modification of the confining barriers in a quantum box array*
- [64] J. W. Wells, J. H. Dil, F. Meier, J. Lobo-Checa, V. N. Petrov, J. Osterwalder, M. M. Ugeda, I. Fernandez-Torrente, J. I. Pascual, E. D. L. Rienks, M. F. Jensen, and Ph. Hofmann *Phys. Rev. Lett.* **102**, 096802 (2009)

- [65] J. Lobo-Checa, F. Mazzola, L. Barreto, F. M. Schiller, J. W. Wells, M. Corso, L. A. Miccio, I. Piquero-Zulaica, N. C. Plumb, P. Hofmann and J. E. Ortega *Surface Dimensionality Transition on a Curved Bi(111) Sample: Surface States Evolution from topologically Trivial to Topologically protected*
- [66] J. Vegh *Journal of Electron Spectroscopy and Related Phenomena* 151,3, 159–164 (2006)
- [67] Behnaz Gharekhanlou and Sina Khorasani *An overview of tight-binding method for two-dimensional C-structures, Graphene: Properties, Synthesis and Applications*, (2011)
- [68] T. F. Watson, B. Weber, J. A. Miwa, S. Mahapatra, R. M. P. Heijnen, and M. Y. Simmons *Nano Letters* 14, 1830 (2014)
- [69] B. Weber, S. Mahapatra, T. F. Watson, and M. Y. Simmons *Nano Letters* 12, 4001 (2012)